

© 2015

RAJESH KAPPERA

ALL RIGHTS RESERVED

**ELECTRONIC PROPERTIES AND PHASE ENGINEERING OF  
TWO-DIMENSIONAL MoS<sub>2</sub>**

by

**RAJESH KAPPERA**

**A Dissertation submitted to the  
Graduate School-New Brunswick  
Rutgers, The State University of New Jersey**

**in partial fulfillment of the requirements**

**for the degree of**

**Doctor of Philosophy**

**Graduate Program in Electrical and Computer Engineering**

**written under the direction of**

**Professor Manish Chhowalla**

**and approved by**

---

---

---

---

---

**New Brunswick, New Jersey**

**January, 2015**

**ABSTRACT OF THE DISSERTATION**  
**ELECTRONIC PROPERTIES AND PHASE ENGINEERING OF**  
**TWO DIMENSIONAL MoS<sub>2</sub>**

**By Rajesh Kappera**

Dissertation Director: **Prof. Manish Chhowalla**

There has been an increased interest in the research of 2D layered materials since the past few years especially after the discovery and physics related study of Graphene, a monolayer of graphite. Layered materials beyond graphene are the family of transition metal dichalcogenides (TMDs) which consist of over 40 members ranging from semiconductors to insulators to metals. All these materials are shown to be easily exfoliated to form monolayers which exhibit a new set of properties owing to the quantum confinement effects that occur during their exfoliation. The intrinsic thickness of less than 1nm per layer, lack of dangling bonds, controllable bandgap and precise control of thickness has aroused the interest of electrical engineers all over the world to use these materials for future electronics and make the dream of all 2D electronics to become true.

Field effect transistors made from TMD semiconductors (MoS<sub>2</sub>, WS<sub>2</sub>, MoSe<sub>2</sub>, WSe<sub>2</sub> etc.) are exhibiting excellent characteristics namely ON/OFF ratios in the range of 10<sup>8</sup>, saturation currents exceeding 200 μA/μm, mobilities exceeding 100 cm<sup>2</sup>/Vs and subthreshold swings almost approaching the theoretical limit of 60 mV/dec. Though these values are impressive, they are far below their theoretical expectations, mainly due to the high contact resistance between the metal and semiconductor because of which their excellent intrinsic characteristics are not practically realized. There have been many efforts

in mitigating this high contact resistance such as use of different contact metals, chemical doping of contact regions and long thermal annealing of devices which resulted in partial success. The aim of this work would be in establishing a universal strategy in reducing this high contact resistance to provide an ohmic-like contact between the metal and the TMD semiconductor by employing their phase-engineered metallic counterparts as the contacts. By fabricating transistors in which the electrode material and the channel similar is of the same material composition, many factors, which are detrimental to the operation of high performance transistors, can be eliminated. We have gained expertise in phase transformation of these transition metal dichalcogenides and successful utilized them as the contacts by locally patterning different phases on a single monolayer flake. We obtained record saturation currents, transconductances, mobilities and sub-threshold slopes for our novel transistors. This thesis will include details of synthesis of these TMD semiconductors, phase transformation and fabrication of transistors with lowered contact resistance with main emphasis on Molybdenum disulfide ( $\text{MoS}_2$ ).

## DEDICATION

*Dedicated with great affection and gratitude to*

***My family*** – for their love

***My friends*** – for their support

*and*

***My mentors*** – for continued guidance

## ACKNOWLEDGEMENTS

There are a very few people who continuously hold importance and reverence at every stage in one's life. One such person for me is my advisor, Prof. Manish Chhowalla. At a stage in my Ph.D. where I appeared to be lost, he took me into his group, motivated and encouraged me to be a good scientist as what I am today. Of equal importance has been the guidance provided by the post-doc in our group, Dr. Damien Voiry. His intellectual inputs helped me figure out intricate details of certain vital aspects in this Ph.D. work.

I would like to thank the rest of my committee members, Prof. Yicheng Lu, Prof. Wei Jiang, Prof. Michael Caggiano and Dr. Aditya Mohite for providing me valuable inputs and guidance on research and future career plans. I am grateful to the useful discussions and funding support provided by Prof. Eric Garfunkel, Prof. Leonard Feldman and Prof. Athina Petropulu. I also appreciate the encouragement provided by my former advisors, Prof. Moncef Tayahi and Prof. Alan Delahoy, who explained the importance of a successful Ph.D. for future career.

Special thanks goes to my fellow group-mates, Mr. Ibrahim Bozkurt, Mr. Muharrem Acerce, Mr. Sol Torrel, Mr. Raymond Fullon, Mrs. Maryam Salehi, Mr. Diego Alves, Mrs. Rut Rivera, Mr. Piljae Joo and my friends in Electrical engineering department, Dr. Pavel Ivanoff Reyes, Dr. Yang Zhang, Mr. Li Rui and Mr. Wayne Warrick. An important person who has provided continuous help is my undergrad, Mr. Wesley Jen. His support in the lab at Rutgers as well as Los Alamos saved a good amount of time and effort for me.

All the device work in this thesis has been done at Los Alamos National laboratory. I would be indebted to Dr. Aditya Mohite, Dr. Gautam Gupta, Dr. Andrew Dattelbaum and the

entire Light to energy team for making it possible. I am grateful to the unperturbed access given to me to most of the research facilities and equipment in the Center for Integrated Nanotechnologies (CINT) and Material Physics and Applications, MPA-11. A few people I'd like to mention are Dr. Brain Crone, Dr. Eric Brosha, Mr. Jon Kevin Baldwin, Mr. Chris Sheehan and the post-docs, Dr. Akhilesh Singh, Dr. Sibel Ebru Yalcin, Dr. Hisato Yamaguchi, Dr. Wanyi Nie, Dr. Rajib Pramanik and Dr. Aruntej Mallajosyula. Life would have been boring at Los Alamos without the fun times I had with my friends, Mr. Sidong Lei, Mr. Dustin Cummins, Dr. Brittany Branch, Dr. Charudatta Galande, Ms. Asli Unal and Mr. Ismail Bilgin. The visiting scientists, Prof. Swastik Kar, Prof. Bruce Alphenaar and Mr. Deep Jariwala provided some advice which proved critical to my work.

I would like to thank my entire family, most importantly, Prof. Kappera Nageswar Rao, Mrs. Kappera Uma, Mr. Kanhailal Bhambhani, Mrs. Rashmi Bhambhani, Mrs. Varsha Kappera, Mr. Ram Naresh Kappera, Mrs. Lakshmi Kappera, Dr. Akhilesh Bhambhani, Mrs. Harshita Bhambhani, Mr. Kamal Bhambhani and Mrs. Riya Bhambhani for their unending love, support and the patience they exhibited during my Ph.D. Special thanks goes out to my dear aunt and uncle, Dr. Bal Reddy Kedika and Mrs. Rani Kedika and my brothers, Ramu and Satish Kedika, for their help and support in various stages of my Ph.D. Without the constant encouragement of all these family members, this work would have not achieved its completion.

Lastly, I would like to thank the Electrical Engineering department and Materials Science Engineering department of Rutgers University for providing me the opportunity to take up Ph.D. and for the funding support in terms of teaching and research assistantship.

## TABLE OF CONTENTS

<b>Abstract</b>	ii
<b>Dedication</b>	iv
<b>Acknowledgements</b>	v
<b>Table of Contents</b>	vii
<b>List of Illustrations</b>	x
<b>List of Tables</b>	xiv
<b>Chapter 1. Introduction</b>	<b>1</b>
1.1 Motivation	1
1.2 Objectives and Scope of Work	2
1.3 Organization of the thesis	3
<b>Chapter 2. Layered Materials</b>	<b>4</b>
2.1 Layered Materials	4
2.2 Graphene	5
2.3 Layered Transition Metal Dichalcogenides	6
2.4 Chapter summary	9
<b>Chapter 3. Molybdenum disulfide</b>	<b>10</b>
3.1 Molybdenum disulfide (MoS <sub>2</sub> )	10
3.2 Structure of MoS <sub>2</sub>	11
3.3 Synthesis methods	12
3.3.1 Top-down approach	12
3.3.2 Bottom-up approach	16
3.4 Optical Spectroscopy on MoS <sub>2</sub>	19

3.4.1 Raman Spectroscopy	19
3.4.2 Photoluminescence	21
3.5 Electrical Characterization	23
3.6 Chapter summary	26
<b>Problem Statement and Solution Strategy</b>	<b>27</b>
<b>Chapter 4. Phase Engineering in MoS<sub>2</sub></b>	<b>28</b>
4.1 Phase Engineering in MoS <sub>2</sub>	28
4.2. Characterizing 1T and 2H MoS <sub>2</sub>	29
4.2.1 Raman Spectroscopy	29
4.2.2 X-Ray Photoelectron Spectroscopy	30
4.2.3 Fluorescence Imaging	32
4.2.4 Scanning Electron Microscopy	33
4.2.5 Transmission Electron Microscopy	34
4.3. Chapter summary	35
<b>Chapter 5. Devices on Mechanically Exfoliated MoS<sub>2</sub></b>	<b>36</b>
5.1 Device Fabrication	36
5.2 Electrical Measurements	39
5.3 Chapter summary	43
<b>Chapter 6. Devices with 1T Phase MoS<sub>2</sub></b>	<b>44</b>
6.1 1T Phase conversion	44
6.2 1T MoS <sub>2</sub> device results	46
6.3 Phase engineered contacts for MoS <sub>2</sub> devices	49
6.4 Chapter summary	58

<b>Chapter 7. Evaluation of Contact resistance and Schottky barrier height and fabrication of top-gated devices</b>	<b>59</b>
7.1 Transmission line measurement (TLM)	59
7.2 Low temperature measurements – Schottky barrier height	65
7.3 Top gate devices	69
7.3.1 Devices with HfO <sub>2</sub> dielectric	72
7.3.2 Devices with SiO <sub>2</sub> dielectric	73
7.3.3 Devices with Si <sub>3</sub> N <sub>4</sub> dielectric	74
7.4 Comparison of top gated devices	75
7.5 Chapter summary	78
<b>Chapter 8. CVD MoS<sub>2</sub> and Other TMDs</b>	<b>79</b>
8.1 Chemical vapor deposition of MoS <sub>2</sub>	79
8.2 Devices with other Transition metal dichalcogenides	84
8.2.1 Tungsten disulfide (WS <sub>2</sub> )	84
8.2.2 Molybdenum diselenide (MoSe <sub>2</sub> )	88
8.2.3 Tungsten diselenide (WSe <sub>2</sub> )	92
8.3 Photocurrent measurement on monolayer CVD MoS <sub>2</sub>	95
8.4 Chapter summary	98
<b>Chapter 9. Future work and Conclusions</b>	<b>99</b>
9.1 Future work	99
9.2 Conclusions	102
<b>References</b>	<b>104</b>

## LIST OF ILLUSTRATIONS

<b>2.1.</b>	Graphene crystal, structure and E-k diagram	6
<b>2.2.</b>	Graphene electrical and nanoribbon properties	6
<b>2.3.</b>	Different properties of TMD family members	8
<b>2.4.</b>	Band alignment of WSe <sub>2</sub> , MoSe <sub>2</sub> , WS <sub>2</sub> and MoS <sub>2</sub>	9
<b>3.1.</b>	Single layer MoS <sub>2</sub> atomic structure	10
<b>3.2.</b>	Structure of 2H MoS <sub>2</sub>	11
<b>3.3.</b>	Structure of 1T MoS <sub>2</sub>	12
<b>3.4.</b>	Mechanical exfoliation of MoS <sub>2</sub>	13
<b>3.5.</b>	TMD Solutions prepared by ultra-sonication	14
<b>3.6.</b>	TMD Solutions prepared by lithium intercalation	15
<b>3.7.</b>	Properties of MoS <sub>2</sub> films prepared by lithium intercalation based exfoliation	16
<b>3.8.</b>	CVD MoS <sub>2</sub> growth processes	18
<b>3.9.</b>	Variation in MoS <sub>2</sub> Raman spectra with flake thickness	20
<b>3.10.</b>	Variation in MoS <sub>2</sub> Raman spectra with phase change	21
<b>3.11.</b>	Variation in MoS <sub>2</sub> Photoluminescence with flake thickness	22
<b>3.12.</b>	MoS <sub>2</sub> device and electrical characterization	24
<b>3.13.</b>	MoS <sub>2</sub> device and electrical characterization with K doping	25
<b>3.14.</b>	MoS <sub>2</sub> multilayer device and electrical characterization	26
<b>4.1.</b>	Mechanical exfoliation of MoS <sub>2</sub> and characterization	28
<b>4.2.</b>	Images of MoS <sub>2</sub> flake before and after phase transformation	29
<b>4.3.</b>	Variation in MoS <sub>2</sub> Raman spectra with gradual change in phase	30

<b>4.4.</b>	Variation in MoS <sub>2</sub> XPS spectra with gradual change in phase	31
<b>4.5.</b>	Fluorescence images of patterned MoS <sub>2</sub> flakes	33
<b>4.6.</b>	SEM images of patterned MoS <sub>2</sub> flakes	34
<b>4.7.</b>	TEM image of atomic boundary of 1T-2H MoS <sub>2</sub>	34
<b>5.1.</b>	Images of mechanically exfoliated MoS <sub>2</sub> flakes	37
<b>5.2.</b>	Images of devices made of MoS <sub>2</sub> flakes	38
<b>5.3.</b>	FET characterization of MoS <sub>2</sub> devices with Au-Ti contacts	39
<b>5.4.</b>	Fabrication steps of Au contacted MoS <sub>2</sub> devices	41
<b>5.5.</b>	FET characterization of MoS <sub>2</sub> devices with Au contacts	42
<b>6.1.</b>	EELS spectrum of 1T MoS <sub>2</sub>	45
<b>6.2.</b>	NRA of 1T MoS <sub>2</sub>	46
<b>6.3.</b>	FET characterization of 1T MoS <sub>2</sub> devices	47
<b>6.4.</b>	Four probe measurement of 1T MoS <sub>2</sub> device	48
<b>6.5.</b>	Devices on a patterned MoS <sub>2</sub> flake	49
<b>6.6.</b>	Devices with contaminated MoS <sub>2</sub> channel	50
<b>6.7.</b>	FET characterization of MoS <sub>2</sub> devices with Au-1T contacts	51
<b>6.8.</b>	Transfer characteristics of Au-2H and Au-1T contacted devices	53
<b>6.9.</b>	Saturated output characteristics of Au-2H and Au-1T contacted MoS <sub>2</sub> devices	54
<b>6.10.</b>	MoS <sub>2</sub> devices with Palladium contacts	56
<b>6.11.</b>	MoS <sub>2</sub> devices with Calcium contacts	57
<b>7.1.</b>	TLM analysis of Au-2H contacted devices	60
<b>7.2.</b>	TLM analysis of Au-1T contacted devices	61

<b>7.3.</b>	Gate dependence of contact resistance	62
<b>7.4.</b>	Current versus 1T MoS <sub>2</sub> flake thickness	63
<b>7.5.</b>	TLM analysis of multi-layered MoS <sub>2</sub> devices	64
<b>7.6.</b>	Charge conduction states at metal-semiconductor interface	65
<b>7.7.</b>	Low temperature transport measurements on Au-2H contacted MoS <sub>2</sub> devices and Schottky barrier height extraction	66
<b>7.8.</b>	Low temperature transport measurements on Au-1T contacted MoS <sub>2</sub> devices and Schottky barrier height extraction	69
<b>7.9.</b>	Characterization of top-gated MoS <sub>2</sub> devices with HfO <sub>2</sub> dielectric	73
<b>7.10.</b>	Characterization of top-gated MoS <sub>2</sub> devices with SiO <sub>2</sub> dielectric	74
<b>7.11.</b>	Characterization of top-gated MoS <sub>2</sub> devices with Si <sub>3</sub> N <sub>4</sub> dielectric	75
<b>7.12.</b>	Comparison of top-gated devices with and without 1T contacts	76
<b>7.13.</b>	Schematics of intended and actual 1T contacted MoS <sub>2</sub> devices	77
<b>8.1.</b>	CVD furnace for growth of TMDs	79
<b>8.2.</b>	Optical characterization of monolayer CVD MoS <sub>2</sub>	80
<b>8.3.</b>	FET characterization of generic monolayer CVD MoS <sub>2</sub>	81
<b>8.4.</b>	Optical characterization of phase transformed CVD MoS <sub>2</sub>	82
<b>8.5.</b>	FET characterization of 1T contacted monolayer CVD MoS <sub>2</sub>	83
<b>8.6.</b>	Optical images of mechanically exfoliated WS <sub>2</sub> flakes	85
<b>8.7.</b>	Raman and Photoluminescence spectra of 2H and 1T WS <sub>2</sub> flakes	85
<b>8.8.</b>	FET characterization of Au-2H and Au-1T contacted WS <sub>2</sub> devices	87
<b>8.9.</b>	Optical images of mechanically exfoliated MoSe <sub>2</sub> flakes	88
<b>8.10.</b>	Raman and Photoluminescence spectra of 2H and 1T MoSe <sub>2</sub> flakes	89

<b>8.11.</b>	FET characterization of Au-2H and Au-1T contacted MoSe <sub>2</sub> devices	91
<b>8.12.</b>	Optical images of mechanically exfoliated WSe <sub>2</sub> flakes	92
<b>8.13.</b>	Raman and Photoluminescence spectra of 2H and 1T WSe <sub>2</sub> flakes	92
<b>8.14.</b>	FET characterization of Au-2H and Au-1T contacted WSe <sub>2</sub> devices	94
<b>8.15.</b>	Opto-electrical characterization of Au-2H and Au-1T contacted CVD monolayer MoS <sub>2</sub> photodetectors	97
<b>9.1.</b>	Mono-bilayer and Mono-multilayer interfaces of mechanically exfoliated and CVD MoS <sub>2</sub> flakes	100
<b>9.2.</b>	All 2D Heterojunction solar cells with TMD semiconductors	101

## LIST OF TABLES

<b>2.1.</b>	Band gaps of bulk and monolayer TMDs	8
<b>5.1.</b>	Device properties of MoS <sub>2</sub> FETs with Au-Ti contacts	40
<b>5.2.</b>	Device properties of MoS <sub>2</sub> FETs with Au contacts	42
<b>6.1.</b>	Device properties of MoS <sub>2</sub> FETs with Au-1T contacts	52
<b>6.2.</b>	Comparison of bottom-gated Au-2H and Au-1T contacted devices	53
<b>6.3.</b>	Comparison of Pd contacted devices with and without 1T contacts	56
<b>6.4.</b>	Comparison of Ca contacted devices with and without 1T contacts	57
<b>7.1.</b>	Comparison of top-gated Au-2H and Au-1T contacted devices	76
<b>8.1.</b>	Comparison of Au-2H and Au-1T contacted CVD MoS <sub>2</sub> devices	84
<b>8.2.</b>	Comparison of Au-2H and Au-1T contacted devices for all TMDs	95

## **Chapter 1**

### **Introduction**

#### **1.1 Motivation**

Present day electronics rely on bulk semiconductors which include silicon and other III-V semiconductors such as GaAs and GaN. These electronics have been undergoing miniaturization since the past five decades following Moore's law which predicted in year 1965 that the transistor density in a chip doubles every two years<sup>1-4</sup>. The law has proven to be very accurate and has been used in the semiconductor industry for setting up long term planning and research goals. The advantages of device miniaturization have been many but in particular is the increased functionality per unit area and the improved performance of each transistor with scaling. However as the channel length of the transistors have gone down and have now reached the nanometer scale, these bulk semiconductor based transistors have begun to experience short channel effects which lead to high off currents and hence heat problems in present day electronics. This is where Moore's law has begun to break down and the ITRS (International technology roadmap for semiconductors) now predicts that the transistor densities will not increase every two years but three years<sup>5</sup>. The presence of a leakage current or off current causes the problem of power dissipation where a static power (a function of the drive voltage and the leakage current) needs to be completely dissipated. As the device dimensions have gone down, the static power increased and thus future scaling has been limited to the rate at which the heat caused by this static power can be dissipated.

To overcome these challenges, efforts have begun in studying novel device structures which solve the problems at short channel lengths, some examples of which are the multiple gate transistors or the FinFETs<sup>6</sup> or planar ultrathin body (UTB) transistors<sup>7</sup>. For

the UTB technology, new materials such as the layered materials are constantly been explored. Though the research of these two dimensional layered materials has been started by Graphene, lack of a finite bandgap has stalled the growth of graphene electronics. A new family of 2D materials called the transition metal dichalcogenides (TMDs) have thus been introduced and molybdenum disulfide, MoS<sub>2</sub>, has emerged as a strong competitor to silicon with its direct bandgap of 1.9 eV and good electrical properties

## **1.2 Objectives of Work**

A major problem in MoS<sub>2</sub> based transistors is in making efficient contacts with the electrode metal. The high schottky barrier that exists between the metal and MoS<sub>2</sub> often results in high contact resistances which results in low drive currents and mobilities than what has been predicted in theory. The primary objective of this thesis is in solving the contact resistance issue in MoS<sub>2</sub> transistors.

We are proposing phase engineered electrodes as efficient contacts to MoS<sub>2</sub> transistors. MoS<sub>2</sub> has a metastable 1T polymorph which is metallic in nature. It has been observed from current state of the art electronics that better devices can be obtained if the electrode material and channel material are same since there are no structural and interfacial defects. In this work, phase engineering in MoS<sub>2</sub> will be extensively explored and characterization will be performed with Raman, XPS and HRTEM spectroscopies. Electrical properties of 1T MoS<sub>2</sub> will be studied with an objective to understand the metallic nature and to estimate the carrier concentration thereby. Devices made with 1T phase contacts will be fabricated, measured and their performance will be compared to the generic MoS<sub>2</sub> field effect transistors. An attempt will also be made to fabricate top gated transistors which would require the deposition of dielectric onto MoS<sub>2</sub> channel. Reduction in contact resistance would be studied through intense TLM based devices and a comparison would be made of

1T and non-1T based contacts. Schottky barrier height of both the types of devices would also be measured so as to compare the amount of reduction in the barrier height. An attempt would also be made to prove the eligibility of this method by using TMD materials other than MoS<sub>2</sub>.

### **1.3 Organization of the thesis**

Chapter 1 of the thesis establishes the motivation and specific goals of the project. Chapter 2 and 3 give literature review which provide some details to establish the work done in this thesis. Chapter 2 is on the basic understanding of the properties of layered materials such as graphene and provides an introduction to the family of transition metal dichalcogenides. Chapter 3 gives a literature review of MoS<sub>2</sub> where its layer dependent properties, properties of its different phases and electrical properties are discussed. Chapter 4 to 8 discuss the experimental work, measurements, results, and analysis of the results. Chapter 4 covers the phase engineering process to obtain 1T phase MoS<sub>2</sub> and its characterization results. Chapter 5 is about optimizing the device fabrication procedure to obtain state of the art MoS<sub>2</sub> field effect transistors. Chapter 6 uses the techniques established in Chapter 5 to develop the best MoS<sub>2</sub> devices with phase engineered contacts. Chapter 7 has the analysis of contact resistance and schottky barrier height measurements. It also details on top gated devices with MoS<sub>2</sub>. Chapter 8 discusses the application of this technique to CVD grown MoS<sub>2</sub> and other TMD semiconductors. Finally Chapter 9 completes the thesis with future work and conclusions.

## Chapter 2

### 2.1 Layered Materials

Layered materials are defined as materials which have strong in-plane bonds but weak out-of-plane bonds<sup>8</sup>. Graphite, for instance, has strong covalent bonds between each of the atoms, but has weak van der Waals forces of attraction between the layers. It is because of this property that it is easy to exfoliate graphite to form graphene, which is a single layer of graphite. Other examples of layered materials are transition metal dichalcogenides<sup>9-15</sup> (TMDCs), transition metal oxides<sup>16</sup>, topological insulators<sup>17</sup>, silicene<sup>18,19</sup>, germanene<sup>20</sup>, phosphorene<sup>21</sup> (two dimensional allotropes of silicon, germanium and phosphorous respectively) and hexagonal boron nitride<sup>22</sup>. These materials have long been studied due to their extensive optical, electrical, chemical and thermal properties<sup>23-26</sup>. Due to the recent advances in exfoliation there has been a resurgence in the research of these materials, particularly the category of TMDCs<sup>4, 7,27-36</sup>. This is mainly due to the additional interesting characteristics found in single layers of these materials; properties that arise due to quantum confinement effects. These monolayered materials have higher surface areas, resulting in improved surface activity<sup>37-39</sup>. Unlike 3D semiconductors which have variations when scaled to nano-dimensions, 2D semiconductors offer controllable band gaps which lead to novel applications<sup>8,11</sup>. As the carriers are confined to this sub-nanometer thickness, they offer excellent gate electrostatics with reduced short channel effects<sup>40-43</sup>. These characteristics of 2D materials make the future for green electronics possible which will enable energy and fuel savings.

## 2.2 Graphene

Graphene was the first material that raised interest in layered materials. It was initially studied in 2004 by researchers Andre Geim and Konstantin Novoselov in Manchester, UK, and the study of the physics<sup>44</sup> related to single-layer graphene eventually led them to win the Nobel Prize in 2010. It is a single sheet of closely knitted  $sp^2$  carbon atoms in a hexagonal pattern where all the carbon atoms are well saturated, resulting in no dangling bonds on the surface. This characteristic result of graphene having no interface traps made it the most suitable material for high frequency electronics<sup>45-47</sup>, and RF applications<sup>48-50</sup>. Graphene can be easily exfoliated from a single crystal of highly ordered pyrolytic graphite (Fig 2.1a) using scotch tape<sup>51</sup>. Figure 2.1b shows the honeycomb lattice of graphene and fig. 2.1c shows the linear E-k diagram of graphene and the dirac cone where the electrons and hole act like mass-less particles<sup>52</sup>. It is simultaneously an excellent conductor of electricity, with sheet resistance of less than  $30 \Omega/\text{sq}$ , and nearly transparent, with an optical transmission of  $>90\%$ <sup>53</sup>. This high degree of optical transmission makes it a viable competitor in the race to replace Indium tin oxide (ITO) as a transparent conductor. Other advantages of graphene which make it a better replacement for ITO include its low cost of fabrication when using a chemical vapor deposition (CVD) process<sup>54</sup>, high electron mobility ( $>3000 \text{ cm}^2/\text{Vs}$  for CVD graphene<sup>28,55</sup>), and high thermal and mechanical flexibility<sup>56</sup>. Researchers have also used graphene electrodes in touch panels<sup>31</sup>, displays<sup>57</sup>, solar cells<sup>58</sup>, and bio-sensors<sup>59</sup>, applications that help showcase the wide range of applications for this material.

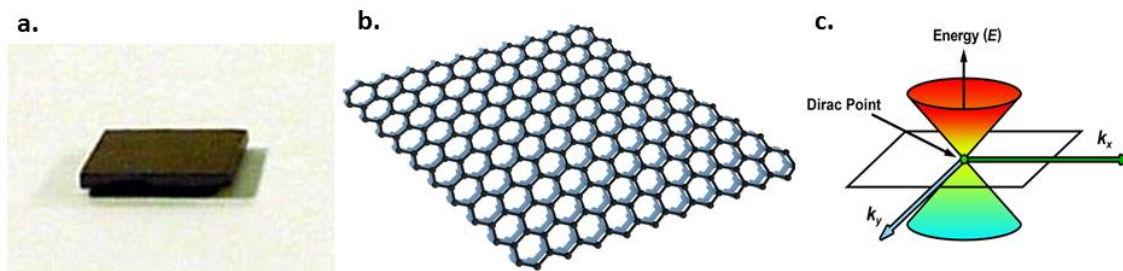


**Fig 2.1: Graphene crystal, structure and E-k diagram** a) Picture of highly ordered pyrolytic graphene from SPI supplies inc. b) A sheet of graphene showing the honey comb lattice of carbon atoms. c) E-k diagram of graphene showing zero band gap and E-k linearity at the Dirac point

### 2.3 Layered Transition Metal Dichalcogenides (LTMDs)

Graphene is a semi-metal with a zero band gap. Due to this intrinsic property, it is not possible to switch off the devices with graphene as the channel material, resulting in very poor ON/OFF ratio<sup>28,60-63</sup>, Fig 2.2a, b shows the FET characteristics of graphene devices<sup>64,65</sup>. Although a band gap can be introduced into graphene by making graphene nano-ribbons<sup>66</sup> (10nm wide GNRs have band gap of 0.1eV), these nanostructures are extremely complex to make and will result in a loss of mobility. Fig. 2.2c shows the band gap value as a function of GNR diameter.

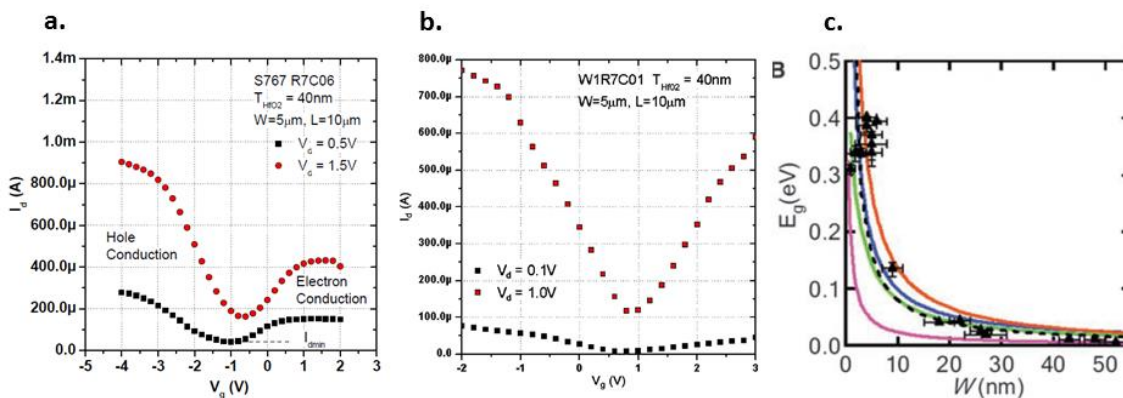


**Fig 2.2: Graphene Electrical Properties** a) FET transfer characteristic of multilayer epitaxial graphene b) FET transfer characteristic of CVD graphene for two different drain-source voltages c) Band gap variation in GNR as a function of its width. Reproduced from Ref. 64, 65 and 66.

With these challenges in mind, many researchers have shifted their interest to other two-dimensional materials<sup>67-72</sup>, these alternatives are mainly comprised of the transition metal dichalcogenides (TMDs) which have diverse properties that range from semiconductors such as MoS<sub>2</sub>, WS<sub>2</sub>, MoSe<sub>2</sub>, semi-metals such as WTe<sub>2</sub> and TiSe<sub>2</sub>, insulators such as HfS<sub>2</sub>, and true metals such as NbS<sub>2</sub> and VSe<sub>2</sub><sup>8,11,73,74</sup>. They have the general formula of MX<sub>2</sub> and have a layered structure in the form of X-M-X where M is a transition metal from group IV, V or VI sandwiched between two layers of X, which is a chalcogen (S, Se or Te)<sup>41</sup>. Adjacent layers of these TMDs are weakly held together by van der Waals forces, which results in relatively easy exfoliation. There are approximately 40 members in the family of TMDs which include semiconductors (with varying band gaps and naturally abundant), semimetals, metals, superconductors, and topological insulators (Fig 2.3)<sup>41</sup>. For semiconductors, the nature of the band gap changes with variation in layer thickness, going from an indirect band gap while in the bulk material to a direct band gap in a single layer<sup>75</sup>. Interestingly, we can have direct band gap semiconductors that vary in band gap from 1.1 eV to 2.2 eV<sup>11,41</sup>. Table 2.1 shows different LTMD semiconductors with gradually increasing band gaps.

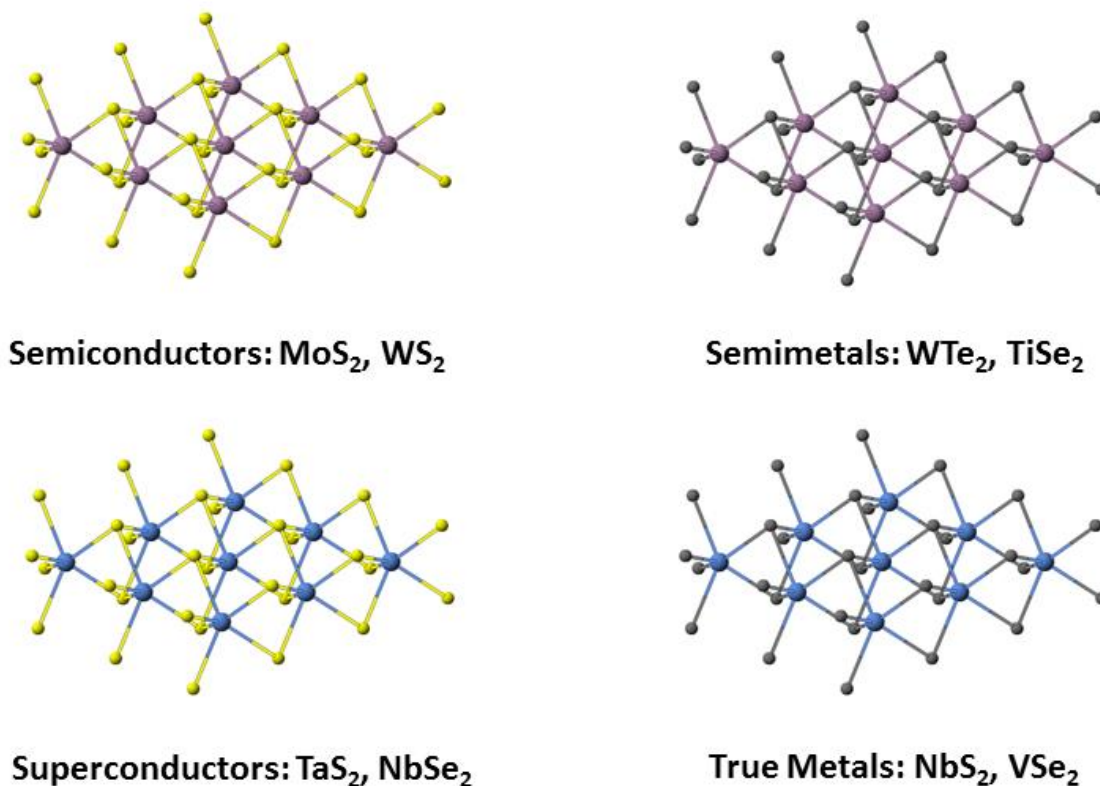


**Fig 2.3: Properties of Transition metal dichalcogenides family**

**Table 2.1: Band gaps of bulk and single layer LTMD semiconductors**

LTMD	Bulk band gap (eV)	Single layer band gap(eV)
MoTe <sub>2</sub>	1.0	1.1
MoSe <sub>2</sub>	1.1	1.5
WSe <sub>2</sub>	1.2	1.6
MoS <sub>2</sub>	1.2	1.8
WS <sub>2</sub>	1.4	2.1
SnS <sub>2</sub>	2.1	2.2

The band gap of these monolayer LTMDs can be tuned by varying the composition<sup>76</sup> and functionalization<sup>77</sup> of the materials, as well as by the application of external electric fields. Since sizeable band gaps are extremely important for the areas of field-effect transistors (FETs) and optoelectronic devices<sup>48,78-80</sup>, these intrinsic properties are among the main attractions for a shift in focus from zero-bandgap graphene to these LTMDs. Fig. 2.4 shows

the band alignment for four TMD semiconductors, such a perfect band alignment makes them extremely suitable for thin film solar cells.

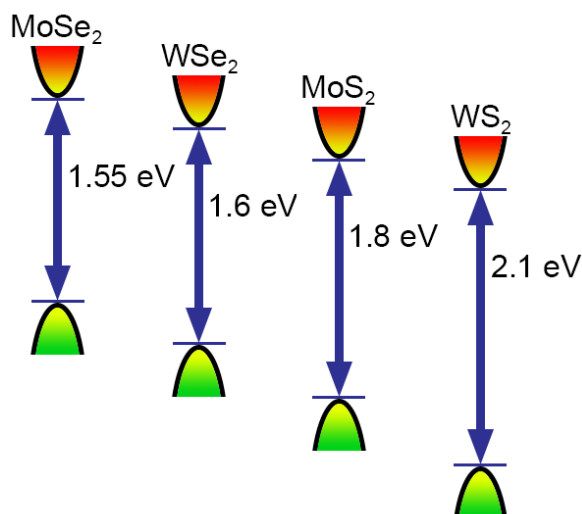


**Fig 2.4: Band alignment of WSe<sub>2</sub>, MoSe<sub>2</sub>, WS<sub>2</sub> and MoS<sub>2</sub>**

## 2.4 Chapter summary

This chapter gave a brief introduction to layered materials and described the properties and advantages of them over the conventional bulk semiconductors. A brief summary of applications of graphene has been given and the reasons why graphene cannot be used for electronic applications have been discussed. This was followed by the introduction of the family of transition metal dichalcogenides. The structure of a TMD material and some important members of the TMD semiconductor family were familiarized.

## Chapter 3

### 3.1 Molybdenum disulfide (MoS<sub>2</sub>)

One of the most studied and widely used LTMD has been molybdenum disulfide (MoS<sub>2</sub>). It has distinctive electrical, optical, chemical and mechanical properties, properties which make it attractive to be used as a hydrodesulphurization catalyst<sup>33,81,82</sup> as active materials or transport

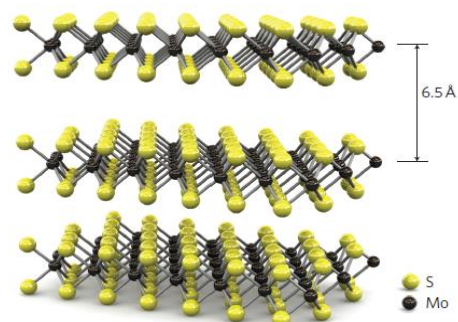


**Fig 3.1: MoS<sub>2</sub> crystal structure. Reproduced from Ref. 95**

material in solar cells<sup>83,84</sup>, as photocatalysts<sup>85</sup>, as electrodes in lithium batteries<sup>86</sup>, and as a solid lubricant<sup>87</sup>. Similar to other LTMDs, bulk MoS<sub>2</sub> is an indirect band gap semiconductor with a band gap value of 1.2 eV<sup>88-91</sup>. When exfoliated to a monolayer, the nature of the band gap changes from indirect to direct band gap<sup>92,93</sup> with a value of 1.9 eV. This effect has led to strong resurgence in the research of monolayer MoS<sub>2</sub> due to its potential application in the field of 2D devices, even though MoS<sub>2</sub> in its bulk form has already been studied extensively in the past<sup>9,94</sup>. The existence of this intrinsic band gap in monolayer MoS<sub>2</sub> has led to field effect transistors which have a high ON/OFF ratio of 10<sup>8</sup><sup>95-98</sup> and application in sensors<sup>99,100</sup> integrated circuits<sup>101</sup> and logic operations<sup>102</sup>. The direct band gap of monolayer MoS<sub>2</sub> has enabled it to exhibit photoluminescence<sup>12,103</sup> and has favored it for use in optoelectronic applications<sup>104,105</sup>. Recently, valley polarization was achieved in monolayer MoS<sub>2</sub> by optically exciting electrons with a circularly polarized light<sup>106</sup>; this development can potentially lead to many new applications in the exciting field of valleytronics.

### 3.2 Structure of MoS<sub>2</sub>

Bulk MoS<sub>2</sub> is composed of layers of monolayer MoS<sub>2</sub> weakly bonded by inter-layer van der Waals forces. Each monolayer of MoS<sub>2</sub> consists of hexagonally packed S-Mo-S units<sup>18,95</sup>. These layers are held together in different stacking orders which results in the Mo atom coordination to be trigonal prismatic or octahedral with overall symmetry of the unit to be hexagonal, rhombohedral, or tetragonal, depending on the orientation<sup>107</sup>. This work would deal with two polymorphs of MoS<sub>2</sub>, which are the 2H (hexagonal) phase and the 1T (trigonal) phase, since monolayer MoS<sub>2</sub> exhibits only these two types. Figure 6 shows the 2H structure of MoS<sub>2</sub> which as a whole exhibits hexagonal symmetry and the Mo atom has trigonal prismatic coordination. This phase has 2 layers per unit and as such is named 2H. There are six S atoms bonded to each Mo atom; in the 2H phase the S atoms below the Mo atom are positioned exactly below the three S atoms which are bonded above the Mo atom, as shown in fig. 3.2a; because of this orientation when the structure is viewed from the top we can see only three sulfur atoms bonded to Mo atom (Fig 3.2b). Bulk MoS<sub>2</sub> exists in this 2H phase and since the d orbitals are fully occupied, it behaves as a semiconductor<sup>12</sup>.

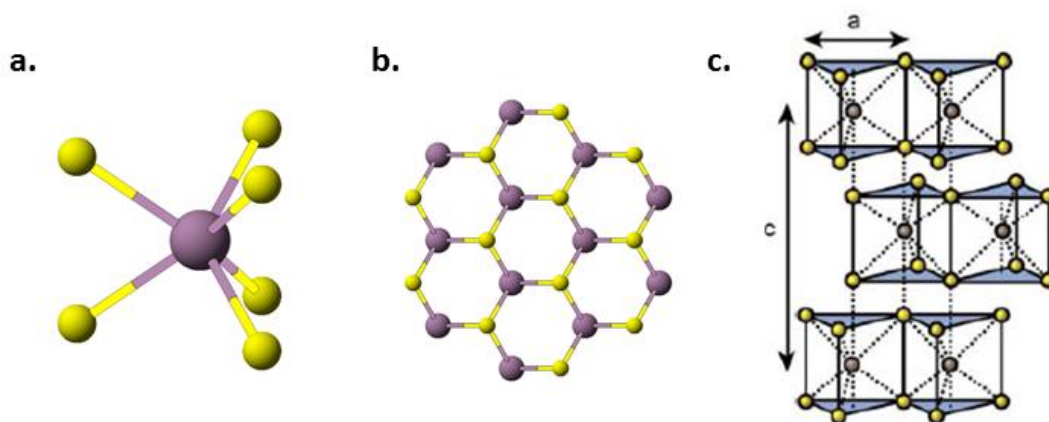


**Fig 3.2: 2H structure of MoS<sub>2</sub> a) 3D model of one unit of 2H MoS<sub>2</sub> b) 2D top view of 2H MoS<sub>2</sub> c) 3 layers of 2H MoS<sub>2</sub> to show the 2 layers per unit hexagonal structure. Reproduced from Ref. 11**

Fig 3.3 shows the 1T structure of MoS<sub>2</sub> which exhibits tetragonal symmetry where Mo atom has octahedral coordination. This phase has 1 layer per unit and hence is named 1T. This structure is analogous to the 2H phase, but with the bottom plane of sulfur atoms rotated by 60° with respect to the top plane of atoms<sup>108</sup>; because of this when viewed from top we can see all the six sulfur atoms bonded to the Mo atom. This 1T phase is a metastable phase of MoS<sub>2</sub> and is metallic in nature<sup>5</sup>.

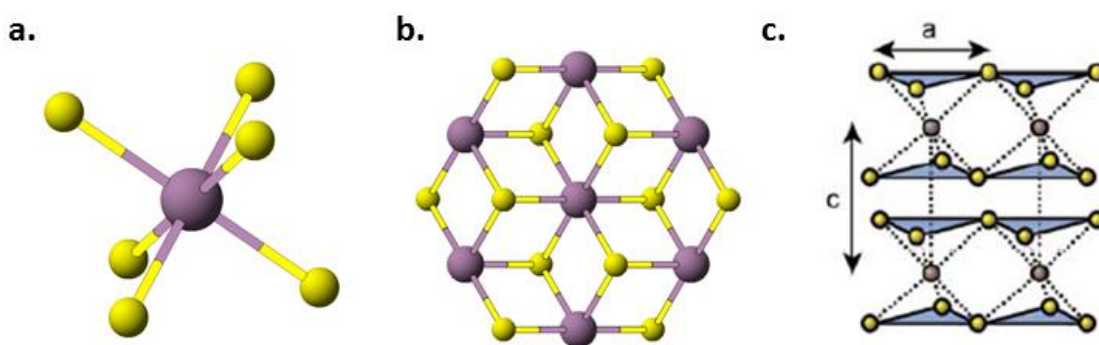


**Fig 3.3: 1T structure of MoS<sub>2</sub> a) 3D model of one unit of 1T MoS<sub>2</sub> b) 2D top view of 1T MoS<sub>2</sub> c) 2 layers of 1T MoS<sub>2</sub> to show the 1 layer per unit tetragonal structure. Reproduced from Ref. 11**

### 3.3 Synthesis methods

#### 3.3.1 Top-down approach

**Mechanical Exfoliation:** One of the most familiar and easy way of obtaining monolayers of these layered crystals (graphene, MoS<sub>2</sub>, WS<sub>2</sub>, etc) is through mechanical exfoliation, which is also known as the “scotch tape method”. MoS<sub>2</sub> single crystals are bought from SPI supplies, a company that obtains them from deposits in Canada<sup>109</sup>. Figure 8a shows the image of a high quality single crystal of MoS<sub>2</sub>. Monolayer or few-layer flakes can be obtained by mechanically peeling off layers from the bulk crystal through the aid of scotch tape or similar adhesive tapes and eventually transferring them to substrates by applying pressure<sup>110-112</sup>. Figure 3.4b shows the image of a scotch tape with layers of MoS<sub>2</sub> on it<sup>113</sup>.

Monolayers can be identified through the use of optical microscopes by noting the significant contrast changes that occur as the number of layers changes<sup>110-116</sup>. An example of the contrast change in a MoS<sub>2</sub> flake is shown in Fig 3.4 where MoS<sub>2</sub> flakes are transferred onto a 300 nm Si/SiO<sub>2</sub> substrate. This is the best method to get flakes with the highest purity and cleanliness, thereby making it the ideal choice for studying the fundamental properties of these materials and for demonstrating high performance devices. However, this method is not scalable and there is no proper control of size and thickness of the flake.

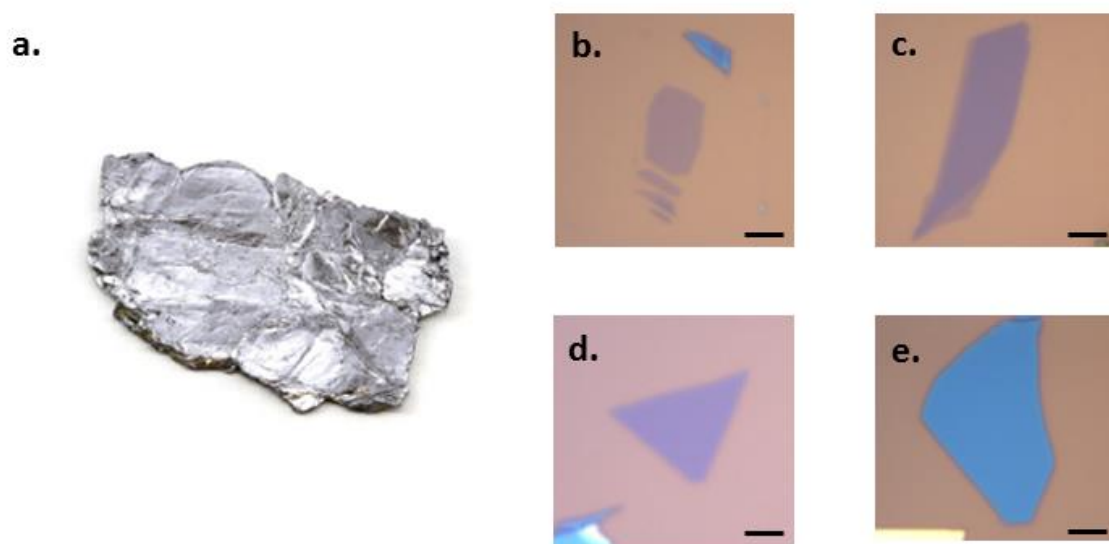


**Fig 3.4:** a) Single crystal of MoS<sub>2</sub>. Optical microscope images of b) single layer, c) bilayer d) trilayer and e) four layered MoS<sub>2</sub> flakes showing the change in contrast as thickness varies on 300 nm oxide capped Si substrates. All scale bars are 5µm in length. Reproduced from Ref. 113

**Solvent based exfoliation:** Solvent based exfoliation methods are preferred for applications where a high quantity of exfoliated nanosheets is required<sup>117-120</sup>. Ultra-sonication of bulk powders of TMDs with an organic solvent, preferably one which has surface energy comparable to the TMD, results in exfoliation<sup>38</sup>. However, the yield of monolayers is very low with this method and the size of the nanosheets is very small. This is because sonication

is very strong on the flakes leading to cracking of the flakes to nanosizes. Fig 3.5 shows the solutions of TMDs exfoliated in this method and the films made with these solutions.



**Fig 3.5: TMD Solutions prepared by ultra-sonication with organic solvents and corresponding films. Reproduced from Ref. 118**

Another interesting method of exfoliating TMDs is through alkali metal intercalation. Lithium intercalation into TMDs, especially for MoS<sub>2</sub>, has been extensively studied since the 70's<sup>121-125</sup>; Joenson et al had exfoliated MoS<sub>2</sub> by performing lithium intercalation through the use of n-butyl lithium dissolved in hexanes<sup>126</sup>. The intercalated material is termed Li<sub>x</sub>MoS<sub>2</sub> and is cleaned thoroughly with hexane to remove any organic residues. MoS<sub>2</sub> is readily exfoliated when this product is sonicated in water as the intercalated lithium reacts with water to produce hydrogen gas<sup>12</sup>. The resulting gas then easily separates the flakes because the layers are attached together by weak van der Waals forces. This separation is then followed by centrifugation to further separate the unexfoliated material, which is forced down to the bottom of the container. Fig 3.6 shows the solutions of various TMDs prepared using this method.



**Fig 3.6: TMDs prepared by lithium intercalation based exfoliation. Reproduced from Ref. 14.**

This process has a very high yield of monolayers but due to the harshness of sonication and centrifugation it suffers from the same issues of liquid exfoliation of having very small sized flakes. Furthermore, due to lithium intercalation into the material, the structure of MoS<sub>2</sub> changes from 2H to 1T. Films can be made using vacuum filtration process where the solution is filtered through a 25 nm pore membrane. The flakes are stitched together on the membrane to form a film which can be delaminated and transferred onto any substrates. Fig 3.7a shows the AFM image of such a film transferred on Si/SiO<sub>2</sub> substrate. Films made through this process are metallic (1T phase) in nature and will show no photoluminescence, unlike mechanically exfoliated single layer MoS<sub>2</sub> which has strong photoluminescence. However, since the 1T phase is metastable, the 2H structure is restored upon annealing the films in inert atmosphere, a change that is evident by the re-emergence of the photoluminescence peak<sup>12</sup>. Fig 3.7b shows the emerging photoluminescence as the films are annealed at gradually high temperatures causing gradual restoration of 1T MoS<sub>2</sub> to 2H MoS<sub>2</sub>. As made films are very conductive because they are metallic and as we anneal the 1T phase relaxes causing the conductivity to reduce. This can be seen in Fig 3.7c.

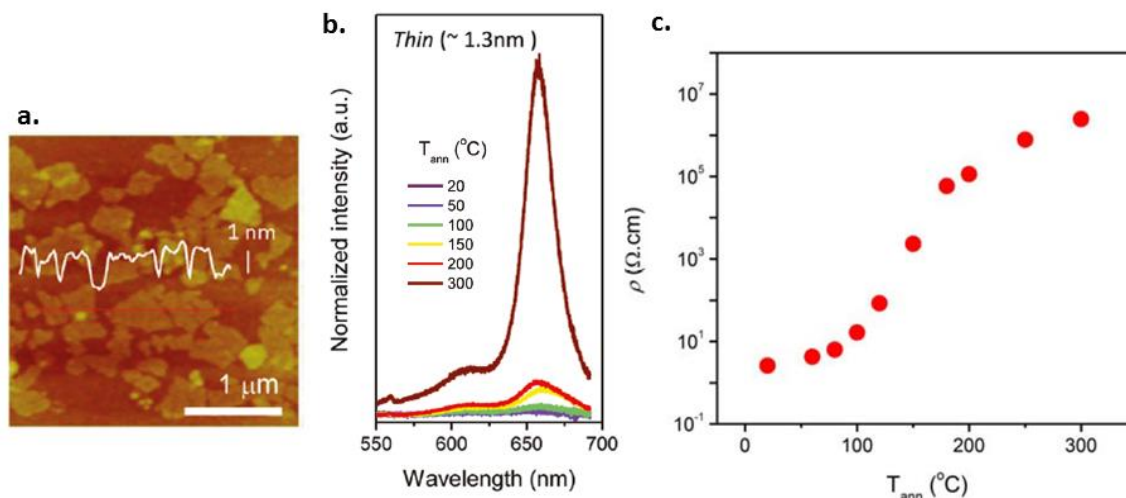


**Fig 3.7:** a) AFM image of MoS<sub>2</sub> film made on Si/SiO<sub>2</sub> substrate b) Emerging photoluminescence as a function of annealing temperature on MoS<sub>2</sub> films c) Resistance of MoS<sub>2</sub> film as a function of annealing temperature. Reproduced from Ref. 12.

### 3.3.2 Bottom up approach

**Chemical vapor deposition:** In order to enable large scale device fabrication, it is essential to develop chemical vapor deposition methods for growing TMDs. In the case of graphene, copper acted as a perfect catalyst to grow large area high quality graphene since it provided a perfect surface for carbon to form soft bonds<sup>127-131</sup>, but the resulting graphene sheet needed to be transferred onto insulating substrates for device fabrication which usually results in contamination and cracking of graphene. In the case of MoS<sub>2</sub>, CVD synthesis methods have been demonstrated in which different solid precursors were heated to a high temperature and allowed to react in order to form MoS<sub>2</sub><sup>11,14,132-134</sup>. Various CVD synthesis methods have been reported to obtain single layers of MoS<sub>2</sub> which are described below.

Liu et al have employed a two-step thermolysis process for growing MoS<sub>2</sub><sup>135</sup>: A film of ammonium thiomolybdate was made on a silicon substrate, which was then annealed at 500 °C for an hour under inert conditions and annealed again in the presence of sulfur vapor at 1000 °C to form a tri-layered MoS<sub>2</sub> film. Schematic of the growth mechanism and sample

images are shown in fig 3.8a. Another method of growing  $\text{MoS}_2$  is through the sulfurization of thin films of Mo metal<sup>136</sup>. The sulfur species are chemisorbed into Mo and then allowed to diffuse throughout the film. The rate of sulfur diffusion is determined by the furnace pressure and temperature used. Fig 3.8b shows the schematic of the growth mechanism and images of  $\text{MoS}_2$  film on Si/SiO<sub>2</sub> substrates. The most familiar and relatively straightforward method for growing  $\text{MoS}_2$  flakes is by vaporizing  $\text{MoO}_3$  and sulfur powders in a furnace under the flow of argon gas<sup>137-139</sup>.  $\text{MoO}_3$  is reduced and reacts with sulfur vapor to form  $\text{MoS}_2$ , which is then deposited onto a substrate placed close to the precursor. Fig 3.8c shows the furnace schematic and flake images formed by this process on Si/SiO<sub>2</sub> substrates. This method gives  $\text{MoS}_2$  flakes which are triangular in shape. By varying the amounts of sulfur fed into the furnace it is possible to grow  $\text{MoS}_2$  flakes which are terminated by Mo edges and flakes which are terminated by S edges. These images are shown in fig 3.8d, Mo terminated flakes have sharp edges whereas S terminate flakes have curved edges<sup>141</sup>. This is very important for the study of processes like catalysis where edge defects play a major role in the catalytic properties of the materials.

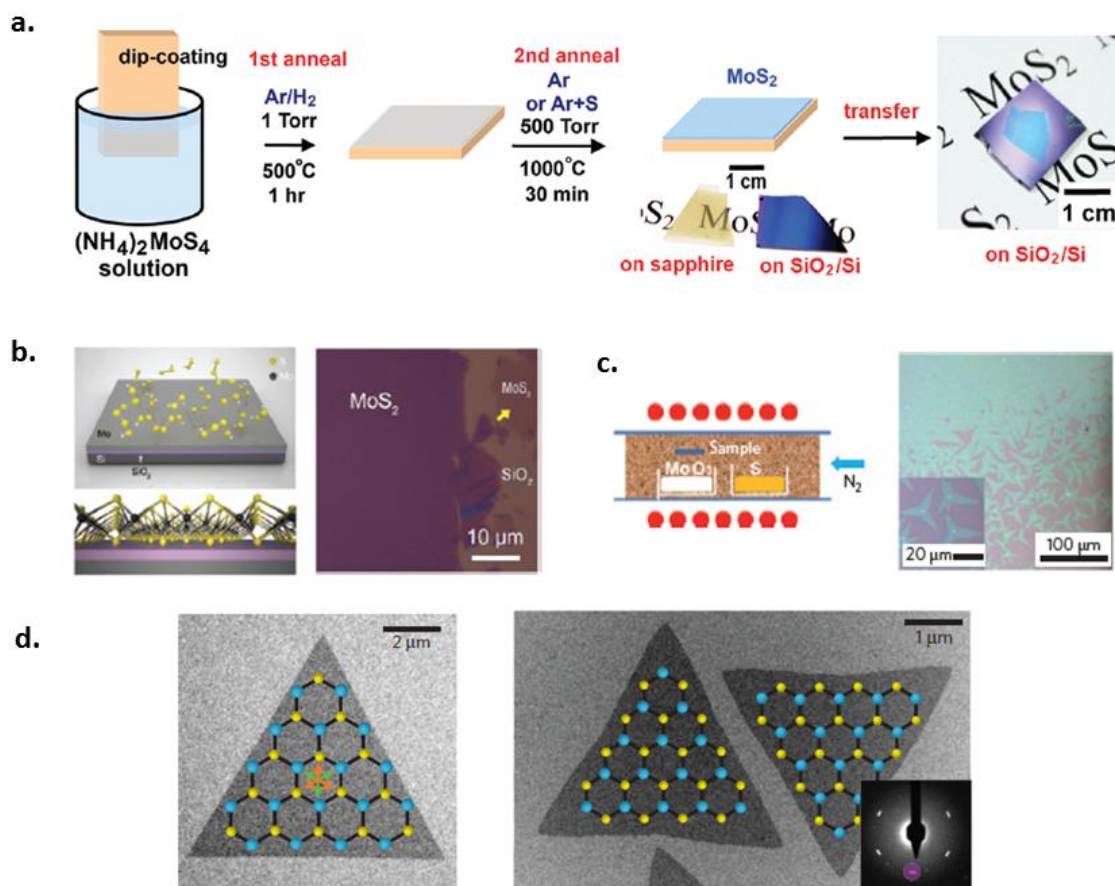


**Fig 3.8:** a) Growth of thin film of MoS<sub>2</sub> by dip coating with ammonium thiomolybdate b) MoS<sub>2</sub> growth obtained by sulfurization of a thin Mo metal film on Si/SiO<sub>2</sub> substrate c) Reaction of MoO<sub>3</sub> and S powders in a tube furnace to obtain single layers of MoS<sub>2</sub> d) Bright field images of MoS<sub>2</sub> flakes terminated with Mo edges (straight sharp edges) and S edges (curved edges). a, b, c, d reproduced from Ref. 135, 136, 137 and 141 respectively.

## 3.4 Optical Spectroscopy on MoS<sub>2</sub>

### 3.4.1 Raman Spectroscopy

#### *Variation of MoS<sub>2</sub> Raman spectra with flake thickness*

MoS<sub>2</sub> has two strong active Raman modes – namely the E<sub>2g</sub><sup>1</sup> and A<sub>1g</sub> peaks which peak around 400 cm<sup>-1</sup>. E<sub>2g</sub><sup>1</sup> represents in plane vibrational mode which occurs at 384 cm<sup>-1</sup>, whereas the A<sub>1g</sub> is the out of plane vibration and occurs around 404 cm<sup>-1</sup>. The behavior of these two peaks varies as a function of flake thickness; this property has been used extensively to identify monolayers of MoS<sub>2</sub> after either mechanical exfoliation or chemical vapor deposition. From fig 3.9a we can see that the E<sub>2g</sub><sup>1</sup> mode red shifts and the A<sub>1g</sub> mode blue shifts. The stiffening of the A<sub>1g</sub> mode can be explained by the classical model of coupled harmonic oscillators. As the number of layers is increased to make a thick flake of MoS<sub>2</sub>, there is an increase in the restoring forces acting on the atoms which then results in the reduction in the intensity of vibrations that the A<sub>1g</sub> mode blue shifts. This theory, however, does not apply to the E<sub>2g</sub><sup>1</sup> mode; this property suggests that there are additional interlayer interactions. The behavior of the E<sub>2g</sub><sup>1</sup> mode has been attributed to the long range Coulombic interlayer interactions. This difference in the peak positions of E<sub>2g</sub><sup>1</sup>, A<sub>1g</sub>, and Δw, can be used as a robust and effective diagnostic to determine the flake thickness<sup>142</sup>. Usually Δw is less than 20 cm<sup>-1</sup> for a single layer flake and will increase considerably as the flake thickness increases – a phenomenon that is demonstrated in fig. 3.9b.

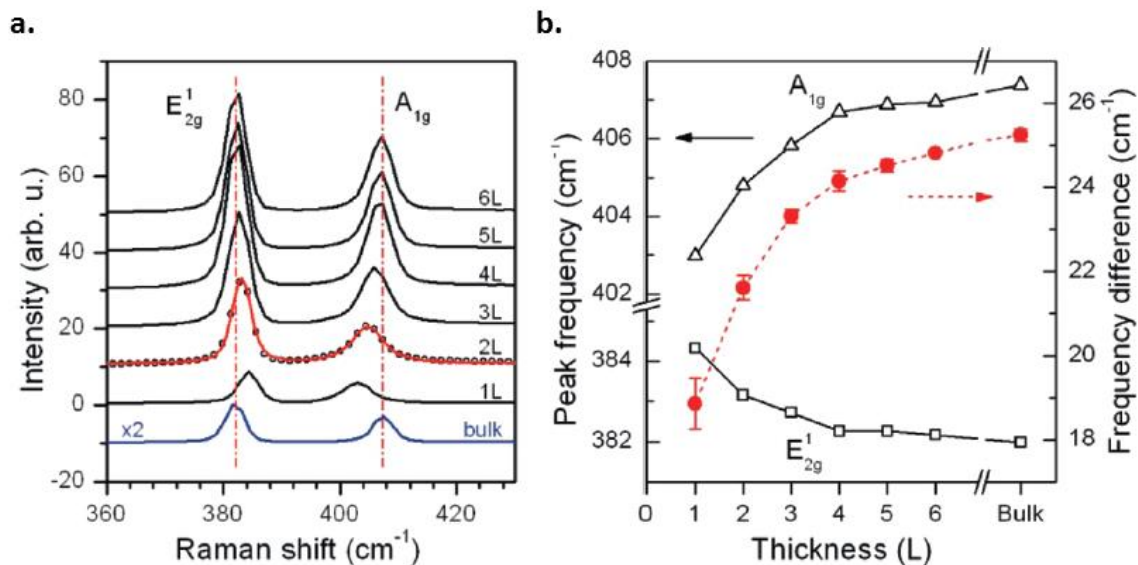


**Fig 3.9:** a) Variation in MoS<sub>2</sub> Raman spectra as the layer thickness changes b) Change in the position of the Raman peaks and frequency difference between them as a function of MoS<sub>2</sub> layer thickness. Reproduced from Ref. 142.

#### *Variation of MoS<sub>2</sub> Raman spectra with phase*

The Raman spectra of 1T MoS<sub>2</sub> is very different than 2H MoS<sub>2</sub>, however; this is due to the different symmetry of S atoms around the Mo atom<sup>108</sup>. For the as-made solution processed films which are phase transformed during the lithium intercalation process, the Raman spectrum resembles that of 1T MoS<sub>2</sub><sup>12</sup>. There are three strong peaks that correspond to 156 cm<sup>-1</sup> (J<sub>1</sub>), 226 cm<sup>-1</sup> (J<sub>2</sub>), and 330 cm<sup>-1</sup> (J<sub>3</sub>). The peak at 384 cm<sup>-1</sup>, which corresponds to E<sub>2g</sub><sup>1</sup> in 2H MoS<sub>2</sub>, is very weak in 1T MoS<sub>2</sub>. This peak corresponds to the trigonal prismatic coordination of 2H MoS<sub>2</sub> and since the coordination of Mo is octahedral in 1T MoS<sub>2</sub>, this peak is infrared active rather than Raman active<sup>108</sup>. Figure 3.10 shows the Raman spectra of 1T MoS<sub>2</sub>.

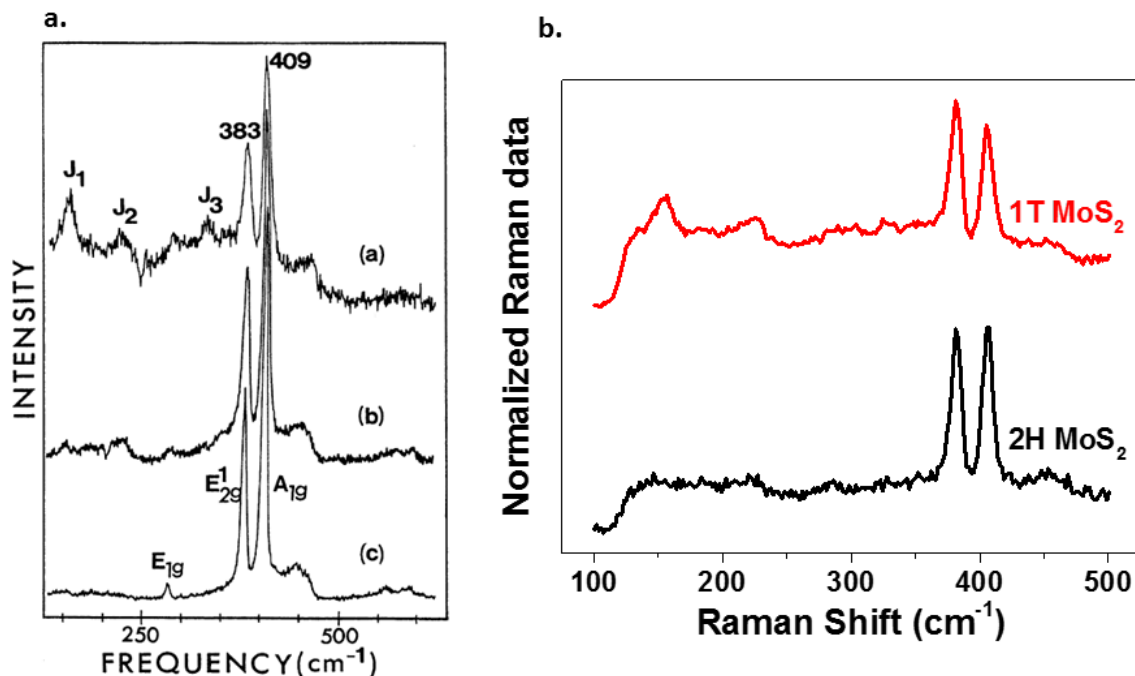


**Fig 3.10:** a) Raman spectra of freshly made and stacked films of MoS<sub>2</sub>. The 1T phase gradually relaxes to 2H with time. b) Raman spectra of as made MoS<sub>2</sub> film (1T) and annealed MoS<sub>2</sub> film (2H). Reproduced from Ref. 108.

### 3.4.2 Photoluminescence

Photoluminescence on MoS<sub>2</sub> would be an ideal test for observing the indirect to direct band gap conversion when going from bulk to single layer. This method has been studied by Splendani et al in 2010<sup>92</sup> on mechanically exfoliated MoS<sub>2</sub> flakes and Eda et al in 2011<sup>12</sup> on solution processed MoS<sub>2</sub> films. Both groups have demonstrated that as the flake/film thickness reduces from multilayer to monolayer there is a strong photoluminescence peak that emerges at 1.8-1.9 eV, corresponding to the direct band gap on single layer MoS<sub>2</sub>. Fig 3.11 shows the photoluminescence peak as a function of flake/film thickness for mechanically exfoliated flakes and solution processed films.

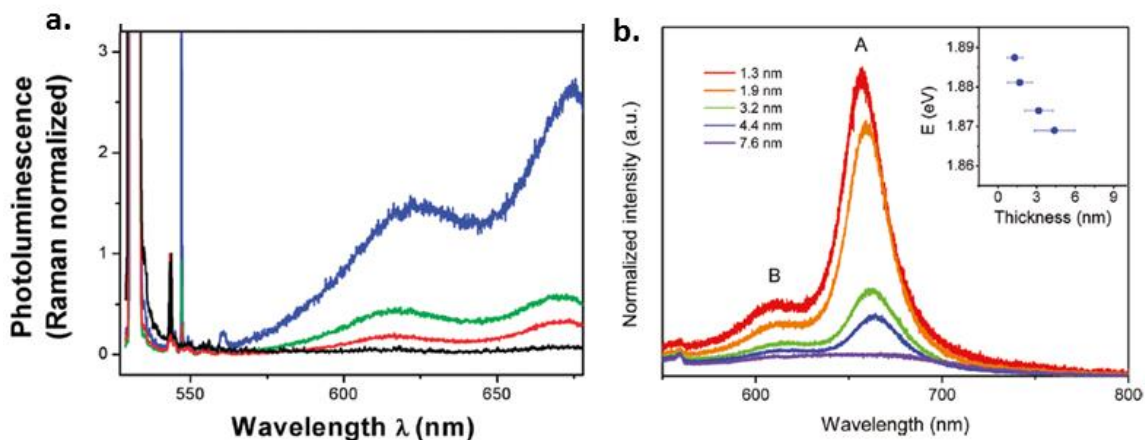


**Fig 3.11:** a) Photoluminescence as a function of flake thickness on mechanically exfoliated MoS<sub>2</sub> flakes (Black-bulk, red-tri-layer, green-bi-layer and blue is monolayer MoS<sub>2</sub>). b) Emerging photoluminescence as the film thickness is reduced in the case of solution processed MoS<sub>2</sub> films. Inset shows the band gap change as film thickness is reduced. a, b reproduced from Ref. 92, 12.

In the case of solution processed films, the as-made films do not show any luminescence as they are metallic in nature (1T phase). As the films were progressively annealed, the luminescence begins to merge and is the brightest when the 1T phase completely transforms to 2H as shown in fig. 3.7b earlier.

This photoluminescence of MoS<sub>2</sub> can be enhanced by making a Ag@SiO<sub>2</sub> core shell composite. The Ag@SiO<sub>2</sub> nanoparticles are physically adsorbed on the MoS<sub>2</sub> surface, thus enabling metal-enhanced fluorescence. This demonstrates a great potential for these TMD materials to be used in applications such as photovoltaics and bioanalysis<sup>143</sup>.

### 3.5 Electrical Characterization

Since the introduction of the first silicon-based transistor by Bell Laboratories in 1954, the device itself went into many modifications based on its design, channel length, and the number of devices per processor. Present state-of-the-art integrated chips have two billion devices with channel lengths of just 30nm<sup>144</sup>. However, the reductions of channel lengths and the increase of the number of devices per processor will soon reach their limits due to quantum confinement, short channel effects, and heat dissipation related issues<sup>145-147</sup>. Henceforth, there is a necessity to start research on new device concepts and materials. There have been reports of high performance graphene field-effect transistors (GFETS)<sup>148</sup> by researchers all over the world. As graphene is a two dimensional material, when it is coupled with a thin insulating oxide on top it will result in a device which will not have short channel effects<sup>149</sup>. Mobilities of 10,000~15,000 cm<sup>2</sup>/Vs have been measured for devices on mechanically exfoliated graphene sheets on SiO<sub>2</sub>/Si substrates<sup>51,150</sup> whereas suspended graphene showed mobilities up to 1,000,000 cm<sup>2</sup>/Vs<sup>151</sup>. One major issue with graphene is that since it is a zero band gap semi-metal, the devices made with graphene as the semiconductor cannot be switched off, thus making them unsuitable for logic operations. Though a band gap can be introduced to graphene when it is made as a nanoribbon, the electrical properties are significantly affected due to edge effects giving rise to a low mobility<sup>40</sup>.

As such there came the need for layered materials which could be exfoliated into single layers and have a sizeable band gap comparable to silicon. This would then enable the devices to be completely turned off while retaining high mobilities and make them efficient for use in logic operations. The family of transition metal dichalcogenides (MoS<sub>2</sub>, WS<sub>2</sub>,

MoSe<sub>2</sub>, WSe<sub>2</sub> etc.) had these properties and so huge interest in studying them in detail, especially MoS<sub>2</sub>, has begun.

## MoS<sub>2</sub> transistors

One of the first reports of transistors on LTMDs came out in 2007 by Ayari et al where they mechanically exfoliated thin crystals of MoS<sub>2</sub> (8 to 40 nm in thickness), made contacts through e-beam lithography, and then deposited 2.5 nm of Chromium and 100 nm of gold. They observed only n-type transport even though a gate voltage of -50V was applied. In addition, they reported mobilities of up to 50 cm<sup>2</sup>/Vs<sup>152</sup> and an ON/OFF ratio of above 10<sup>5</sup> with a back gated configuration. In 2010 a research group led by Kis fabricated top-gated monolayer MoS<sub>2</sub> transistors with HfO<sub>2</sub> as the dielectric and obtained mobilities in the range of 15 cm<sup>2</sup>/Vs (corrected from earlier reported high value of 200 cm<sup>2</sup>/Vs), high ON/OFF ratios in order of 10<sup>8</sup>, and high ON currents of around 2.5 μA/μm at a drain source voltage of 0.5 V. The device configuration and electrical characteristics are shown in fig 3.12. Their devices also showed a sharp turn-on as observed from the low sub-threshold slope of 74 mV/dec<sup>95</sup>. Such efficient device characteristics have shown promise for 2D materials to be realized in future electronics where low-standby-power integrated circuits would be required.

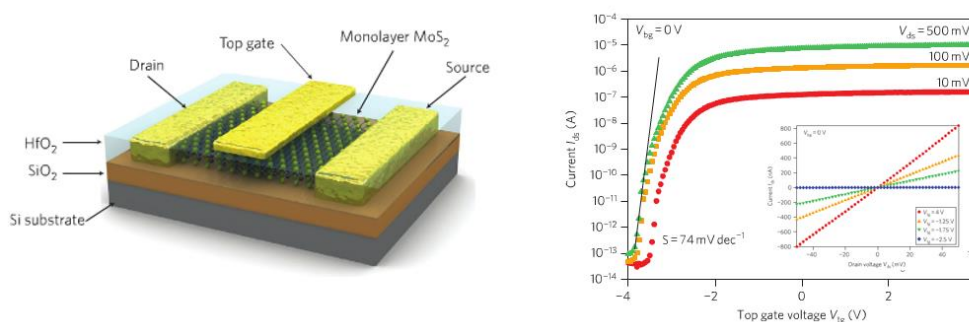


**Fig 3.12: Device configuration and electrical characteristics of single layer mechanically exfoliated MoS<sub>2</sub>. Reproduced from Ref. 95.**

Yoon et al have done quantum transport simulations using non-equilibrium Green's function to determine the scaling limits of single layer (SL) MoS<sub>2</sub> transistors. SL MoS<sub>2</sub> transistors have low transconductance, high on/off ratios, and good short channel behavior, making them very suitable for low power applications<sup>153</sup>. To demonstrate that MoS<sub>2</sub> transistors are immune to short channel effects, Liu et al fabricated devices with channel lengths up to 100 nm and claimed no short channel effects. They further reported that the performance limit in MoS<sub>2</sub> transistors is due to the high contact resistance between metal and the semiconductor and as such a fully transparent contact is required to make a high performance short channel device<sup>154</sup>. Das et al fabricated MoS<sub>2</sub> transistors with different metals as the contacts and found that Fermi level pinning at the conduction band of MoS<sub>2</sub> strongly influences the metal semiconductor interface. They achieved the best device performance for Scandium contacts owing to high carrier injection and low contact resistance of 0.65 KΩ-μm<sup>155,156</sup>. Another interesting approach for making low contact resistance devices is to degenerately dope the contact regions of MoS<sub>2</sub>, as was done by Fang et al where they doped the devices with potassium and achieved much better device performances from MoS<sub>2</sub><sup>157</sup>. Device structure and electrical characteristics are shown in fig 3.13.

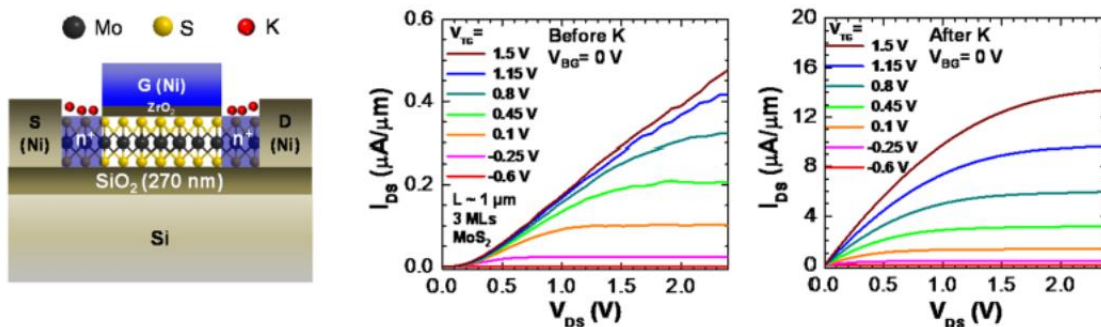


**Fig 3.13: Device structure and electrical characteristics of MoS<sub>2</sub> transistor which has K doping at the contacts. Reproduced from Ref. 157.**

Apart from devices on SL MoS<sub>2</sub>, interesting characteristics can also be obtained from multilayer MoS<sub>2</sub> transistors. Kim et al fabricated devices on multilayer MoS<sub>2</sub> and obtained mobilities which exceeded the present semiconductor materials used for large area thin film transistors. Apart from this high mobility, multilayer MoS<sub>2</sub> has additional attractive features such as high current modulation, low sub-threshold slope, and the ease of growing multilayer MoS<sub>2</sub> over large area. These properties make it a viable candidate for thin film transistors implementation<sup>158</sup>. Device schematic and characteristics on multilayer MoS<sub>2</sub> are shown in fig 3.14 below.

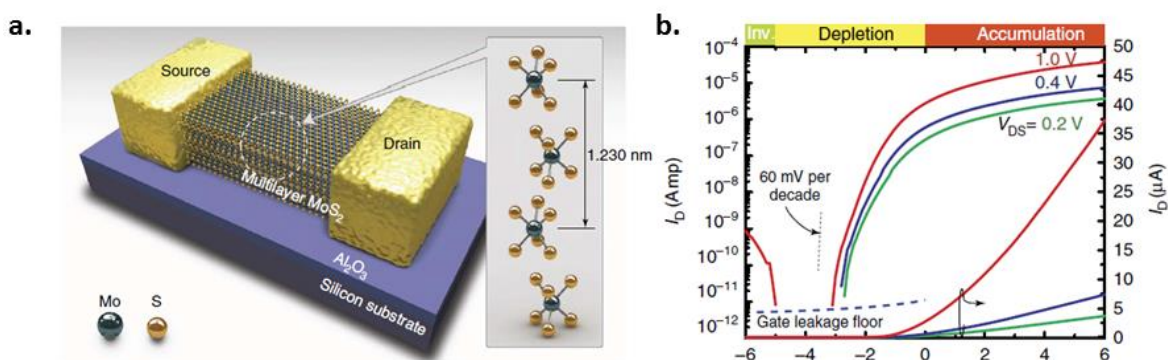


**Fig 3.14: a) Schematic of multilayer MoS<sub>2</sub> device. b) Transfer characteristic showing the inverse, depletion and accumulation region of operations of the device. Reproduced from Ref. 158.**

### 3.6 Chapter summary

This chapter focused on an important member of the TMD family, MoS<sub>2</sub>. A brief summary of its properties and applications has been presented. Structure of MoS<sub>2</sub> has been discussed in detail with differences in the naturally occurring 2H phase and the metastable 1T phase. Top down and bottom up synthesis procedures have also been discussed. Optical (Raman and Photoluminescence) and electrical characterization of MoS<sub>2</sub> has also been described in detail. This chapter will conclude with description of the problem statement and a strategic solution will be discussed in the next section.

## **Problem Statement and Solution Strategy**

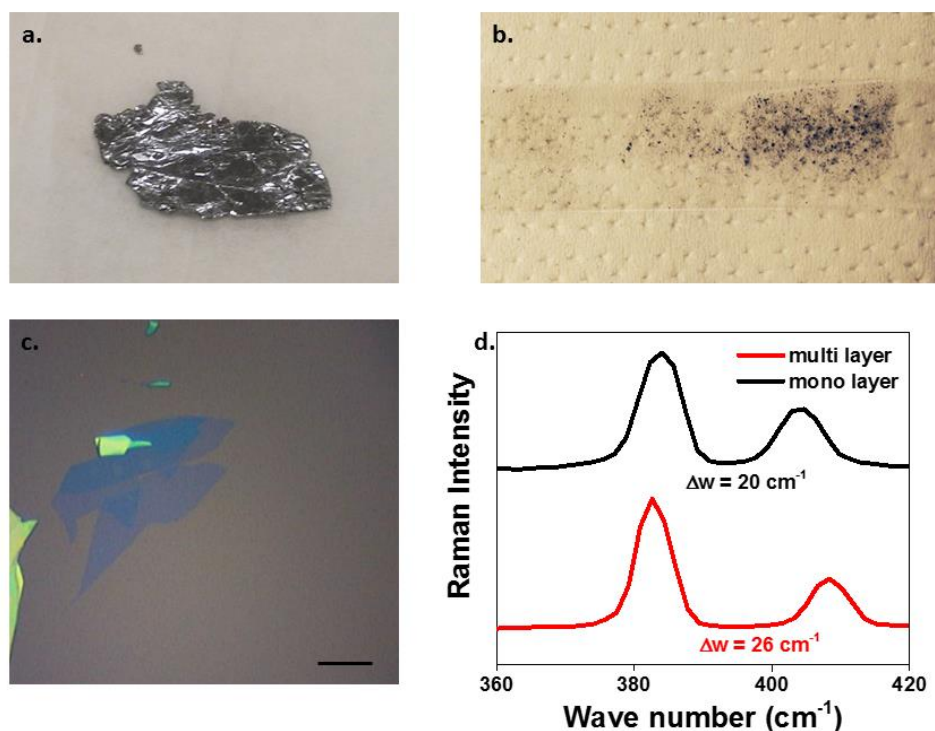
One common problem encountered by every researcher while making devices with MoS<sub>2</sub> is the high contact resistance between the metal and semiconductor<sup>155,159,160</sup>. This arises due to the Schottky barrier that is formed between metal and MoS<sub>2</sub><sup>155,161-163</sup>. Usually this high contact resistance is reduced by annealing the sample at high temperatures (200 °C to 400 °C) under inert conditions<sup>164-166</sup>, but this is not an option for flexible electronics. Another attempted method was the use of different metals to make contacts with MoS<sub>2</sub> that enabled a reduction in the Schottky barrier<sup>153,167-169</sup> but there was still a considerable amount of contact resistance present after this attempt. The method of doping the contact regions of MoS<sub>2</sub> seems to be valid, but there is no efficient method for control in doping which makes these methods volatile<sup>155</sup>. Due to the high contact resistance inherent in the system, we were unable to explore the excellent intrinsic properties of MoS<sub>2</sub>.

In order to solve this problem our strategy was to use the 1T-2H interface of MoS<sub>2</sub> to our advantage. Phase transformation can be performed locally to develop a 1T-2H hybrid structure<sup>13,14</sup>. Since 1T MoS<sub>2</sub> is metallic in nature, the contact resistance and Schottky barrier height would be considerably lower between 1T MoS<sub>2</sub> and metal when compared to 2H MoS<sub>2</sub> and metal. We plan to make a device using a flake which has 1T-2H-1T hybrid structure. Upon deposition of metal onto the 1T region we would have a device which would have low contact resistance due to the metal-1T interface and simultaneously have high gate modulation due to the 2H MoS<sub>2</sub> present as the channel region. This molecular electronic device would be suitable for future electronics as it would combine the essential features of flexibility, low-standby-power consumption, and efficient gate electrostatics with reduced short channel effects.

## Chapter 4

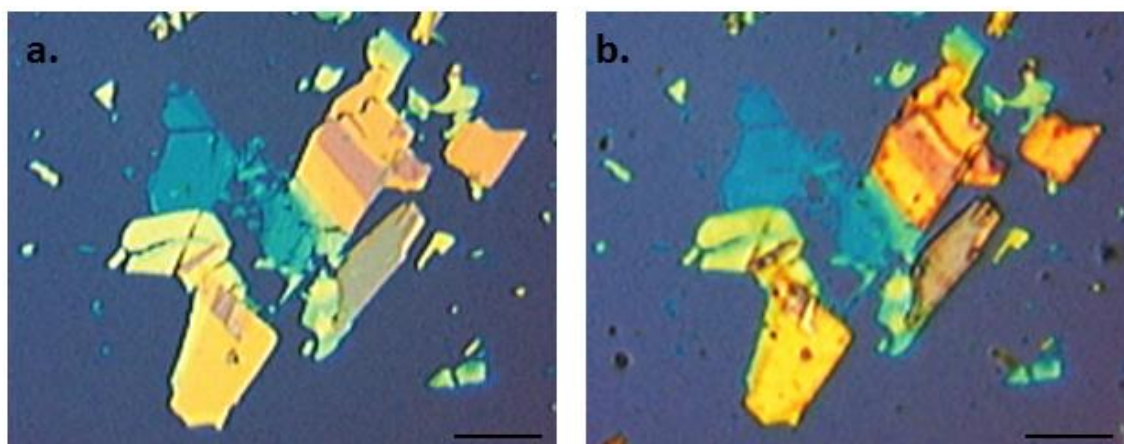
### 4.1 Phase Engineering in MoS<sub>2</sub>

Figure 4.1 shows the single crystal purchased from SPI supplies, a length of scotch tape which has flakes exfoliated from the single crystal, and the optical microscope images of single layered and few layered MoS<sub>2</sub>. Flakes were deposited on silicon substrates which are capped with 300 nm of silicon dioxide. This thickness of the oxide layer is chosen because it gives the perfect optical contrast to identify single layer of MoS<sub>2</sub> with ease. The flake thickness was confirmed through the use of optical microscopy and Raman spectroscopy, with which we could observe the frequency difference between the two strong peaks, the in-plane E<sub>12g</sub> and out-of-plane A<sub>1g</sub> peaks, which would reduce as the flake becomes thinner. This can be seen in fig 4.1c and d.



**Fig 4.1:** a) Single crystal MoS<sub>2</sub> purchased from SPI supplies (length = 5 cm) b) Image of scotch tape with MoS<sub>2</sub> flakes c) Optical microscope images of single layer and multilayer MoS<sub>2</sub> flakes (Scale bar = 5 μm) d) Raman spectra of monolayer and multilayer MoS<sub>2</sub>

In order to convert the MoS<sub>2</sub> phases, samples were immersed in 1.6M n-butyl lithium purchased from Sigma-Aldrich for increasing amounts of time in intervals of 12 hours. Since n-butyl lithium is not an air-stable material, all experiments were performed in a glove box filled with Argon gas. Upon the completion of time, sample was cleaned thoroughly with hexane and was then removed from the glove box. In order to remove lithium ions intercalated into MoS<sub>2</sub>, the sample was cleaned with de-ionized water thoroughly and then cleaned with acetone and IPA to keep it free from solvent residues. Figure 4.2 shows the optical images of flakes after exfoliation and the same flakes after lithium intercalation induced phase change. Note that there is no physical damage to the flakes due to lithium exposure.



**Fig 4.2:** Optical microscope images of mechanically exfoliated MoS<sub>2</sub> flakes a) as exfoliated b) after lithium intercalation based phase transformation. Scale bar = 5  $\mu$ m

## 4.2 Characterizing 1T and 2H MoS<sub>2</sub>

**4.2.1 Raman Spectroscopy:** In order to make sure the phase conversion has been done, Raman spectroscopy was performed on the flakes after every 12 hours to see the difference in spectra for as is and phase transformed flakes. Raman was performed using an InVia Raman microscope (Renishaw) at an excitation wavelength of 514 nm at room

temperature in air. As exfoliated MoS<sub>2</sub> flakes exhibited the in plane E<sub>2g</sub><sup>1</sup> and out of plane A<sub>1g</sub> peaks. After phase transformation these two peaks were reduced in intensity and there was the emergence of three new peaks at 156 cm<sup>-1</sup>, 226 cm<sup>-1</sup> and 330 cm<sup>-1</sup>. These three peaks are J<sub>1</sub>, J<sub>2</sub>, and J<sub>3</sub> and represent the 1T phase of MoS<sub>2</sub>. Fig 4.3 also clearly shows that the two MoS<sub>2</sub> peaks which represent the 2H phase gradually reduce in intensity while the three MoS<sub>2</sub> peaks which represent the 1T phase continue to rise in intensity. To see the peaks clearly, fig 4.3b shows the Raman spectra of pure 2H MoS<sub>2</sub> flake and with the spectra of a MoS<sub>2</sub> flake which has the highest content of 1T phase overlaid upon it. All the peaks are represented with bands for clear visibility.

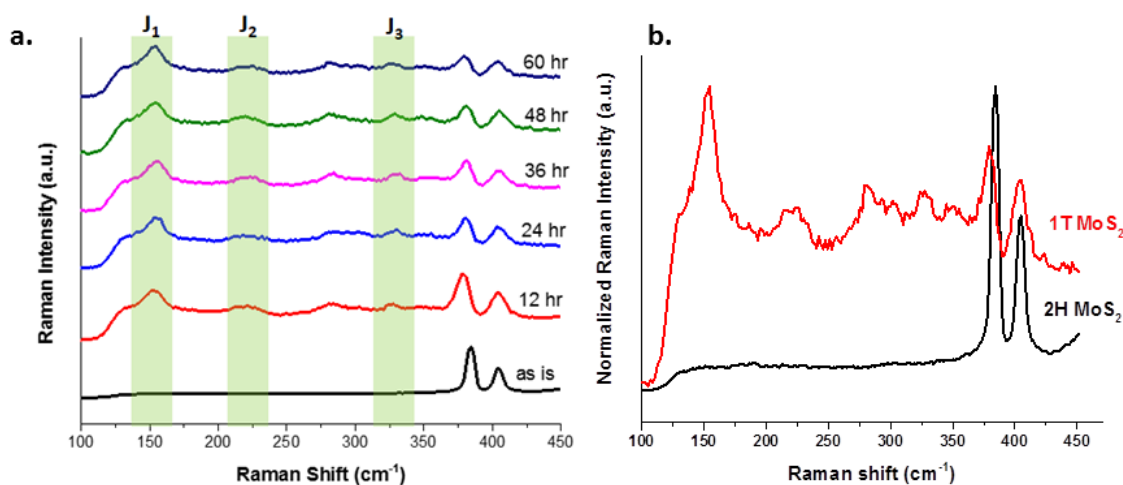


**Fig 4.3: a) Raman spectra of MoS<sub>2</sub> flake which underwent lithium intercalation for increasing amounts of time b) Raman spectra of 1T and 2H MoS<sub>2</sub> flake**

**4.2.2 X-ray Photoelectron Spectroscopy:** Though Raman spectroscopy enables us to identify the 2H phases and 1T phases of MoS<sub>2</sub>, it does not help in computing the amount of each phase in a flake. As it was shown in a few earlier reports that 1T and 2H phase co-exist<sup>13,14,170-172</sup>, it is quite important to have an idea of the amount of each phase present in a sample. In order to identify the amounts, we can use X-ray photoelectron spectroscopy (XPS) to aid us as it specifies both the elemental composition of the MoS<sub>2</sub> sample and the

binding energy of each element. In the case of 2H MoS<sub>2</sub> flakes, the Mo 3d scan peaks appear at 229.5 and 232 eV<sup>173</sup>. However in the case of 1T MoS<sub>2</sub> flakes, since the flake is metallic rather than semiconducting like 2H MoS<sub>2</sub>, there would be a change in the Fermi level. This change can be detected by XPS and so the Mo 3d peaks get shifted to lower binding energies by approximately 1 eV in the case of metallic MoS<sub>2</sub>. Since the partially phase-transformed MoS<sub>2</sub> will have co-existing 2H and 1T phases, XPS gives a doublet peak for the Mo 3d scan; by de-convoluting this doublet peak we can compute the amount of each phase present in the MoS<sub>2</sub> flake. Fig. 4.4a shows that as the time of lithiation (lithium intercalation) increases the Mo coming from 1T MoS<sub>2</sub> increases and the Mo from 2H MoS<sub>2</sub> decreases. It was found that after a lithiation time of 60 hours, the 1T content is very high at over 80%. Fig. 4.4b shows just the Mo 3d scan of as made MoS<sub>2</sub> and another MoS<sub>2</sub> flake which has the highest content of 1T MoS<sub>2</sub>.

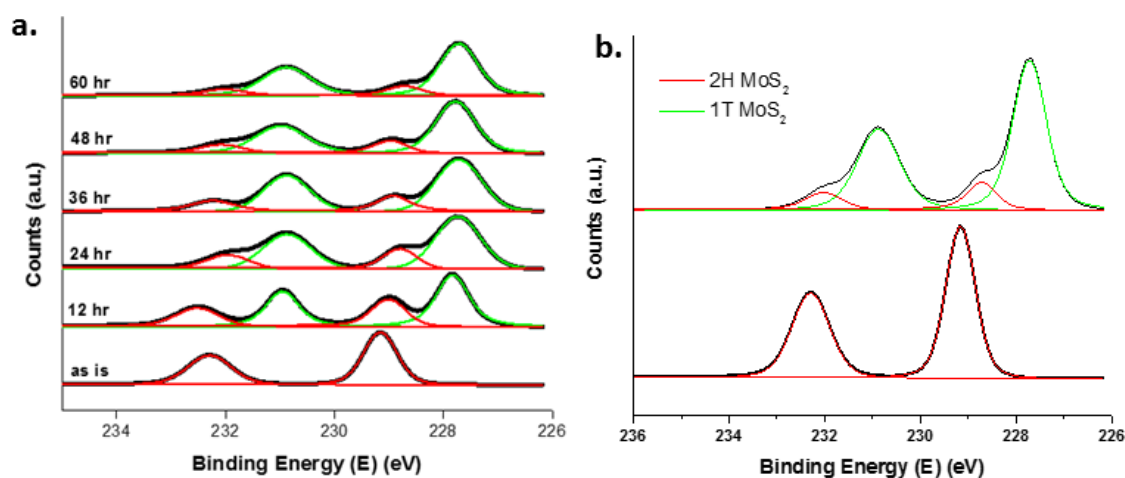


**Fig 4.4:** a) XPS spectra of MoS<sub>2</sub> flake which underwent lithium intercalation for increasing amounts of time b) XPS spectra of as exfoliated MoS<sub>2</sub> flake and after it got phase transformed to 1T.

### 4.2.3 Fluorescence Imaging

Since single layer MoS<sub>2</sub> is a direct band gap semiconductor, it has a very bright fluorescence response when illuminated with a monochromatic light above its band gap value. Since the band gap of monolayer MoS<sub>2</sub> is 1.9 eV, we used a laser with a 488 nm wavelength to excite the samples and collected the fluorescence image coming from single layer MoS<sub>2</sub> flakes. We used CVD MoS<sub>2</sub> flakes for this purpose and observed that the whole triangular flake shines very bright when excited with the laser. Fig 4.5a shows images of single layer CVD MoS<sub>2</sub> flakes glowing bright under laser excitation.

Now if we take into account the property of 1T MoS<sub>2</sub> flakes, which are metallic in nature, they should have no fluorescence. This is evident in images in fig. 4.5b.

Since the CVD flakes are large, more than 10 micron in size, I went ahead and started patterning the flakes with half 1T and half 2H phases in single flake. This was done with the aid of e-beam lithography where PMMA acts as a resist. First I covered the whole flake with PMMA and then removed it in the areas on the flake where I wanted to convert to 1T phase. I then immersed the sample in n-butyl lithium and followed the same process for conversion to 1T phase as mentioned earlier. The part of the flake which is covered with PMMA will not be converted since they are inaccessible for lithium ions. Upon the completion of the desired time of lithiation, the sample was cleaned with hexane, followed by water, and then the PMMA was removed by dissolving it in acetone. The resulting flakes would have patterned 1T phase on a flake where everything else would be in 2H phase. Upon looking at this image under the fluorescence microscope, only the 2H portion of the flake would fluoresce and the 1T portion would appear dark as is evident from images in fig. 4.5c and fig. 4.5d.

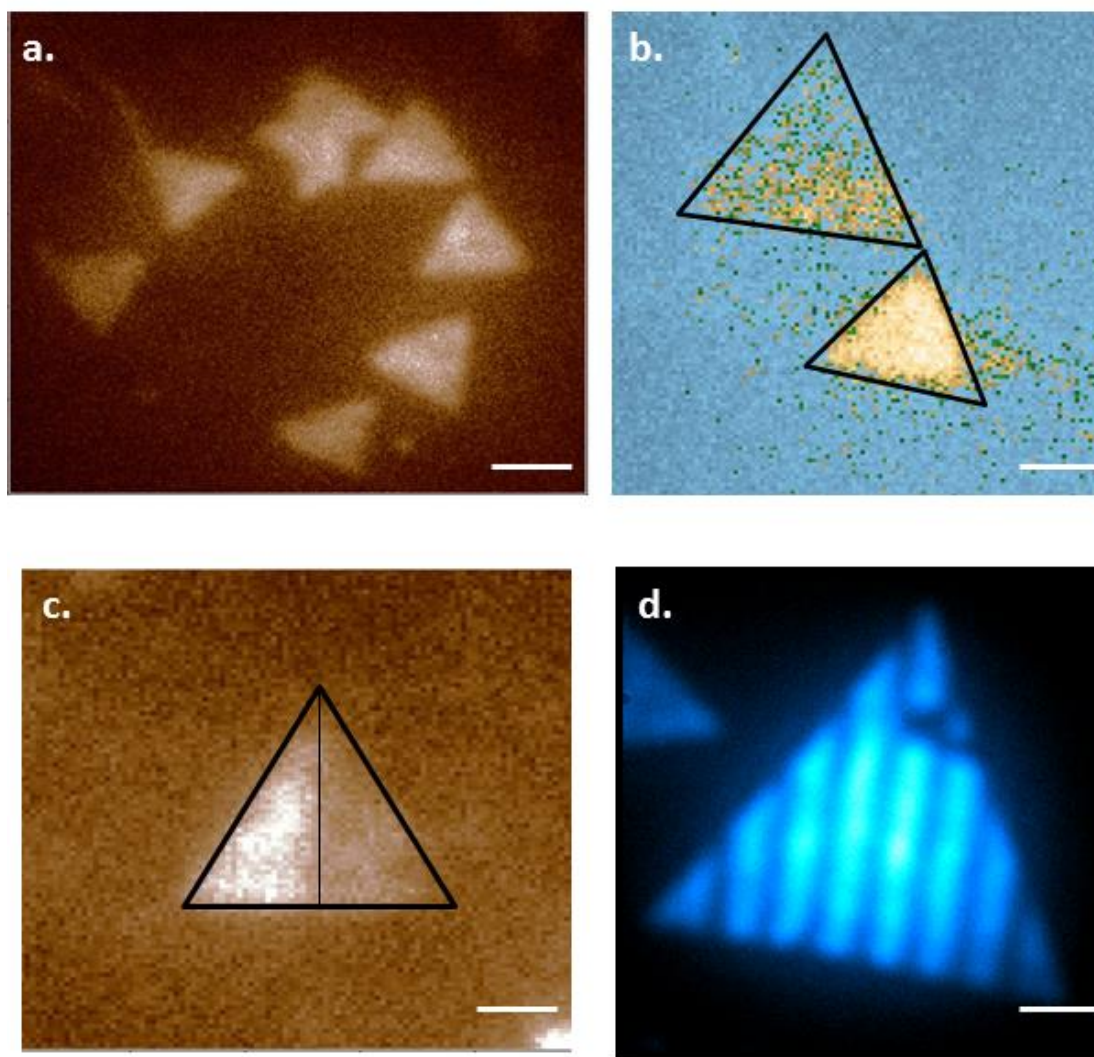


**Fig 4.5:** Fluorescence images of a) as grown CVD MoS<sub>2</sub> flakes b) one metallic and one semi-conducting MoS<sub>2</sub> flake c) a flake which has half semi-conducting and half metallic phase d) a flake which has narrow regions of 1T phase MoS<sub>2</sub> on a 2H phase flake. All scale bars are 5 μm. Average length of the base of triangle is 12 μm.

#### 4.2.4 Scanning Electron Microscopy

I've also used scanning electron microscope to distinguish between 1T phase and 2H phase of flakes since the metallic portion would have a difference contrast in the image than the 2H phase owing to the difference in conductivity. Fig 4.6 shows the patterned 1T and 2H phases of the flakes. The 1T part of the flake appears darker than the 2H part of the flake.

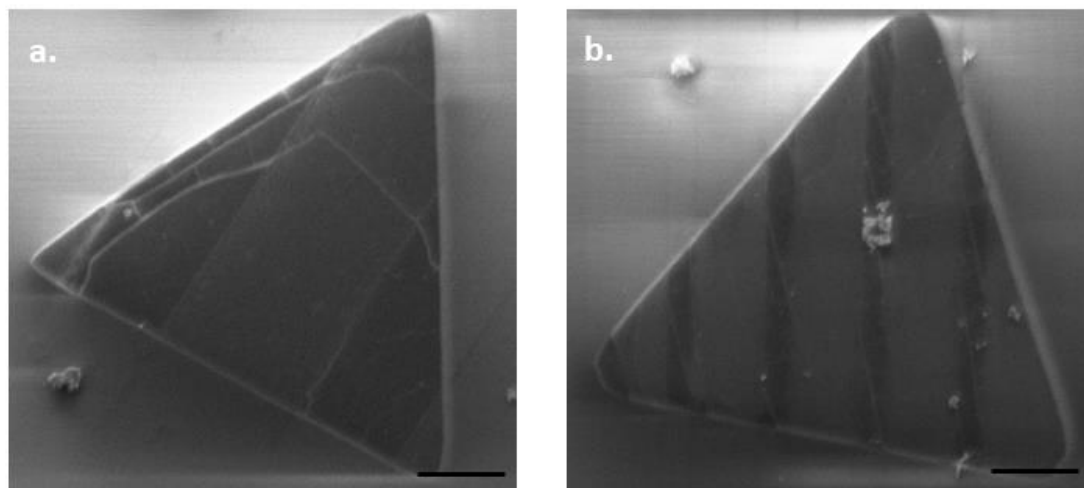


**Fig 4.6: SEM Images of patterned 1T phase on 2H flakes. The 1T phase appears darker due to higher conductivity compared to the 2H phase. Scale bar = 2  $\mu$ m.**

#### **4.2.5 Transmission Electron Spectroscopy (TEM)**

We have also performed high resolution transmission electron microscopy on our flakes to show the coexistence of 1T and 2H phases MoS<sub>2</sub> on a flake. These results are shown in Fig 4.7 which shows the coherent atomic structures of both the phases and the atomic sharp interface that exists among them. These results are encouraging to realize devices which have these coexisting structures.

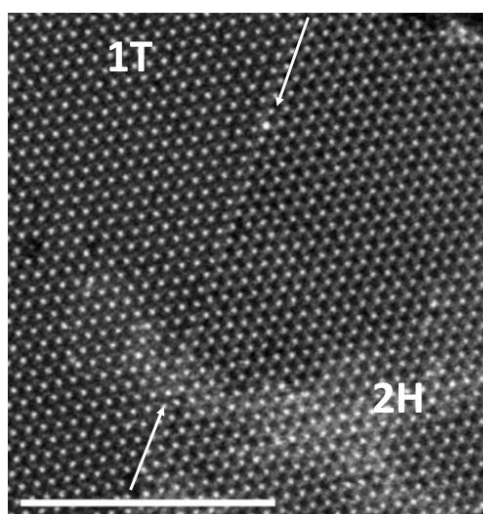


**Fig 4.7: High resolution transmission electron microscope image of the 1T phase and 2H phase MoS<sub>2</sub> boundary depicting the atomically thin interface between them.**

### 4.3 Chapter summary

This chapter described the process of phase transformation of MoS<sub>2</sub> with lithium intercalation in detail. Structural characterization of the two phases on MoS<sub>2</sub> is described in the next section where Raman spectra of 2H and 1T MoS<sub>2</sub> is described. This was followed by compositional characterization of MoS<sub>2</sub> with XPS which helped in identifying and quantifying the 1T phase and 2H phase in a given flake of MoS<sub>2</sub>. Patterning of 1T phase on 2H MoS<sub>2</sub> flake is demonstrated and was characterized by SEM and Fluorescence imaging. The atomic sharp interface of the 1T and 2H phases was shown by high resolution transmission electron microscope imaging. Further chapters would discuss the application of these concepts in making high performance MoS<sub>2</sub> devices.

## Chapter 5

### Devices on Mechanically exfoliated MoS<sub>2</sub>

**5.1 Device Fabrication:** In order to get the best working MoS<sub>2</sub> devices, an essential requirement that needs to be fulfilled is to obtain a good quality flake upon its exfoliation from the crystal and maintain its quality throughout the process of making a device on it. For this purpose, high quality Nitto-denko tape is chosen which does not leave any residue while exfoliating the crystal. Silicon substrates with 100nm or 300nm oxide layer were diced into 1cm x 1cm squares and were first cleaned in boiling acetone and then rinsed with isopropanol. This was followed by ozone plasma treatment for the substrates which helps in proper adhesion of MoS<sub>2</sub> monolayers to the substrates. A small piece of MoS<sub>2</sub> crystal is attached onto the tape and then slowly lifted off at the smallest angle possible. The remnant of the flake on the tape is exfoliated numerous times until a pale green color of the flakes is left on the tape. Si substrates are placed on these regions and uniform pressure is applied for a couple of minutes to transfer the flakes from the tape to the substrates. The tape is removed slowly at a small angle in order to avoid cracking of the flakes. This process ensures flakes of above 10 $\mu$ m in size to be obtained. The substrates are soaked in acetone for 10 minutes so as to dissolve any tape residue present on the flakes and followed by an isopropanol rinse. Fig. 5.1 shows optical microscope images of some typical MoS<sub>2</sub> flakes obtained from mechanical exfoliation.

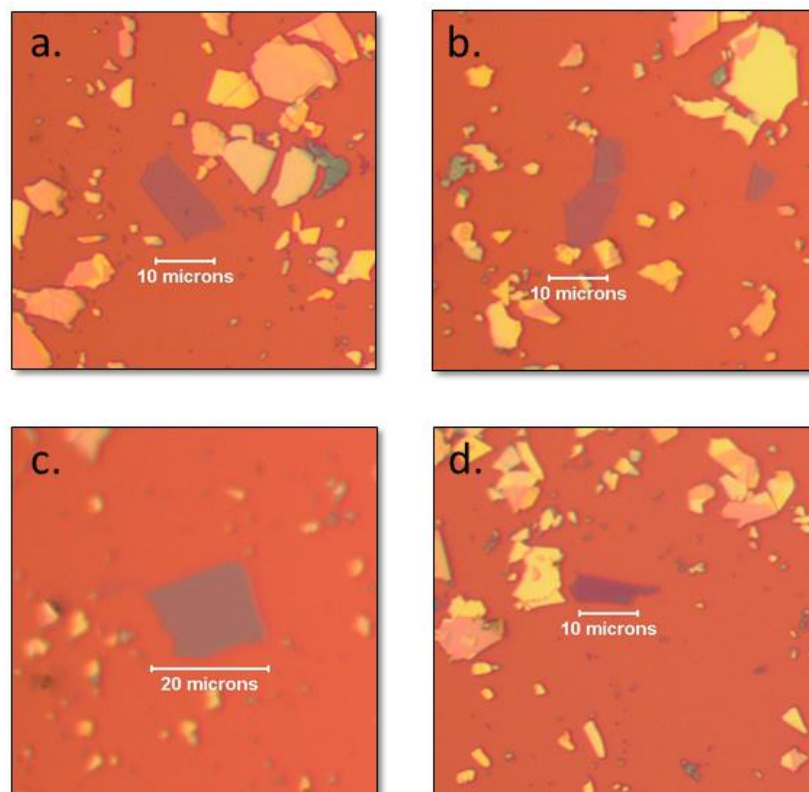


**Fig 5.1: Optical microscope images of mechanically exfoliated MoS<sub>2</sub> flakes on 300nm SiO<sub>2</sub> substrates.**

Accurate position of the flakes on the substrates is determined with their deposition on pre-patterned substrates. Optical microscope images are used to make the design files to pattern electrodes on the flake using appropriate software such as SolidWorks or AutoCad.

After cleaning the samples, they are spin coated with a positive e-beam resist, PMMA. Two different molecular weight PMMA is used, the bottom layer is a lower molecular weight PMMA which can be easily dissolved in acetone and the top layer is a higher molecular weight PMMA which allows accurate patterning of the electrodes on the flake. These both PMMA layers are coated one after the other at a speed of 3000 RPM for 60 seconds followed by a baking time of 90 seconds at 180 °C. This process gives a total thickness of ~500nm of PMMA which is suitable for perfect development of exposed PMMA after e-beam lithography.

For e-beam lithography, a current of 40pA was used for exposure at a dose rate of 400  $\mu\text{C}/\text{cm}^2$  which have been optimized with numerous experiments. The development was done with a solution of methyl isobutene ketone and isopropanol in 1:3 ratio for 90 seconds followed by an isopropanol rinse. This was followed by metallization where e-beam evaporation was employed. An initial deposition of 5nm titanium is done at a rate of 0.1nm/second which is followed by 50nm of gold at a rate of 0.3nm/second. For lift-off, the samples are immersed in acetone until the metal starts getting peeled off. After all the metal is removed, the samples are cleaned with isopropanol. Typical device images are shown in fig 5.2.

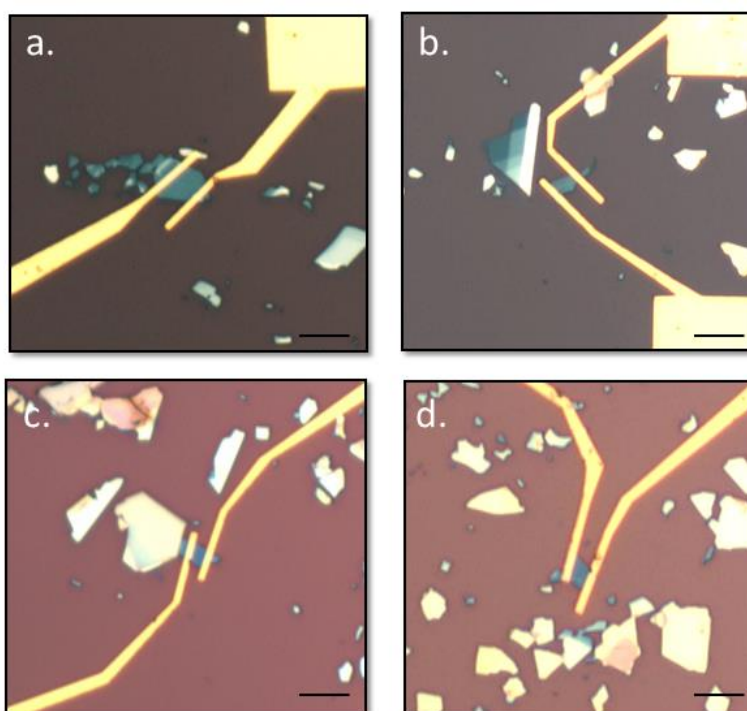


**Fig 5.2: Optical microscope images of devices made on mechanically exfoliated MoS<sub>2</sub> on 100nm (a,b) and 300nm (c,d) SiO<sub>2</sub> substrates. Scale bar = 5  $\mu\text{m}$**

**5.2 Electrical Measurements:** Electrical characteristics of these devices were made where the two electrodes on the flake were used as the source and drain electrodes and the bottom silicon substrate was used as the global gate. This was contacted from the top by scratching off the oxide layer and using silver paste as the electrode. Devices made with the above mentioned process worked decently exhibiting reasonable currents and good field modulation. Typical transfer and output characteristics of such devices are shown in fig. 5.3 and the average figures of merit of over 10 devices are mentioned in table 5.1.

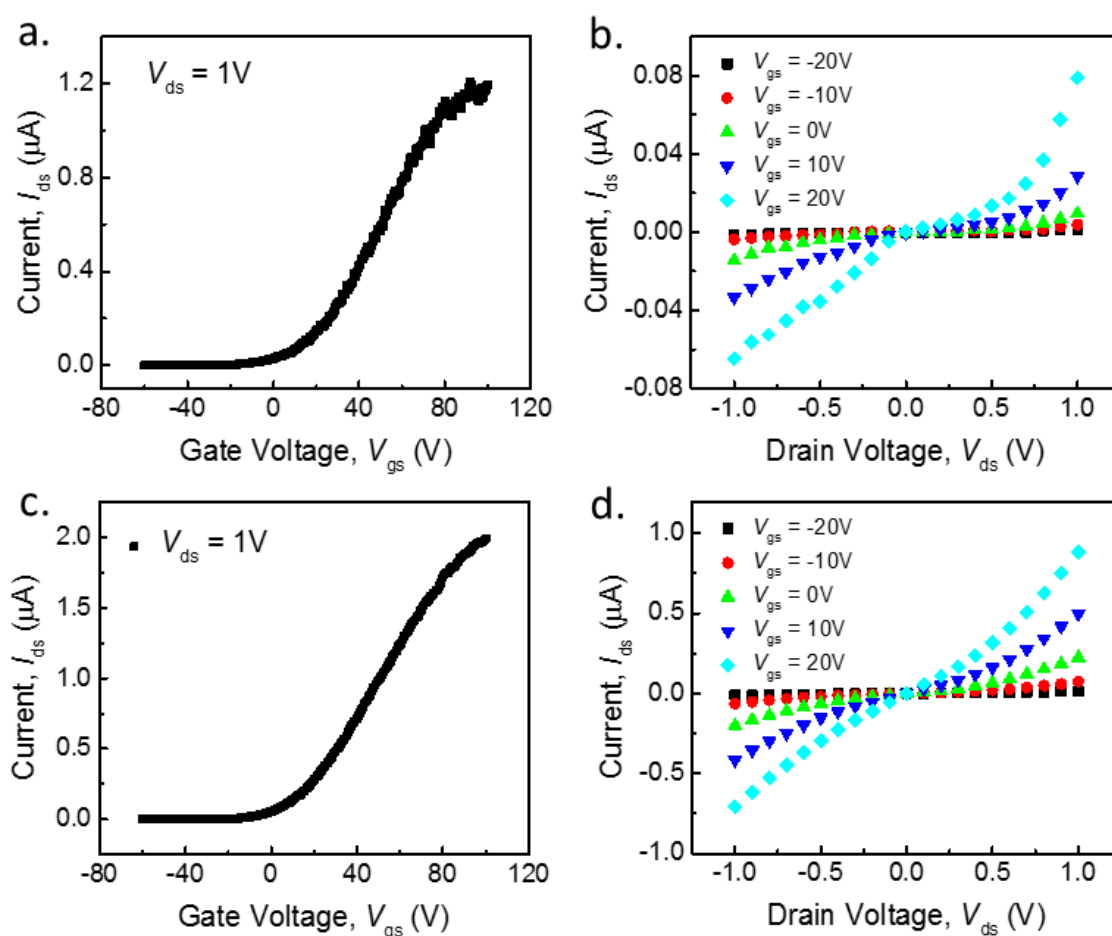


**Fig 5.3:** Transfer (a, c) and output (b, d) characteristics of MoS<sub>2</sub> field effect transistors with Au-Ti electrodes.

I extracted the mobility values from the transfer characteristics of the devices and the average mobility for around 10 devices came out to be 5 cm<sup>2</sup>/Vs. The mobility was extracted by using the drain-source current equation in the linear region of operation of a MOSFET.

$$I_{DS} = \mu C_{ox} \frac{W}{L} ((V_{GS} - V_T)V_{DS} - \frac{V_{DS}^2}{2})$$

By taking the first order derivative of this equation with respect to  $V_{DS}$ , we can extract the formula to calculate the mobility which comes out as

$$\mu = \frac{Lg_m}{WC_GV_{DS}} \text{ where } g_m = \frac{\partial I_{DS}}{\partial V_{GS}}$$

**Table 5.1: Device properties of MoS<sub>2</sub> field effect transistors with Au-Ti contacts**

Property	Value
ON Current (μA/μm)	4.8
Transconductance (μS/μm)	0.3
Mobility (cm <sup>2</sup> /Vs)	6.9
ON/OFF ratio	10 <sup>6</sup>

Though these devices looked good in terms of their performances they are much underpar when compared to the devices published in literature. Upon careful analysis, it was found that though titanium acts as an excellent adhesion layer, it tends to react with the sulfur present in MoS<sub>2</sub> causing a reduction in the device properties. In order to deal with this issue, two separate lithography processes was employed to fabricate devices.

In the first lithography process, windows were opened on the flake and only gold deposition was performed at a very slow rate of 0.5 Å/s. After liftoff, PMMA was again spinned on

the sample using the same recipe as afore mentioned and a second lithography step was performed to open the pads connecting the electrodes. This time a titanium layer of 5nm was deposited at 0.1nm/s followed by 50nm gold deposition at 0.3nm/s. Lift off was performed very carefully since adhesion of gold is not good on the MoS<sub>2</sub> flake. Fig 5.4 shows the optical microscope image at each of the major steps in this device fabrication procedure.

Devices made with this procedure exhibited a much superior performance compared to devices with had Ti contacting MoS<sub>2</sub>. They were in par with the device results published in literature. Fig. 5.5 shows some device images and the transfer and output characteristics of such devices and table 5.2 shows the properties which are averaged of over 10 devices.

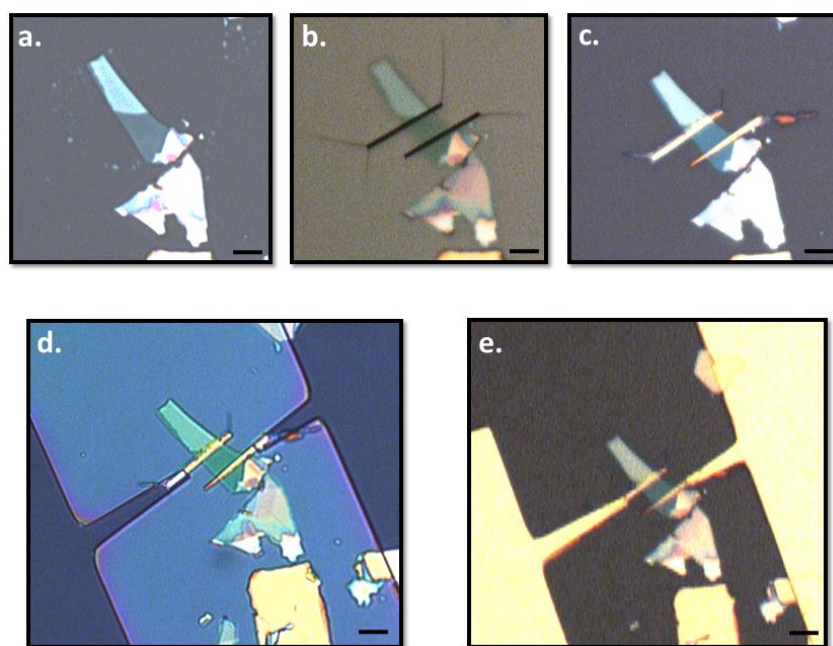


**Figure 5.4: Optical microscope images depicting each step of MoS<sub>2</sub> device fabrication procedure a) Picture of a 3-4 nm MoS<sub>2</sub> flake b) Windows opened on the flake, rest of the sample covered with PMMA c) Flake with 50nm of gold electrodes d) Pads opened connecting the two gold electrodes e) Pads of 10nm titanium and 50nm gold connecting the gold electrodes. All scale bars = 5 μm.**

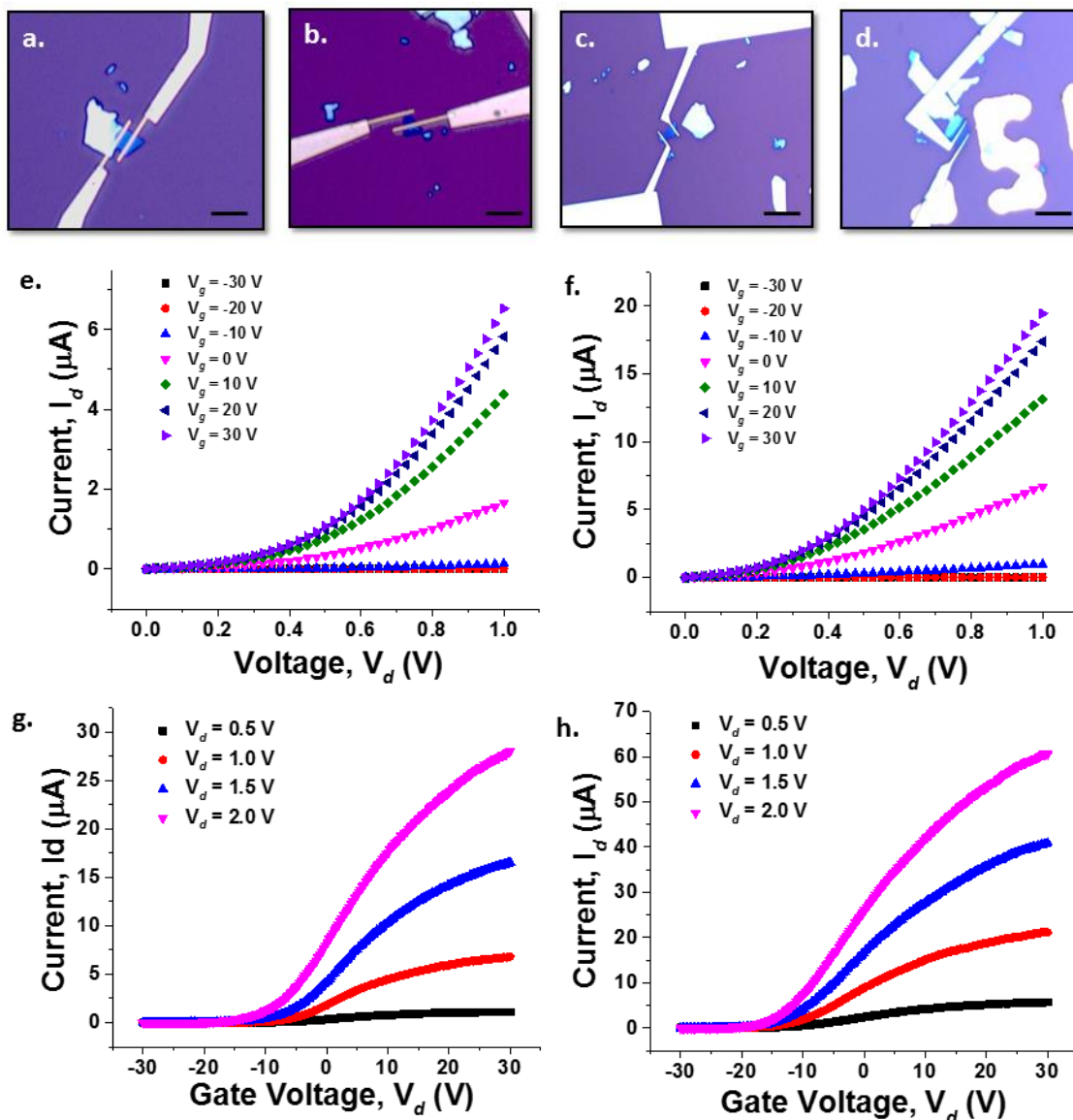


Fig 5.5: a-d) Devices on mechanical exfoliated MoS<sub>2</sub> flakes. All scale bars = 5 μm. e, f) Output characteristics showing the presence of schottky barrier between gold and MoS<sub>2</sub>. g, h) Transfer characteristics of the devices which show a good turn on feature and good carrier mobility.

Table 5.2: Device properties of MoS<sub>2</sub> field effect transistors with Au contacts

Property	Value
ON Current (μA/μm)	30
Transconductance (μS/μm)	1.4
Mobility (cm <sup>2</sup> /Vs)	19
ON/OFF ratio	10 <sup>7</sup>

Properties of these devices are comparable to the values reported in literature for mechanically exfoliated devices with gold contacts<sup>174-176</sup>. The skew in the output curves represents the schottky barrier that exists between MoS<sub>2</sub> and gold. Elimination or reduction of this barrier would help in obtaining ohmic contacts and hence better performance from devices. This has been done in the past by annealing the devices under inert conditions for a long time (overnight or longer) and in other cases by doping MoS<sub>2</sub> at the contacts. We have chosen to solve this issue by using phase transformed MoS<sub>2</sub> as the electrodes.

### **5.3 Chapter Summary**

This chapter described the process of mechanical exfoliation to obtain flakes of 1 to 3 layers of MoS<sub>2</sub>. Device fabrication procedure using e-beam lithography was described in detail. Electrical characterization of preliminary devices with Au-Ti contacts have been discussed and the reasons for low performance of these devices have been discussed. Au contacts have been used instead of high performance devices have been obtained which compare with the state of the art MoS<sub>2</sub> devices reported in literature. However, the output characteristics are non-linear which represents the high schottky barrier that exists between gold and MoS<sub>2</sub>. The next chapter discusses the use of 1T phase contacts to reduce this barrier and hence obtain devices of enhanced performances. Chapter 6 and 7 is the description of my work published in Nature Materials<sup>177</sup>. All the details contained in these chapters are compiled into the paper.

## Chapter 6

### Devices with 1T phase MoS<sub>2</sub>

**6.1 1T Phase Conversion:** In order to ensure the metallic nature of 1T phase MoS<sub>2</sub>, devices were fabricated on MoS<sub>2</sub> flakes which were converted to 1T phase through lithium intercalation. For this purpose, exfoliated flakes on SiO<sub>2</sub> substrates were immersed in 1.6M n-butyl lithium for 2 days. Since n-butyl lithium is an air sensitive chemical (Reacts vigorously with moisture and oxygen), all the experiments were performed in Argon filled glove box at room temperature and atmospheric pressure. Upon lithium intercalation, the samples were cleaned with hexane in the glove box to remove excess lithium. Then they were rinsed with distilled water so that all the lithium present in MoS<sub>2</sub> reacts with the water and gets removed so that only pure 1T phase MoS<sub>2</sub> remains eventually.

***Electron Energy Loss Spectroscopy:*** In order to confirm that all the lithium is removed we performed Electron Energy Loss Spectroscopy (EELS), a very common surface analysis technique used to detect elements present in the material. The STEM analysis of our material identified the 1T phase (shown earlier) and when same material was analyzed by EELS results (Fig 6.1), there was no signature of lithium (Li edge is expected at ~60eV) present.

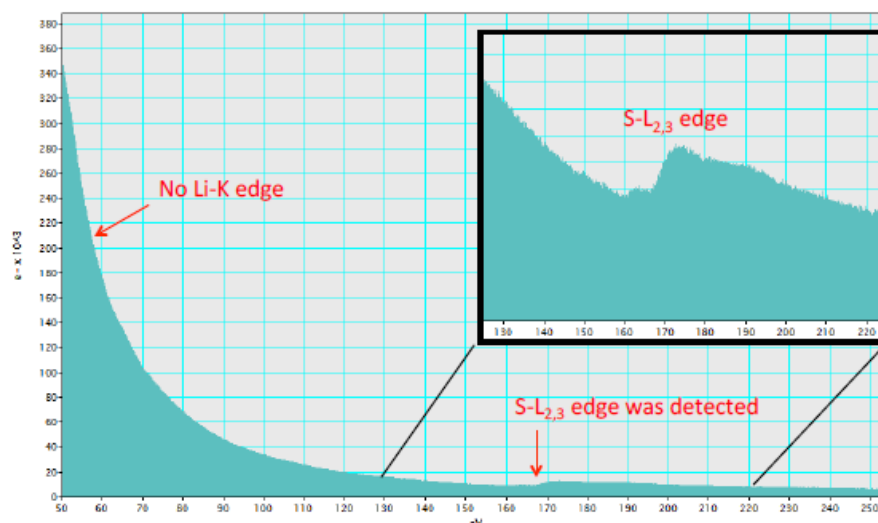


**Fig 6.1:** EELS spectrum of MoS<sub>2</sub> flake treated with butyl lithium and thoroughly washed with hexane and water.

**Nuclear Reaction Analysis:** Since EELS is a surface technique, we further performed Nuclear reaction analysis (NRA) which is a more robust and efficient technique for elemental analysis of a material. We performed NRA on two different samples, one which was washed with hexane but not with water and another sample which was washed with hexane and then with water. The former sample will have lithium present in it in the form of intercalated element in MoS<sub>2</sub> whereas the latter element will have a very minimum amount if at all present. NRA was performed using  ${}^7\text{Li}(p,\alpha){}^4\text{He}$  nuclear reaction with a 2000 keV proton ion beam. Lithiated MoS<sub>2</sub> without water rinse had  $\sim 1$  Li per MoS<sub>2</sub> giving an approximate stoichiometry of LiMoS<sub>2</sub>. The sample which was washed with water had Li in negligible amounts consistent with the result obtained through EELS. Fig 6.2 shows the results of NRA.

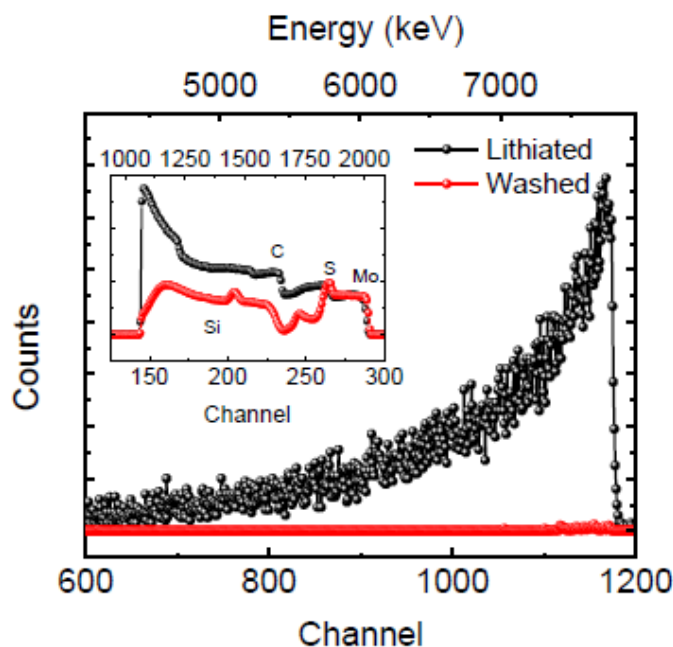


**Fig 6.2: NRA on MoS<sub>2</sub> treated with butyl lithium and thoroughly washed with hexane and water.**

**6.2 1T MoS<sub>2</sub> Device results:** Devices were made on 1T MoS<sub>2</sub> flakes using the procedure mentioned earlier by e-beam lithography. Since 1T MoS<sub>2</sub> is metallic in nature, the metal contacting MoS<sub>2</sub> did not have any significant effect on the device properties hence I followed the regular device making procedure of one lithography step and one metallization step. Fig 6.3 shows the field effect device characteristics of 1T phase MoS<sub>2</sub>. The linear output characteristics depict the presence of ohmic contact between the metal and 1T MoS<sub>2</sub>. Fig 6.3b shows the transfer characteristics of the devices which show no field dependent modulation even though the gate is scanned from -100V to 100V, this represents the high carrier concentration in 1T phase MoS<sub>2</sub> and hence of lack of Fermi level tuning. This is a very significant result in realizing high performance devices with MoS<sub>2</sub> since this 1T phase MoS<sub>2</sub> can be used as a contact to 2H phase MoS<sub>2</sub> which would not have a barrier and henceforth reducing the contact resistance by a significant amount.

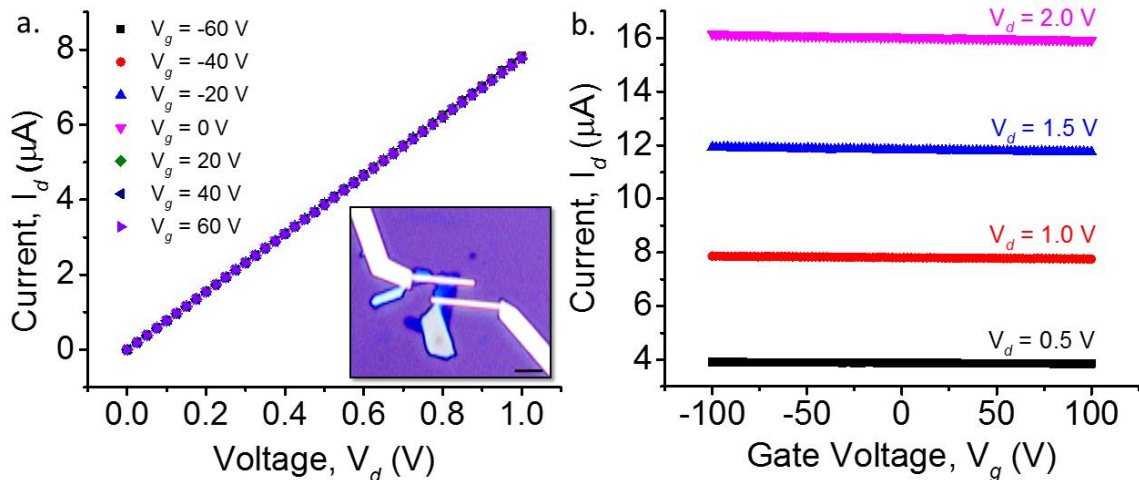


**Fig 6.3: Output (a) and Transfer characteristics (b) of device on 1T phase MoS<sub>2</sub>. Scale bar = 5  $\mu\text{m}$ .**

**Four probe measurement:** The lack of field effect in 1T MoS<sub>2</sub> devices reflects that there would be very low contact resistance between metal and 1T MoS<sub>2</sub>. In order to realize this I made a four terminal device on a 1T MoS<sub>2</sub> flake and measured the 2 terminal IV characteristics and the 4 terminal 1V characteristics. In the four terminal 1V measurement, the voltage is applied in the external terminals and the current is measured and plotted as function of the voltage measured in the two internal terminals; this IV measurement separated the current and the voltage leads and hence is independent of lead and contact resistance. From the results, it was noted that there was no significant difference between the 2 terminal and 4 terminal measurement (Fig 6.4) and hence proved the fact again that the contact resistance is very low between metal and 1T MoS<sub>2</sub>.

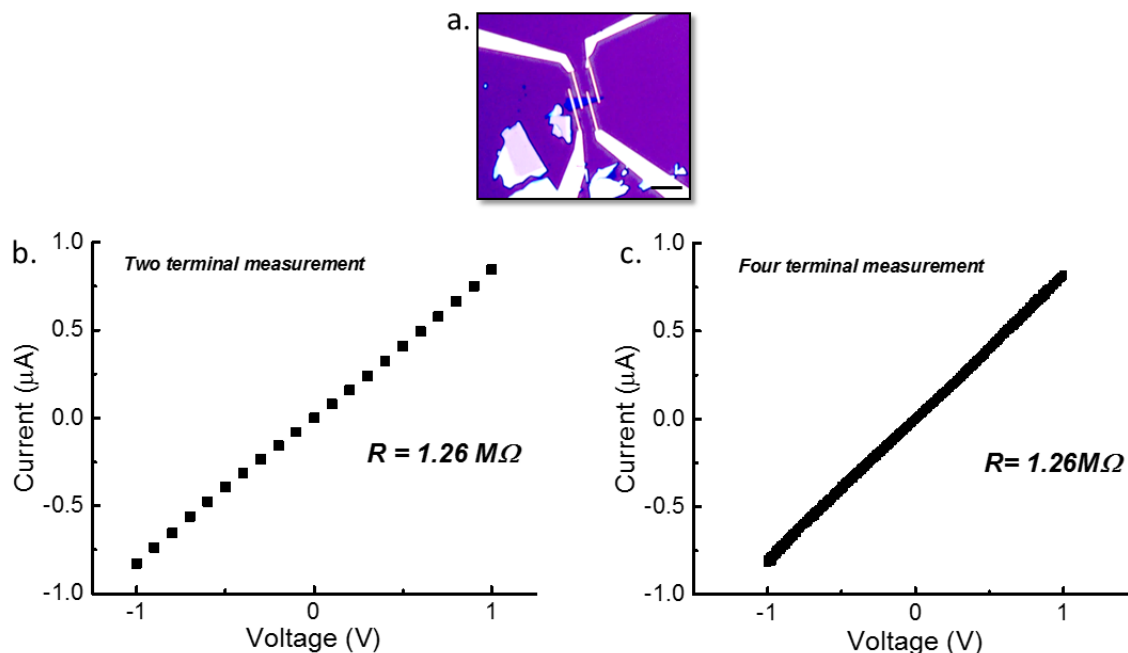


**Fig 6.4:** a) Four terminal device on a 1T phase MoS<sub>2</sub> flake. Scale bar = 5 μm b) Two terminal current-voltage measurement on the external electrodes, resistance is extracted from the inverse slope of the plot. c) Four terminal current-voltage measurement of the device, resistance extracted is close to the resistance from the two terminal measurement.

In order to make sure patterning of flakes works for devices, an interesting experiment was performed where a long flake was chosen and one half of the flake was converted to 1T phase while protecting the other half from contamination. Devices were fabricated on the 1T portion of the flake and the 2H portion of the flake. As expected device in the 2H portion of the flake showed good gate modulation with schottky contacts whereas the device in the 1T portion of the flake showed no gate modulation with ohmic contacts. Fig 6.5 shows the device image, output and transfer characteristics.

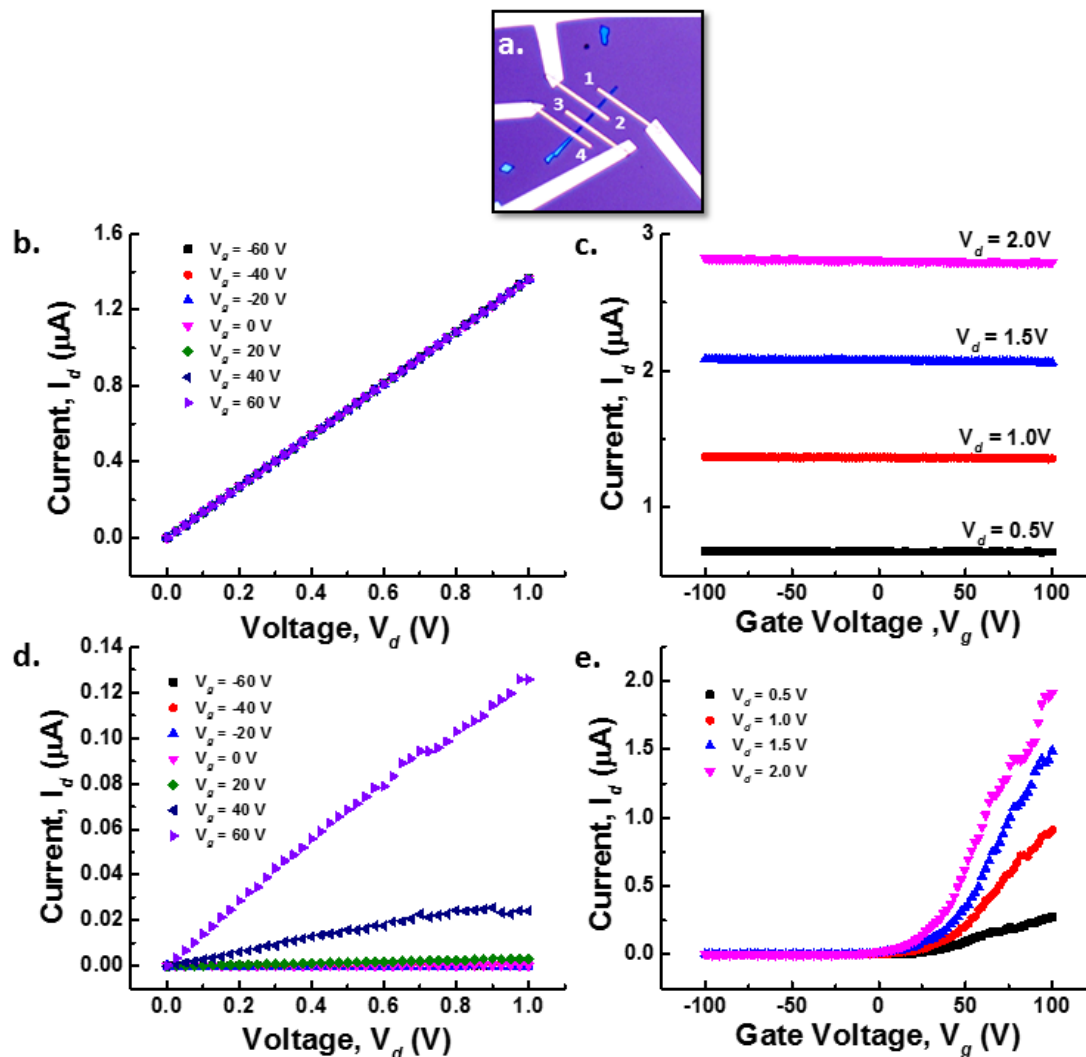


Fig 6.5: a) Devices on a MoS<sub>2</sub> flake which is half 1T (electrodes 1, 2) and half 2H phase (electrodes 3, 4) b) Output characteristic and d) Transfer characteristic of device made on 1T phase of the flake defined by electrodes 1 and 2 c) Output characteristic and e) Transfer characteristic of devices made on 2H phase of the flake defined by electrodes 3 and 4.

### 6.3 Phase engineered contacts for MoS<sub>2</sub> devices

Owing to the success in phase transformation of MoS<sub>2</sub> and patterning of the flakes with different phases, I went ahead and used the 1T phase portion of the flake as the electrode contacts. For this purpose a three step lithography process is employed where the first lithography step was to open windows on the MoS<sub>2</sub> flake. This exposed portion was converted to the 1T phase with lithium intercalation as mentioned earlier. After the phase

transformation and rinsing process, the PMMA was removed and recasted after which the same windows were reopened for metallization. 50nm gold was deposited with e-beam evaporation at a slow rate of  $0.5 \text{ \AA/s}$ . This was followed by lift off and then PMMA was recasted which was followed by lift off and gold-titanium deposition for making big pads which contact the prior deposited electrodes.

The initial devices made with this process were constantly getting shorted out giving device characteristics as shown in fig. 6.6. Upon careful analysis and characterization of the channel region, it was understood that the channel region was getting contaminated due to infusion of lithium into the channel since PMMA is not a strong mask for long periods of time.

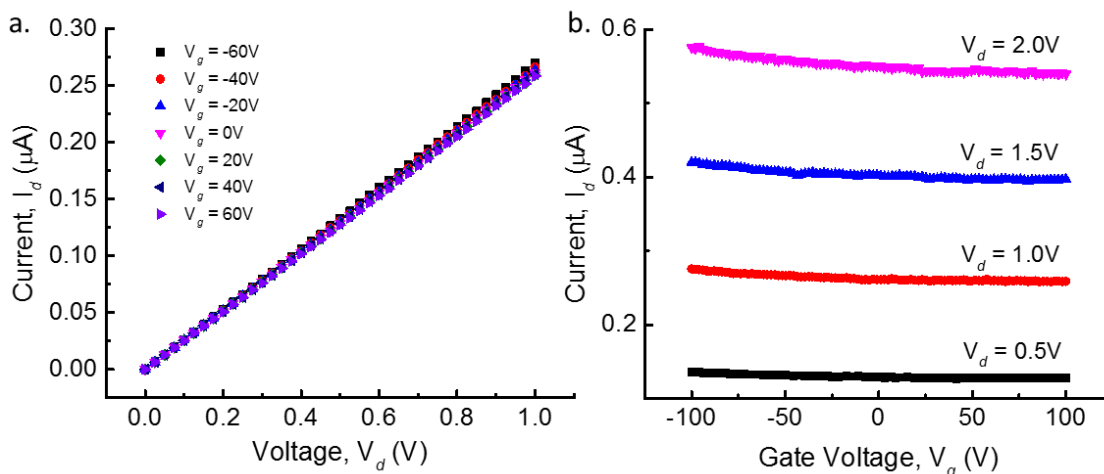


**Fig 6.6: Devices with contaminated MoS<sub>2</sub> channel. a) Output characteristics showing ohmic contacts b) Transfer characteristics showing modulation but with high metallic content.**

In order to make devices with just the contact regions of 1T phase MoS<sub>2</sub> while the channel remains unaffected was hence realized to be very challenging and a series of experiments were performed to optimize the rate of lithiation based phase transformations. For contact areas of less than  $1 \mu\text{m}^2$  with a channel length of around 2 micron, the perfect time of

lithiation would be 2 hours for mechanically exfoliated MoS<sub>2</sub> flakes with thickness less than 3nm. With these optimized conditions, devices with very high performances were realized which had record ON currents and field effect mobilities.

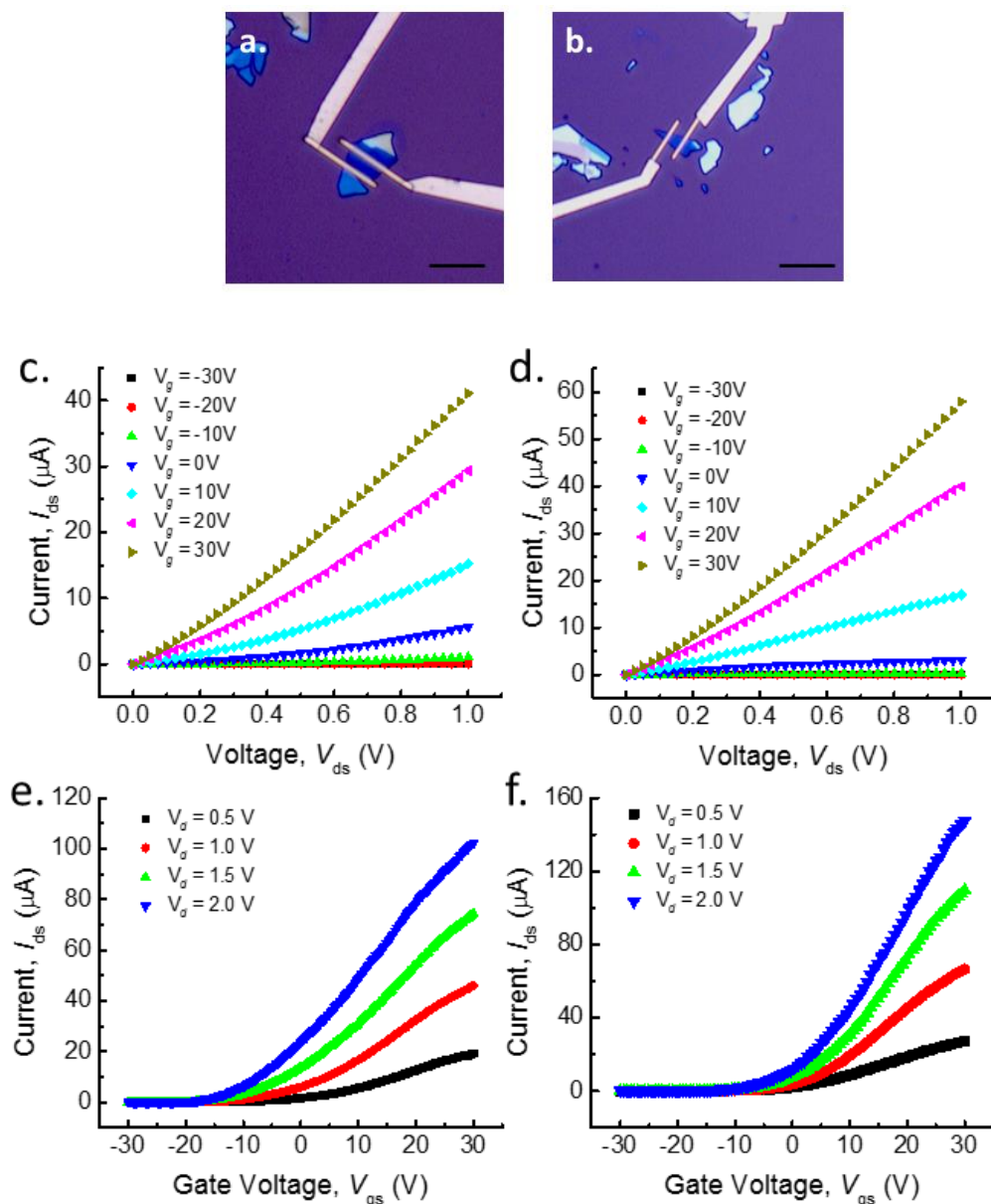


**Fig 6.7:** a, b) Devices on mechanical exfoliated MoS<sub>2</sub> flakes with 1T phase MoS<sub>2</sub> at contacts and gold deposited as electrodes. All scale bars = 5  $\mu$ m. c, d) Output characteristics showing linear characteristics representing ohmic contacts between gold and MoS<sub>2</sub>. g, h) Transfer characteristics of the devices which show a good turn on feature and good carrier mobility

Devices with 1T phase contacts showed superior and much enhanced properties than regular MoS<sub>2</sub> devices. Table 6.1 shows some of the key figures of merit of these devices. Most important thing to note here is that the drive currents of 85  $\mu\text{A}/\mu\text{m}$  is impressive since the conducting channel is just 3-4nm thick with a field effect mobility of  $\sim 50 \text{ cm}^2/\text{Vs}$ . These high values can be further improved by elimination of organic residues that might be present on the surface of MoS<sub>2</sub>.

**Table 6.1: Device properties of MoS<sub>2</sub> field effect transistors with 1T contacts**

Property	Value
ON Current ( $\mu\text{A}/\mu\text{m}$ )	85
Transconductance ( $\mu\text{S}/\mu\text{m}$ )	3.8
Mobility ( $\text{cm}^2/\text{Vs}$ )	46
ON/OFF ratio	$10^8$

### **Comparison of Au-2H and Au-1T MoS<sub>2</sub> contacted devices**

Performance of devices with gold contacts MoS<sub>2</sub> was very inconsistent and the yield of working devices was always very low. Though the fabrication of devices with gold-1T contacts had a couple of extra steps in the process, the devices worked reliably and much better. Fig. 6.8 shows the transfer characteristics of both these devices in the log and linear scale to see the higher current, better modulation and faster turn on in the Au-1T contacted devices. The turn on characteristic is compared by extracting the subthreshold slope on the transfer characteristic in the log scale. Subthreshold slope is the inverse of the slope before the device actually turns on, that is before the threshold voltage is reached. It was found that devices with gold on MoS<sub>2</sub> requires twice as much voltage to turn on compared to gold on 1T MoS<sub>2</sub> representing the quicker turn on in the latter. On an average of over 10 devices,

it was observed that devices with 1T contacts have atleast 3 times higher current and transconductances. These values are summarized in table 6.2.

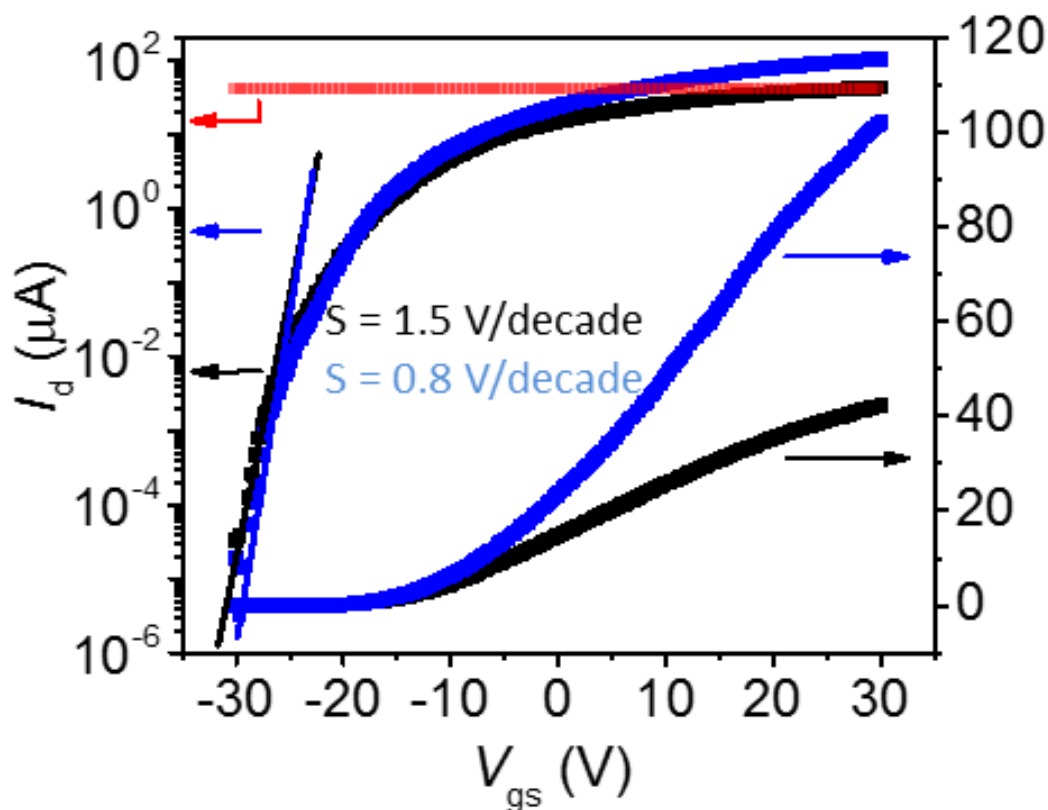


Fig 6.8: Transfer characteristics of Au-2H (black) and Au-1T (blue) contacted MoS<sub>2</sub> devices in linear and log scale.

Table 6.2: Comparison of bottom gated Au-2H and Au-1T contacted devices

Property	2H phase contacts	1T phase contacts	Ratio
ON currents ( $\mu\text{A}/\mu\text{m}$ )	30	85	2.8
Transconductance ( $\mu\text{S}/\mu\text{m}$ )	1.4	3.8	2.7
Mobility ( $\text{cm}^2/\text{Vs}$ )	19	46	2.5
ON/OFF ratio	$10^7$	$10^8$	10
Subthreshold Swing (V/dec)	1.5	0.8	0.5

### Current Saturation

Current saturation is a very important criterion for a semiconductor device and the semiconductor itself has a major role to play in it. Most of today's electronic devices such as the TFTs in displays operate in the saturation regime; Graphene devices haven't been

able to achieve saturation due to the transport of hole carriers at high drain source voltages. However, current saturation can be easily obtained in MoS<sub>2</sub> transistors irrespective of the type of contact. Fig 6.9 shows the output characteristics of both kinds of MoS<sub>2</sub> transistors. It can be observed that current saturation is much better in 1T-contacted devices with higher current levels and linear ohmic characteristics.

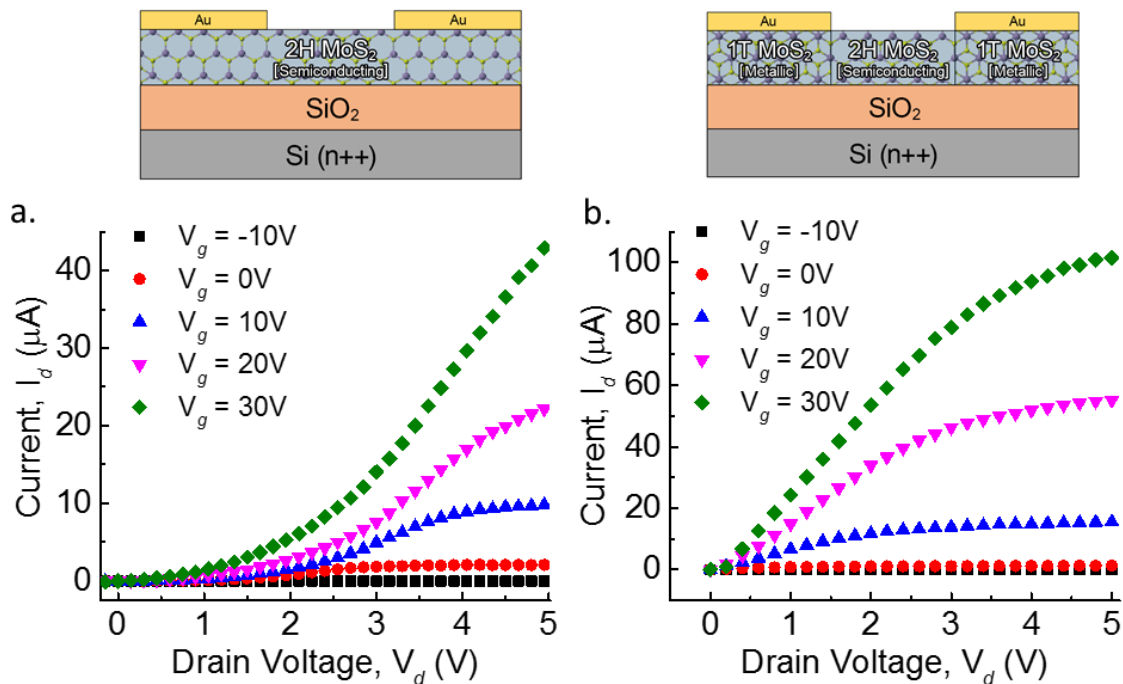


Fig 6.9: Saturated output characteristics of Au-2H and Au-1T contacted MoS<sub>2</sub> devices

### 1T contacted MoS<sub>2</sub> devices with other metals as contacts

In the hybrid MoS<sub>2</sub> device which has the 1T-2H-1T configuration, the 1T phase of MoS<sub>2</sub> play the role of charge injection and extraction layers. Owing to this, the metal deposited on 1T MoS<sub>2</sub> (gold in this case) should have no effect, minor if at all, on the device performance. In order to prove this, high work function metal, Palladium, and a low work function metal, Calcium, have been chosen as contacts to make MoS<sub>2</sub> devices. Since calcium is highly sensitive to oxygen present in air, it was covered with 40nm of gold. It

was very challenging to obtain working devices with both Pd contacts and Ca contacts, however, after numerous efforts; barely working devices were obtained with low currents. However upon phase conversion of the contacts to 1T and depositing the same metals on them, devices with reliable operation and highly enhanced performances were obtained. The gate modulation was superior and the output characteristics showed linear ohmic behavior similar to Au-1T contacted devices. The average on currents was around 20 A/m and mobilities were 20-30  $\text{cm}^2/\text{Vs}$  consistently for the 1T-contacted devices. This proved the fact that the actual barrier for the 1T contacted devices was between the 1T and 2H phase and not between the metal and 1T phase. Fig 6.10 and table 6.3 show the properties of Pd contacted  $\text{MoS}_2$  devices while Fig 6.11 and table 6.4 show the properties of Ca contacted  $\text{MoS}_2$  devices.

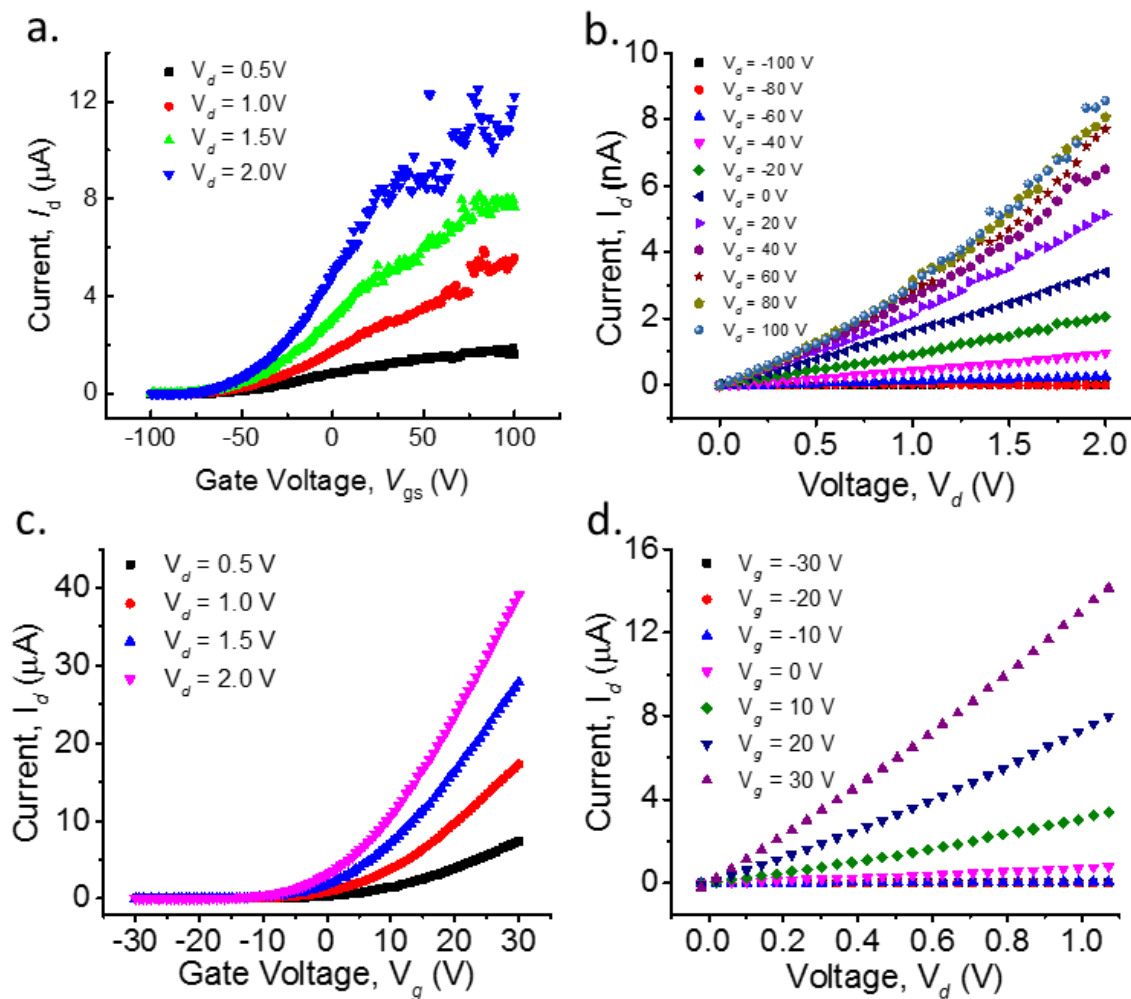


Fig 6.10: MoS<sub>2</sub> devices with Palladium contacts. a, b) Transfer and output characteristics of Pd contacted devices without 1T MoS<sub>2</sub> showing very poor device performances. c, d) Transfer and output characteristics of Pd contacted devices with 1T MoS<sub>2</sub> showing very good device performances.

Table 6.3: Comparison of Palladium contacted MoS<sub>2</sub> devices

Property	2H Phase contacts	1T Phase contacts
ON current ( $\mu\text{A}/\mu\text{m}$ )	0.02	21
ON/OFF Ratio	$10^4$	$10^7$
Mobility ( $\text{cm}^2/\text{Vs}$ )	0.02	18

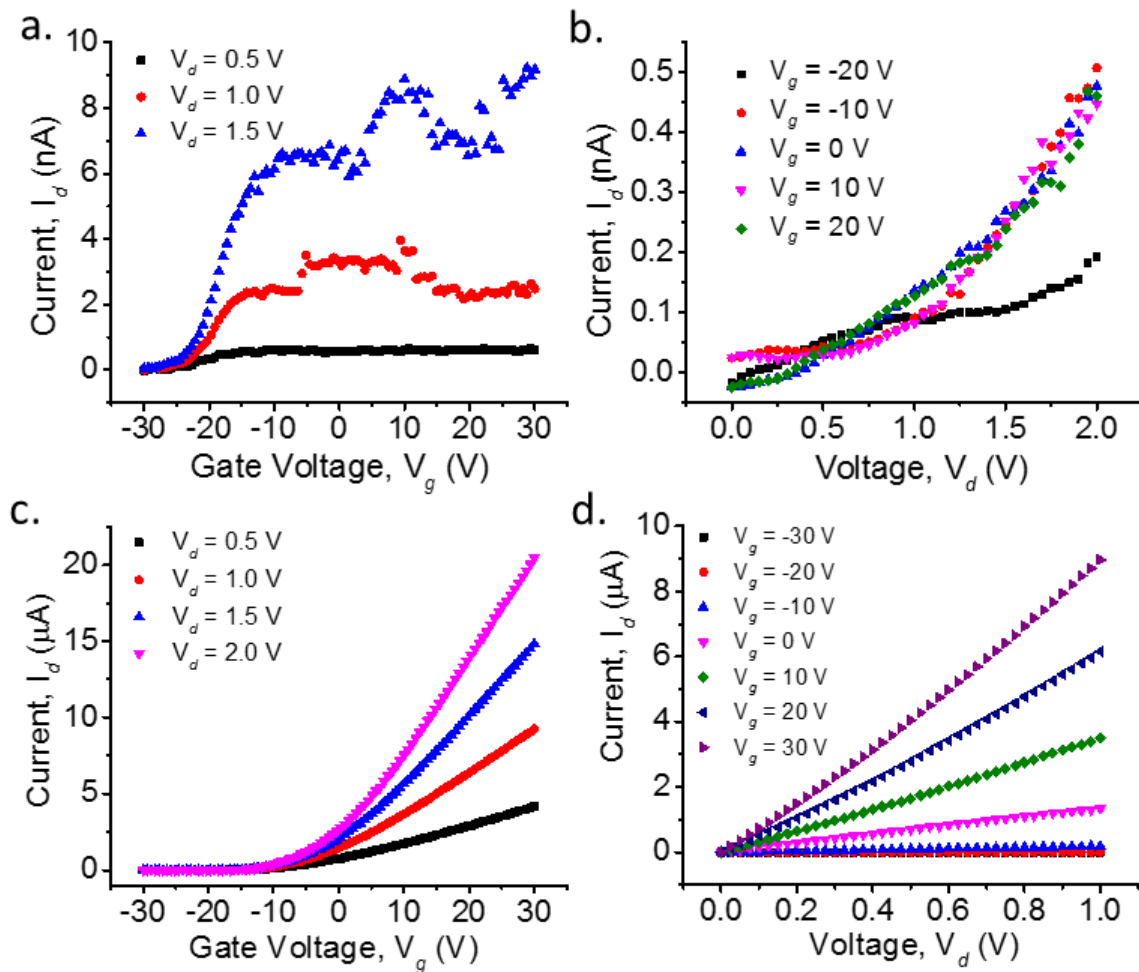


Fig 6.11: MoS<sub>2</sub> devices with Calcium contacts. a, b) Transfer and output characteristics of Ca contacted devices without 1T MoS<sub>2</sub> showing very poor device performances. c, d) Transfer and output characteristics of Ca contacted devices with 1T MoS<sub>2</sub> showing very good device performances.

Table 6.4: Comparison of Calcium contacted MoS<sub>2</sub> devices

Property	2H Phase contacts	1T Phase contacts
ON current ( $\mu$ A/ $\mu$ m)	0.01	21
ON/OFF Ratio	$10^3$	$10^8$
Mobility ( $\text{cm}^2/\text{Vs}$ )	0.03	28

## 6.4 Chapter Summary

This chapter discussed the fabrication of 1T phase MoS<sub>2</sub> devices and 1T phase contacted MoS<sub>2</sub> devices. It provided evidence of the absence of lithium in 1T phase MoS<sub>2</sub> which is very important to note since we want the improvement in devices to come from 1T MoS<sub>2</sub> and not from the presence of impurities. The evidence was provided in the form of EELS and NRA measurements which showed negligible amounts of lithium in 1T phase MoS<sub>2</sub>. Electrical measurements on 1T phase devices showed that the carrier concentration is very high in the material due to which the Fermi level cannot be tuned as like in metals. Devices fabricated with 1T phase as contacts exhibited superior performances. The output characteristics were perfectly linear proving ohmic contacts and the measured current levels and extracted mobilities were much higher than pure Au-2H devices. Furthermore, electrodes of Pd and Ca deposited on 1T MoS<sub>2</sub> contacts did not change the device performances substantially which proved that the actual carrier injection is taking place from 1T MoS<sub>2</sub> rather than the metal. The next chapter will discuss the evaluation of the contact resistance from TLM based measurements in order to quantify the actual amount by which the contact resistance has been reduced. It will also include the results of schottky barrier heights and the fabrication of top gated devices with a variety of dielectrics.

## Chapter 7

### Evaluation of Contact resistance and Schottky barrier height

#### 7.1 Transmission line measurement (TLM)

In order to determine the contact resistance between metal and MoS<sub>2</sub>, the TLM method was employed. Devices were fabricated in the TLM model with Au contacts on MoS<sub>2</sub> and Au contacts on 1T MoS<sub>2</sub>. Each structure had 4 devices with increasing channel lengths. Current-voltage measurements were performed on each of these devices and resistance was extracted by taking the inverse slope of the IV-measurement data. This resistance was normalized with the device dimension and plotted as a function of device channel length. A linear fit was made to the points and the line was extrapolated to find the y-intercept. The value of resistance at the y-intercept represents the contact resistance of the device coming from the two contacts and hence two times the contact resistance. Half of this value represents the contact resistance that exists between metal and MoS<sub>2</sub>. Fig. 7.1 has the TLM analysis for gold on MoS<sub>2</sub> devices and Fig. 7.2 has the TLM analysis for gold on 1T MoS<sub>2</sub> devices. The contact resistance was found to reduce by a factor of 5 for Au on 1T MoS<sub>2</sub> devices denoting a significant drop in the schottky barrier height between metal and 1T MoS<sub>2</sub> compared to that between metal and 2H MoS<sub>2</sub>. Record low contact resistance was obtained for MoS<sub>2</sub> devices with 1T contacts.

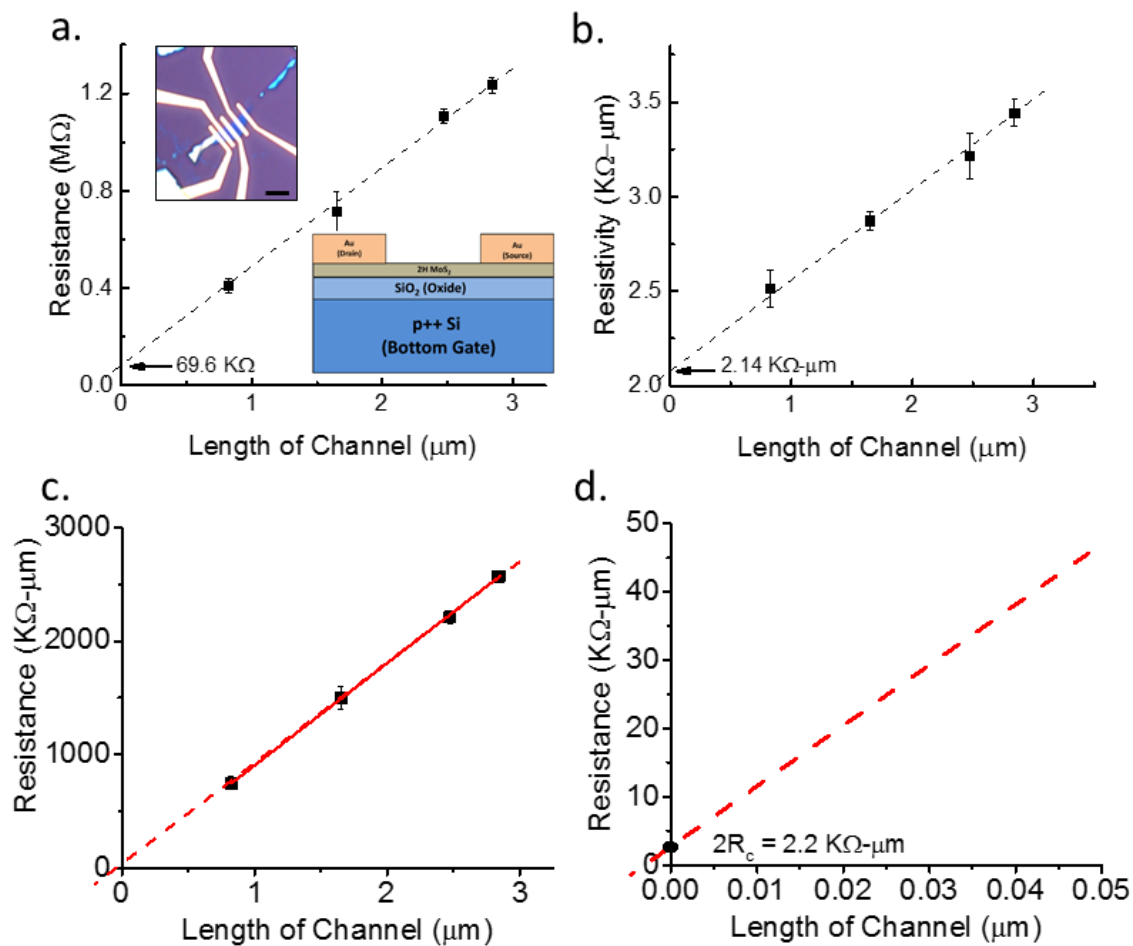


**Fig 7.1.** Contact resistance analysis with TLM for Au-2H contacts on MoS<sub>2</sub>. a) Resistance as a function of channel length. Scale bar = 5 μm b) Resistivity of the devices as a function of channel length c) Resistance normalized to device geometry as a function of channel length d) Magnified version of (c) which gives y intercept which represents two times contact resistance

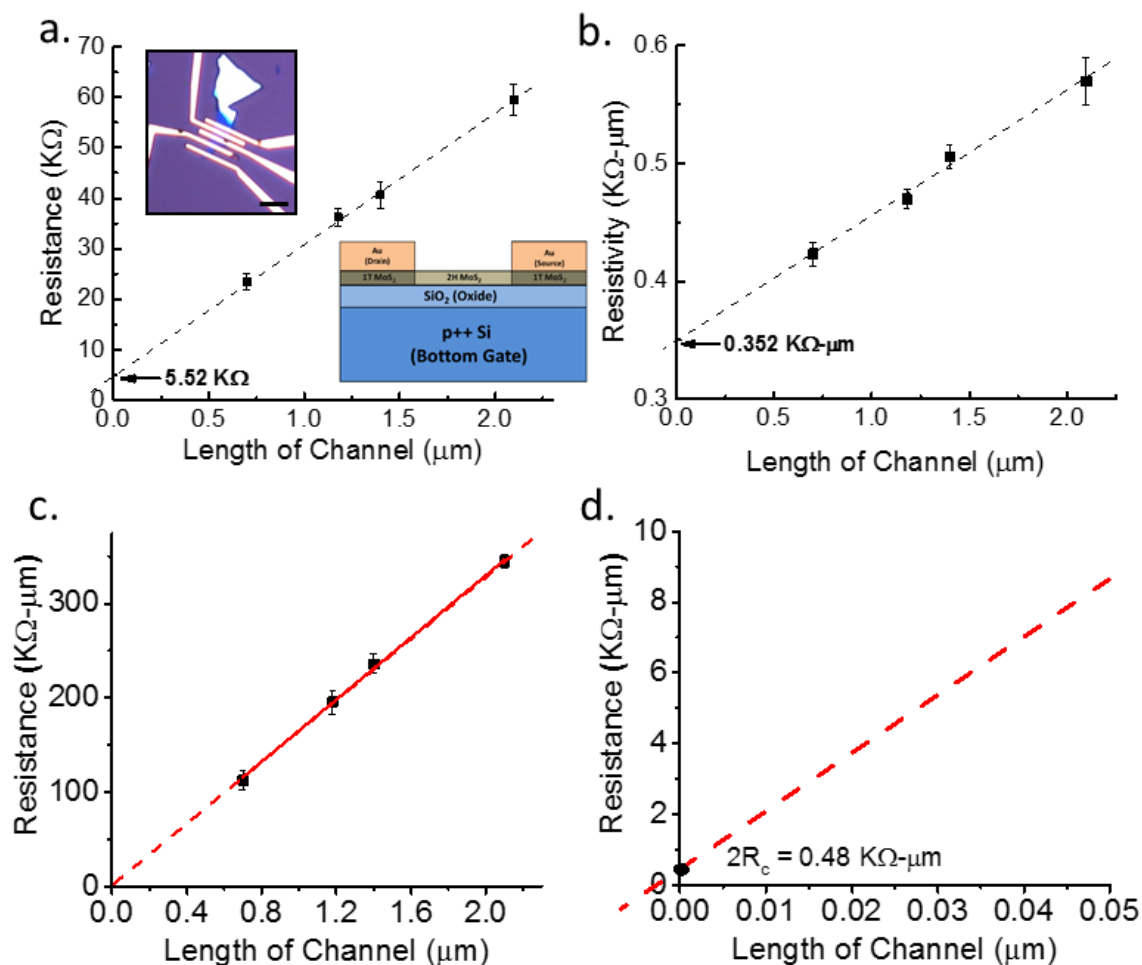


**Fig 7.2. Contact resistance analysis with TLM for Au-1T contacts on MoS<sub>2</sub>.** a) Resistance as a function of channel length. Scale bar = 5 μm b) Resistivity of the devices as a function of channel length c) Resistance normalized to device geometry as a function of channel length d) Magnified version of (c) which gives y intercept which represents two times contact resistance

### Contact resistance dependence on gate voltage

Applying a gate voltage to the device can further reduce this contact resistance. I extracted the contact resistance at gate voltages of 10V, 20V and 30V by measuring the drain-source current at each of these gate voltages. Applying a gate voltage increases the channel carrier concentration thereby reducing the schottky barrier height between metal and MoS<sub>2</sub>. However in the case of metal and 1T MoS<sub>2</sub>, since the schottky barrier is already low, the contact resistance dropped by ~3 times from 0V gate voltage to 30V gate voltage compared

to the 4 times reduction in the case of Au on 2H MoS<sub>2</sub> devices. Fig 7.3 has the contact resistance dependence on gate voltage for both kinds of devices.

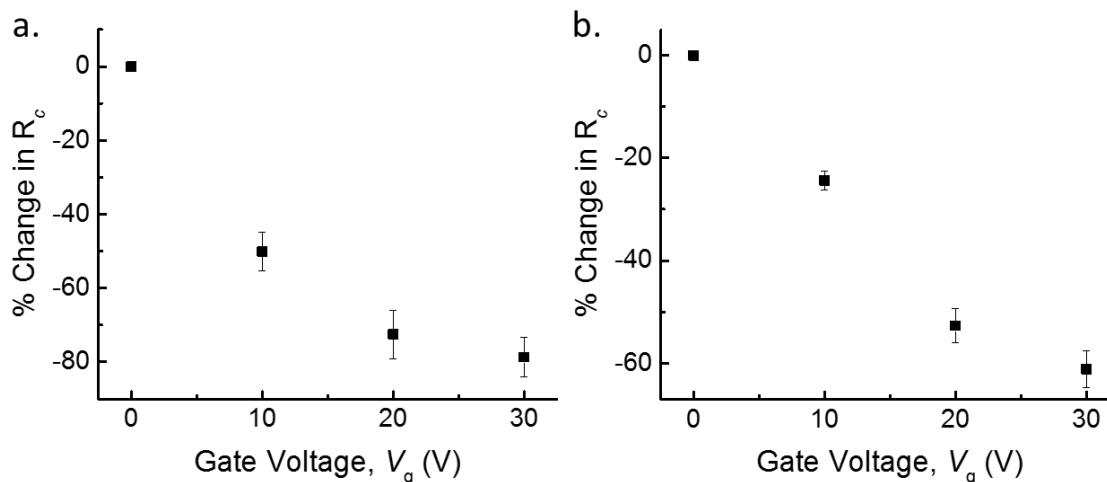
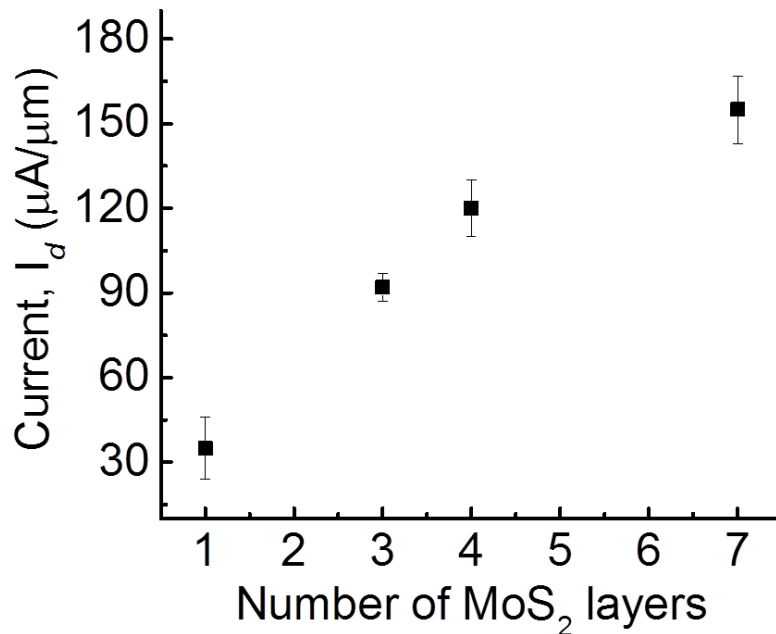


Fig 7.3. Gate dependence of Contact resistance with a) Au-2H contacts and b) Au-1T contacts

### Contact resistance dependence on thickness of MoS<sub>2</sub>

It would be a valid to claim that in a thick film of MoS<sub>2</sub>, the phase transition occurs only the top layer since only the top layer of MoS<sub>2</sub> is in contact with butyl lithium. In order to study this effect, devices were made on MoS<sub>2</sub> films which ranged from a monolayer to 7 layers. All these flakes were converted to 1T phase MoS<sub>2</sub> through lithium intercalation for the same amount of time and the saturation current was measured. We found that as the thickness of the film increased the current levels increased. If only the top layer is converted, current would not vary so substantially, since all the current would be injected from this layer which would create a current bottleneck. Since all the layers below are converted, we see the increase in current as seen in figure 7.4 below.



**Fig 7.4. Current versus number of layers for 1T MoS<sub>2</sub> devices**

We have proved the same theory through non-electrical measurements as well. To do this, we performed NRA to extract Li concentration as a function of depth. We took a multilayered MoS<sub>2</sub> sample and performed butyl lithium treatment in the same manner as for devices. We found that lithium diffuses into the top 6 layers consistent with the electrical measurement data. The corresponding measured Lithium concentration values are given below:

1<sup>st</sup> layer – 6% Li

2<sup>nd</sup> layer – 3% Li

3<sup>rd</sup> layer – 2% Li

4<sup>th</sup> layer – 1% Li

5<sup>th</sup> layer – 0.7% Li

6<sup>th</sup> layer – 0.4% Li

However after washing, we cannot measure any Li even in these multilayered samples which is a very good sign that our devices have no contamination from Li and all the improvement in conductivity is solely due to the presence of 1T phase MoS<sub>2</sub>.

In order to test for contact resistance variations with thickness, TLM was performed on devices which had thickness of upto 6 layers. The variations were not substantial. However when the thickness was more than 10 layers, the contact resistance increased to 850  $\Omega$ - $\mu$ m for Au-1T devices and  $\sim$ 30 k $\Omega$ - $\mu$ m for Au on MoS<sub>2</sub> devices. This is because in the case of multilayer flakes there are increased number of 1T-2H interfaces which will account for an increase in the contact resistance. Fig. 7.5 below shows the TLM results for multilayer MoS<sub>2</sub> devices with the device photos in the insets.

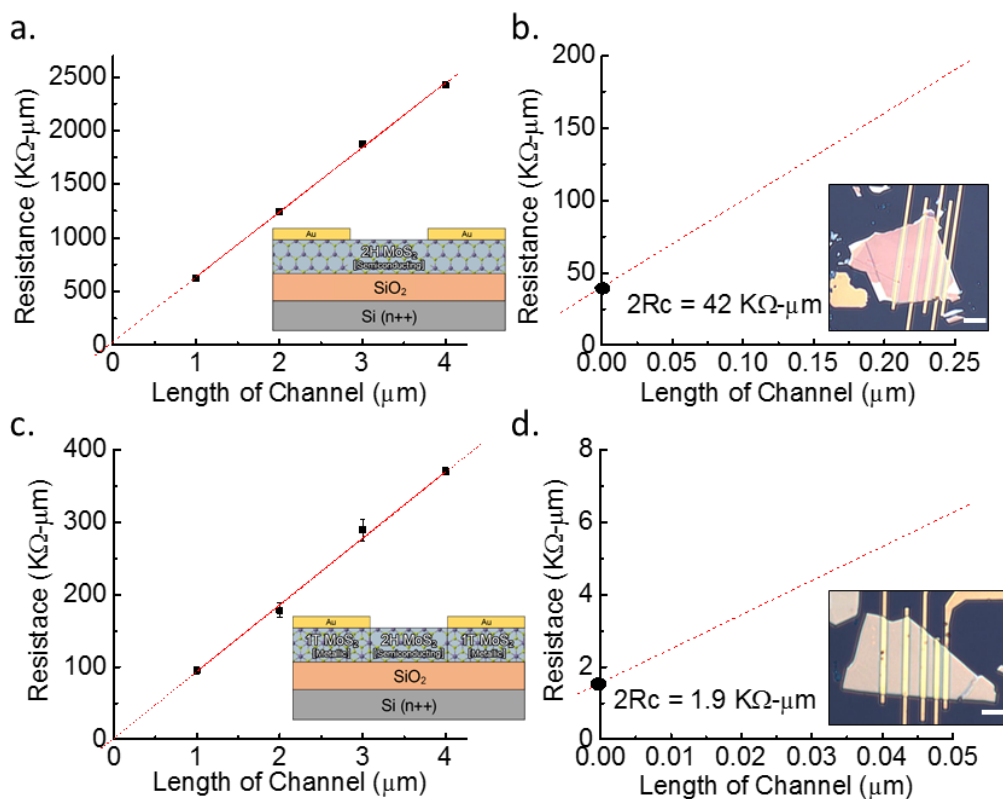


**Fig 7.5. Contact resistance analysis for multilayer MoS<sub>2</sub> flakes. Resistance as a function of channel length for (a) Au-2H contacts and (b) Au-1T contacts. b, d Magnified versions of (a) and (c)**

## 7.2 Low Temperature measurements – Schottky barrier height

When measuring metal-semiconductor systems with varying temperature and gate voltage, the charge conduction mechanisms which are involved are the thermionic emission and tunneling. Thermionic emission occurs when the gate voltage is sufficiently low where the device is in the OFF state and current starts to increase as temperature is increased, that is the carrier flow is assisted due to energy provided by the heat. Tunneling occurs when the device is in the ON state and the metal semiconductor barrier is sufficiently low so that the charge carriers just tunnel through the barrier<sup>178</sup>. Fig 7.6 below depicts these two charge conduction mechanisms.

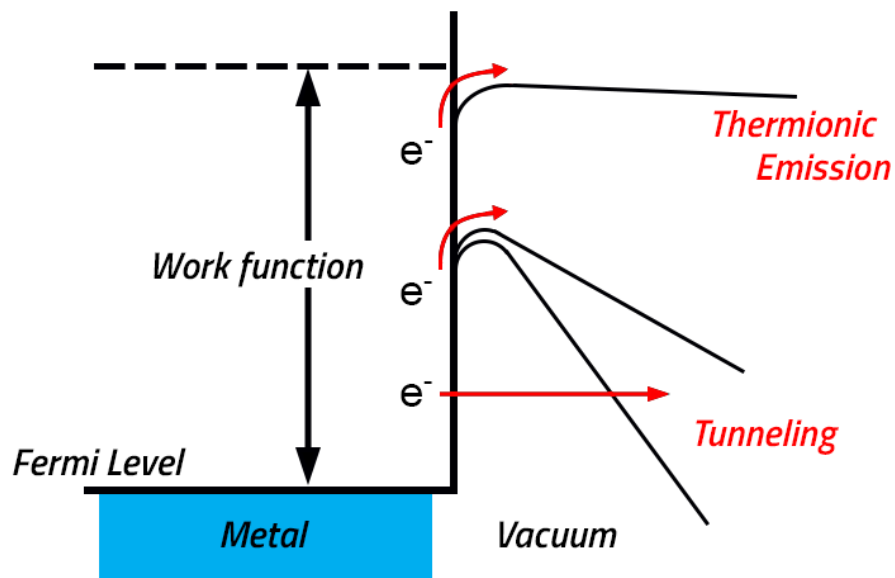
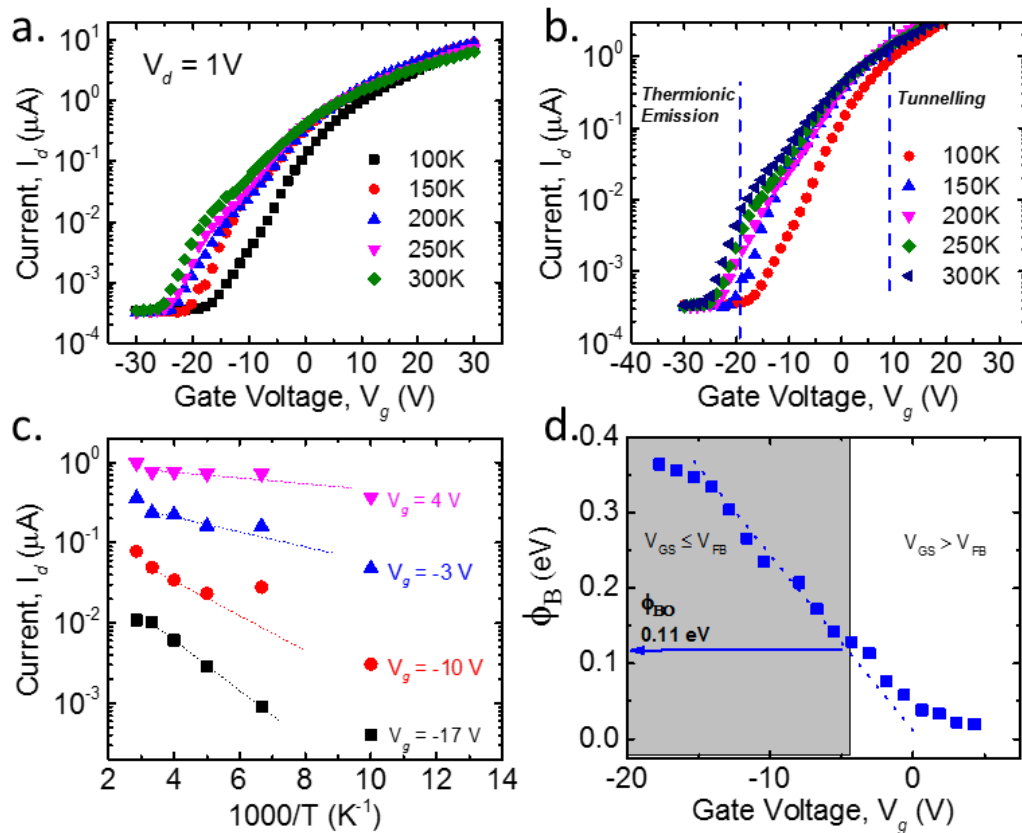


Fig 7.6: Charge conduction states at metal-semiconductor interface.

### Schottky barrier height – True and efficient

True schottky barrier height is the difference in the work function of the metal and electron affinity of the semiconductor at the flat band condition. Due to charge interaction at the metal semiconductor interface, the bands in the semiconductor are not flat, so we need to apply a voltage on the gate in order to make the surface potential on the substrate zero and

establish the flat band condition where the schottky barrier height measured would be the true schottky barrier height which is independent of the trap states in the semiconductor. However the current flowing between the metal semiconductor junction is determined by the effective schottky barrier height which varies with variation in the charge carrier concentration of the semiconductor which in turn depends on the gate voltage and the trap states in the semiconductor. In order to do this, it is mandatory to distinguish between thermionic emission and tunneling states of conduction for which temperature dependent field effect measurements.



**Fig 7.7:** Low temperature measurements on Au-2H contacted MoS<sub>2</sub> devices. a) Transfer characteristics at different temperatures b) Charge conduction states recognized in the transfer characteristics c) Arrhenius plots at different gate voltages d) Extraction of true schottky barrier height after plotting the effective schottky barrier heights at different gate voltages.

Fig. 7.7a and b show the temperature dependent transfer characteristics of MoS<sub>2</sub> field effect transistors which have gold as contacts. We can see the increase in current as the temperature is raised especially in the off state of the device. The threshold voltage where the device turns on increases in magnitude as temperature is increased due to increased carrier concentration in the channel. This change in threshold voltage or early turn on of the device is actually due to carriers which are generated thermally and so this state can be recognized as the thermionic emission state. After the gate voltage is high enough where the channel is accumulated with charge carries, the transfer curves start getting close to each other even while the temperature is changing and this conduction state is recognized as tunneling. These charge conduction mechanisms are identified in fig. 7.7b. In between these two states, the conduction is through thermal emission and tunneling and it is important to identify the exact transition point of the transition to tunneling since that particular voltage is the flat band voltage and the schottky barrier height at that point is the true schottky barrier height.

In order to do this lets consider the Arrhenius equation which is given below:

$$I_{DS} \propto AT^2 \exp\left(-\frac{q\phi_B}{k_B T}\right)$$

Here  $I_{DS}$  is the drain source current, A is the Richardson's constant, T is temperature, q is the charge of an electron,  $\phi_B$  is the effective schottky barrier height and  $k_B$  is the Boltzmann constant.

This equation can be rearranged to give the following form

$$\frac{d\ln(I_{DS})}{d(1000/T)} \approx -\frac{q\phi_B}{k_B} \text{ (meV)}$$

From the equation above and the data from the device transfer curves, I generated the Arrhenius plot for each gate voltage in between the thermal emission and tunneling charge conduction states. Some of the curves are shown in fig 7.7c. Effective schottky barrier height at each gate voltage is extracted from the Arrhenius plot and plotted as a function of gate voltage. The gate voltage at which the schottky barrier height tends to curve away from the linear dependence is where the flat band condition occurs that's because after the gate voltage reaches this condition carriers are transferred through thermal assisting tunneling as well. From fig 7.7d, the true schottky barrier height and flat band voltage is extracted by generating a plot of  $\Phi_B$  vs  $V_g$ . The true schottky barrier height between gold and MoS<sub>2</sub> is ~0.11eV at  $V_{FB} = -4V$

Similar measurements were performed on Au on 1T MoS<sub>2</sub> contacted devices. Fig 7.8 shows the results. It can be observed that the current and threshold voltage variation with temperature is lower than in the case of Au on MoS<sub>2</sub> devices. The true schottky barrier height between gold and 1T MoS<sub>2</sub> is ~40 meV at  $V_{FB} = -7V$ . This is a much lower value compared to that of gold and 2H MoS<sub>2</sub> and hence explains the reduced contact resistance and enhanced device performances with 1T contacts.

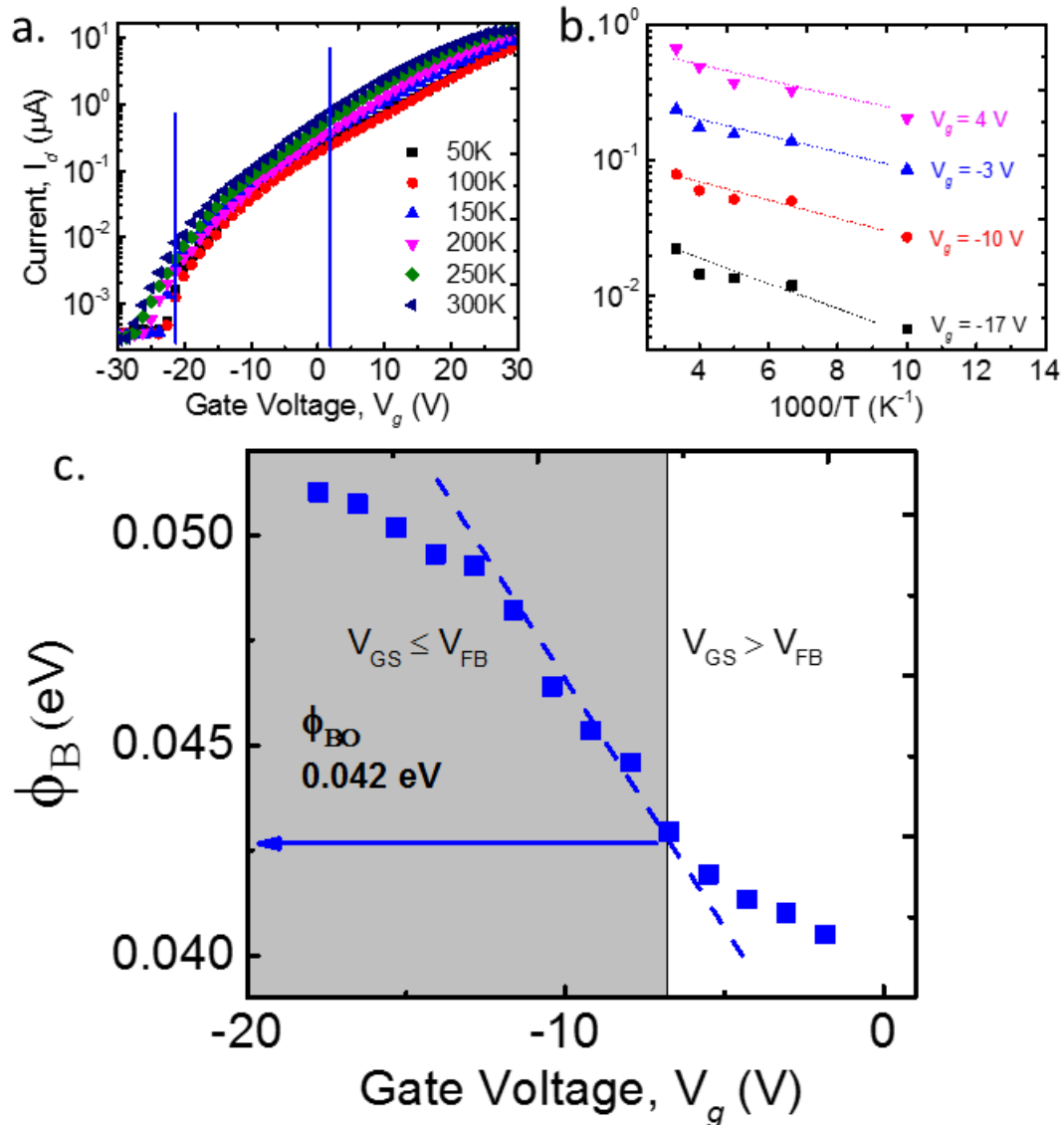


**Fig 7.8:** Low temperature measurements on Au-1T contacted MoS<sub>2</sub> devices. a) Charge conduction states recognized in the transfer characteristics b) Arrhenius plots at different gate voltages c) Extraction of true Schottky barrier height after plotting the effective Schottky barrier heights at different gate voltages.

### 7.3 Top gate devices

Top gate devices allow isolation of gate electrode for each individual device, this coupled with a high  $k$  dielectric and thin dielectric layer allows efficient control of carrier concentration for fast switching and enhanced performance devices. Fabrication of top gated devices required deposit of dielectric on pre-fabricated devices. We have tried four

different dielectrics which consisted e-beam evaporated  $\text{Al}_2\text{O}_3$ , atomic layer deposited  $\text{HfO}_2$  and plasma enhanced chemical vapor deposited  $\text{SiO}_2$  and  $\text{Si}_3\text{N}_4$ . The following section describes the deposition of these dielectrics on  $\text{MoS}_2$  devices.

**Aluminum Oxide ( $\text{Al}_2\text{O}_3$ ):** Alumina was deposited on  $\text{MoS}_2$  devices with e-beam evaporation at a very slow rate of  $0.5\text{\AA}/\text{s}$ . However, the quality of dielectric deposited through e-beam evaporation was very low with the film consisting of pin holes<sup>170</sup>, this caused shorting of the top gate with the source/drain electrodes hence we moved to other deposition schemes like atomic layer deposition (ALD) and plasma enhanced chemical vapor deposition (PECVD) which give better dielectric films.

**Hafnium Oxide ( $\text{HfO}_2$ ):** Atomic layer hafnium oxide coatings were deposited onto the devices using a Picosun SUNALE™ R-150B ALD system (Detroit, MI) by following growth conditions from reference S4<sup>62</sup>. Tetrakis-dimethylamido hafnium (IV) (TDMAH, SAFC Hitech (USA)) was used as the hafnium metal precursor with deionized water as the oxygen source. TDMAH preheated to  $75^\circ\text{C}$  was delivered to the reaction chamber at 100 sccm with a pulse time of 1.0 second followed by a purge of nitrogen for 5.0 seconds. Two steps of water followed at 200 sccm for 1.0 second with a purge of nitrogen at 200 sccm for 10 seconds. The chamber temperature was maintained at  $200^\circ\text{C}$  during the completion of 200 cycles or approximately a 20 nm film, where one cycle consisted of TDMAH and two water pulses with nitrogen purges in between. Devices made with this recipe were not conductive at all. We hypothesized that the combination of the heat at  $200^\circ\text{C}$  and presence of water resulted in the oxidation of the thin  $\text{MoS}_2$  flake resulting in the loss of its conductivity<sup>179</sup>.

Lower temperature depositions were not investigated because higher reaction times of oxygen would be required to achieve the necessary surface chemistry that would promote hafnium oxide nucleation and this would not help in preventing the oxidation of the MoS<sub>2</sub> flakes. Hence we went on to modify the recipe to grow better hafnium oxide on MoS<sub>2</sub> without adversely killing the properties of MoS<sub>2</sub>. TDMAH preheated to 75°C was delivered to the reaction chamber at 100 sccm with a pulse time of 1.9 seconds. Water followed at 200 sccm for 0.1 seconds with a purge of nitrogen at 200 sccm for 40 s between each pulse of precursor. The chamber temperature was maintained at 200°C during the completion of 200 cycles resulting in approximately a 20 nm film, where one cycle consisted of TDMAH and water pulses with nitrogen purges in between. Many a times this resulted in a discontinuous film which resulted in the shorting of gate and source/drain electrodes. Similar problem was experienced by McDonnell et al where they observed non conformal growth of HfO<sub>2</sub> on MoS<sub>2</sub>. We tried a longer deposition time by doing 350 cycles which resulted in approximately 35 nm film. This growth recipe of hafnium oxide resulted in reasonably working devices but not impressive device characteristics. Therefore we shifted our focus from hafnium oxide dielectric to other dielectrics to make better top gated MoS<sub>2</sub> devices.

**Silicon Nitride deposition (Si<sub>3</sub>N<sub>4</sub>):** Plasma enhanced chemical vapor deposition (Trion Orion II CVD) was used to produce a thin film of Silicon nitride (Si<sub>3</sub>N<sub>4</sub>) coating the device. A purge step of Argon at 10 sccm for 30 seconds at 10 mT preceded deposition. Silane (SiH<sub>4</sub>) at a rate of 16 sccm and nitrogen at 32 sccm with argon as a carrier gas (24 sccm) served as precursors for deposition of the Si<sub>3</sub>N<sub>4</sub> dielectric layer. The chamber was maintained at 100 °C for the duration of deposition and the pressure remained constant (10

mT). During deposition the inductively coupled plasma (ICP) power was 650 watts. A deposition time of 14 seconds resulted in a  $\text{Si}_3\text{N}_4$  film approximately 20 nm in thickness. This was estimated by deposition of previous  $\text{Si}_3\text{N}_4$  films, optimized for a bare silicon surface using a Nanospec Reflectometer. Following deposition the chamber was purged once more.

**Silicon dioxide deposition ( $\text{SiO}_2$ ):** Similar conditions were used for the deposition of a 20 nm thin film of silicon dioxide ( $\text{SiO}_2$ ). In addition to the purge steps, during deposition an ICP power of 500 watts was applied. Precursors were supplied for 10 seconds and included, nitrous oxide at a rate of 32 sccm and  $\text{SiH}_4$  at a rate of 16 sccm with Ar as a carrier gas (24 sccm).

**Top gate devices fabrication:** After depositing dielectric on working devices, top gate was patterned in between the source and drain electrodes using e-beam lithography and Au-Ti (20nm of titanium and 50nm of gold) was deposited using e-beam evaporation as mentioned earlier. Care was taken during patterning that the top gate electrode lies in between the source and drain electrodes without going over any of them in order to avoid sporadic capacitance effects which would hamper the gate electrostatics.

### 7.3.1 Devices with $\text{HfO}_2$ dielectric

Top gate  $\text{MoS}_2$  devices made with  $\text{HfO}_2$  dielectric have been mentioned in literature and owing to the high dielectric constant in  $\text{HfO}_2$ , we tried to fabricate devices with  $\text{HfO}_2$  dielectric. Unfortunately during the  $\text{HfO}_2$  deposition,  $\text{MoS}_2$  got oxidized due to its inorganic nature and the conductivity got severely reduced. Fig 7.9 a,b and c show the bottom gate device photo, transfer and output characteristics of the device. Fig 7.9 d, e and

Fig 7.9 shows the top gate device, transfer and output characteristics. From the output characteristics, we note that the currents levels have dropped by almost three orders in magnitude. All working devices with HfO<sub>2</sub> top dielectric showed similar behavior. The sub threshold swings extracted from the transfer characteristics came to be around 500 mV/decade. Prior to HfO<sub>2</sub> deposition, these devices showed ON/OFF ratios in the range of 10<sup>7</sup> in the bottom gated configuration but after HfO<sub>2</sub> dielectric on top, they showed only 10<sup>4</sup>. We attribute this loss in conductivity to the high temperature (200 °C) exposure of MoS<sub>2</sub> in the presence of water vapor which resulted in the oxidation of the flake<sup>180</sup>.

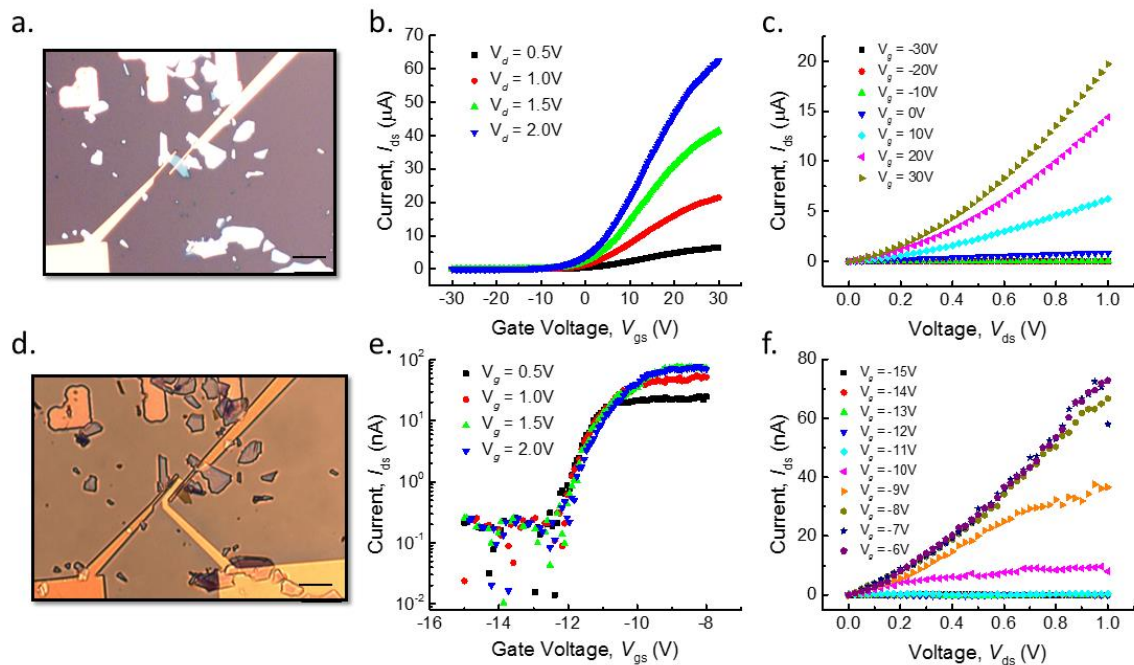


**Fig 7.9: Top gate device characteristics with hafnium oxide dielectric. a) Device photo of bottom gated device. Scale bar = 5 μm b) Corresponding transfer characteristics c) output characteristics of the bottom gated device d) Device photo of top gated transistor with HfO<sub>2</sub> dielectric e) Corresponding transfer characteristics c) output characteristics of the top gated device.**

### 7.3.2 Devices with SiO<sub>2</sub> dielectric

Fig 7.10 a, b and c show the bottom gate device photo, transfer and output characteristics of the device. Fig 7.10 d, e and f show the top gate device, transfer and output

characteristics with SiO<sub>2</sub> dielectric. Though there is a drop in current levels as seen from the output characteristics, the turn on characteristics as seen in the transfer characteristics of fig 7.10 e are much better. The sub threshold swings extracted from the transfer characteristics came to be around 250 mV/dec. Prior to SiO<sub>2</sub> deposition, these devices showed ON/OFF ratios in the range of 10<sup>7</sup> in the bottom gated configuration and after SiO<sub>2</sub> dielectric on top, they showed ~10<sup>5</sup>. Due to this loss of conductivity, I chose a dielectric which is free of oxygen, PECVD deposited silicon nitride.

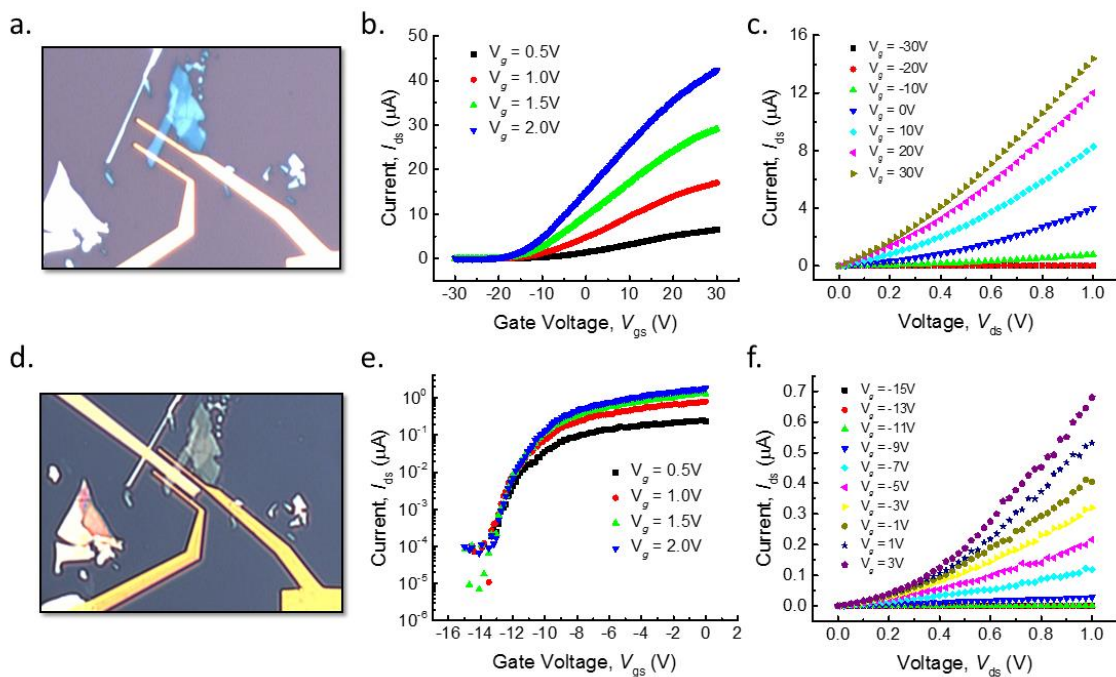


**Fig 7.10: Top gate device characteristics with silicon dioxide dielectric a) Device photo of bottom gated device. Scale bar = 5  $\mu\text{m}$  b) Corresponding transfer characteristics c) output characteristics of the bottom gated device d) Device photo of top gated transistor with SiO<sub>2</sub> dielectric e) Corresponding transfer characteristics c) output characteristics of the top gated device.**

### 7.3.3 Devices with Si<sub>3</sub>N<sub>4</sub> dielectric

The best results for top gated devices were obtained for silicon nitride dielectric. Fig 7.11 a, b and c show the device photo and device results of bottom gated device. After dielectric deposition and top gate fabrication, fig 7.11d, e and f show the top gate device results. The

current levels dropped by a minimal amount and the transport was fantastic. The ON/OFF ratio was maintain at  $10^7$  and a good subthreshold swing of  $\sim 100$  mV/dec was obtained. Silicon nitride is oxygen free and its deposition has been done at less than  $100$  °C and hence had no detrimental effect on the conduction of  $\text{MoS}_2$ .

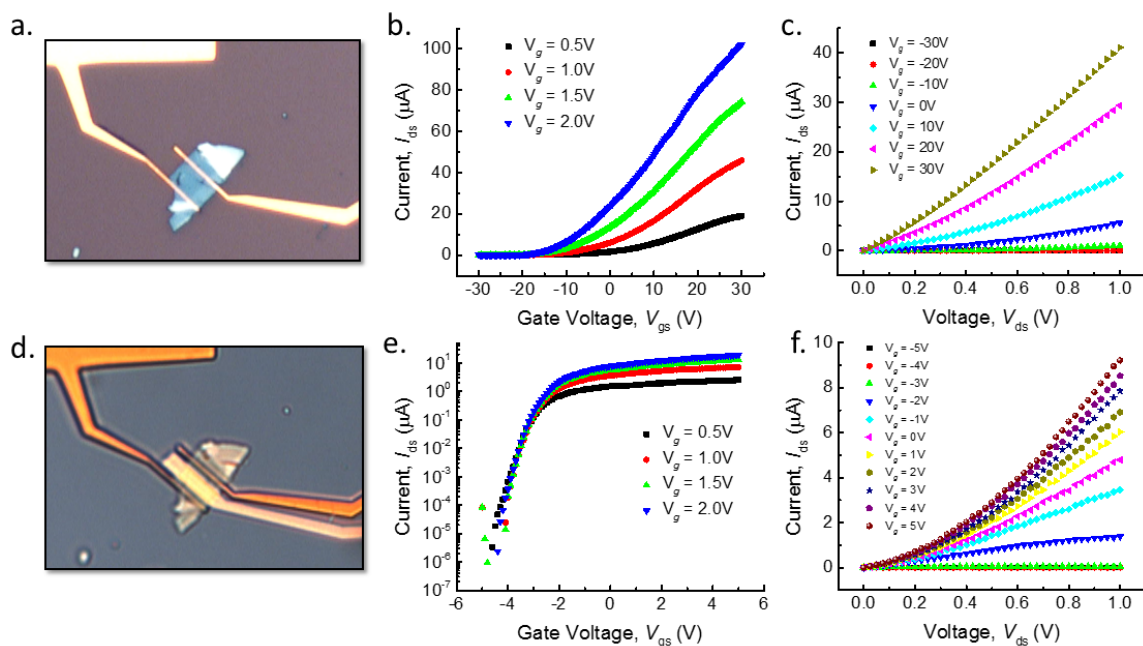


**Fig 7.11: Top gate device characteristics with silicon nitride dielectric a) Device photo of bottom gated device. Scale bar =  $5 \mu\text{m}$  b) Corresponding transfer characteristics c) output characteristics of the bottom gated device d) Device photo of top gated transistor with  $\text{Si}_3\text{N}_4$  dielectric e) Corresponding transfer characteristics c) output characteristics of the top gated device.**

## 7.4 Comparison of top gated devices

Owing to the success in making state of the art devices with silicon nitride dielectric, I went ahead and made devices with and without 1T phase contacts. Fig 7.12 shows the transfer characteristics of both the types of top gate devices. We can see the higher currents and faster turn-ons in devices with 1T contacts. Table 7.1 compares the device performance of both kinds of devices.

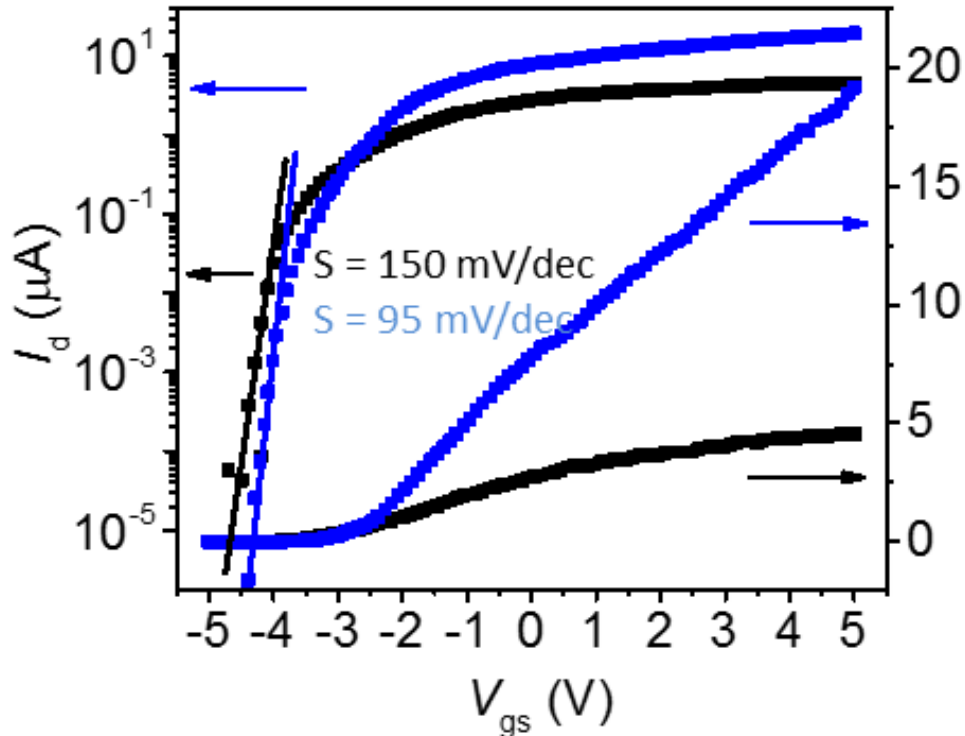


Fig 7.12: Comparison of top gate device transfer characteristics with and without 1T contacts

Table 7.1: Comparison of top-gated devices with and without 1T contacts

Property	2H phase contacts	1T phase contacts	Ratio
ON currents ( $\mu\text{A}/\mu\text{m}$ )	3	16	5.3
Transconductance ( $\mu\text{S}/\mu\text{m}$ )	1.1	3.1	2.8
Mobility ( $\text{cm}^2/\text{Vs}$ )	3.5	12.5	3.7
ON/OFF ratio	$10^6$	$10^7$	10
Subthreshold Swing (mV/dec)	150	95	0.6

The most important and significant aspect of in devices with 1T contacts is the improvement in the sub-threshold slope. This is quite strange to note because sub threshold slope is not affected by the types of contacts. Below is the equation of sub threshold slope

$$SS = \left(1 + \frac{C_s + C_{it}}{C_{ox}}\right) \frac{kT}{q} \ln 10$$

Since subthreshold slope is extracted in the deep subthreshold region,  $C_s$  which is the capacitance in  $\text{MoS}_2$  conducting channel is negligible.  $C_{ox}$  is the oxide capacitance which is same for the 1T contacted and 2H contacted device.

Now  $C_{it}$  is the capacitance from the interface trap density which is given by

$$C_{it} = qD_{it}$$

Here  $D_{it}$  is the interface traps density. Since 1T MoS<sub>2</sub> has a higher carrier concentration than 2H MoS<sub>2</sub>, the interface trap density is expected to be lower for 1T MoS<sub>2</sub>.

In order to answer why 1T contacts device has lower subthreshold slope, let us take a close look at the 1T contacts device configuration. Fig 7.13a is what we intend to do and the 1T conversion at the contacts is done with n-butyl lithium as explained earlier. However, since this transformation is a solution based process and lithium is a very small atom, it easily penetrates into the material which results in some conversion of the MoS<sub>2</sub> which is at the edges though it is covered by the PMMA resulting in the device to appear as shown in fig 7.13b.

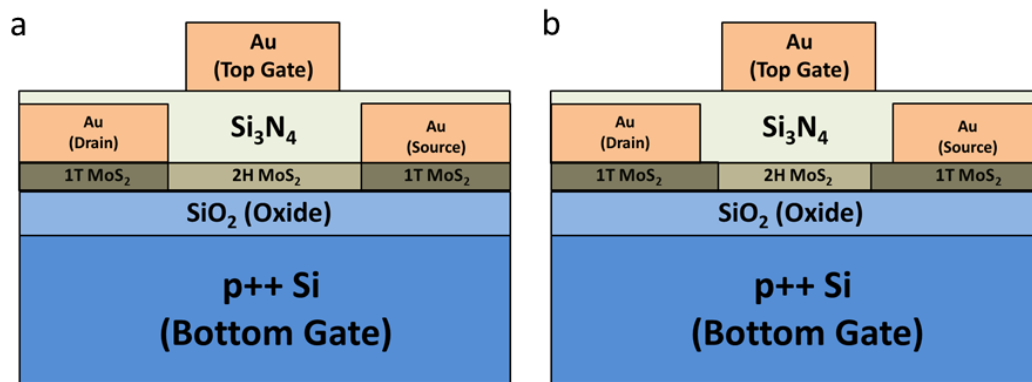


**Fig 7.13: Schematics of (a) intended structure and b) actual structure of top gated MoS<sub>2</sub> FET.**

The lower interface trap density in the 1T MoS<sub>2</sub> results in lower  $C_{it}$  and hence lower SS. It should also be noted that unlike metal on semiconductor contacts which actually contact the semiconductor from top, 1T contacts actually contact the semiconductor from the side. Side contacts have been proven to be very efficient for layered materials and have shown enhanced device properties compared to top contacts<sup>181-183</sup>.

## 7.5 Chapter summary

This chapter provided some in depth analysis of the 1T contacted devices. First, it described the process of estimating contact resistance through the fabrication of devices in the TLM structure. The contact resistance between gold and 2H phase MoS<sub>2</sub> was extracted as 1.1 K $\Omega$ - $\mu$ m and that between gold and 1T phase MoS<sub>2</sub> was obtained as 200  $\Omega$ - $\mu$ m which is record low contact resistance obtained till now. The schottky barrier height between gold and MoS<sub>2</sub> was measured to be ~1.1 eV and this value dropped to ~40 meV between gold and 1T MoS<sub>2</sub>. These results further established the enhancement of device performances with 1T contacts. Furthermore, top gated devices were fabricated with MoS<sub>2</sub>. For this a variety of dielectrics were explored and PECVD silicon nitride proved to be the best dielectric for MoS<sub>2</sub>. Top gated MoS<sub>2</sub> devices with 1T contacts gave a very low sub-threshold swing of ~90 mV/decade. Such low values were obtained for silicon MOSFETs after decades of optimization. The reason for improvement in the subthreshold swing values were discussed and the concept of side contacts versus top contacts was mentioned to be an additional reason for improved devices with 1T contacts.

## Chapter 8

### 8.1 Chemical Vapor deposition of MoS<sub>2</sub>

This chapter gives the details of my work published in APL Materials<sup>184</sup> in 2014 as an invited article. After establishing the process of fabrication of high performance devices with mechanically exfoliated MoS<sub>2</sub>, I moved on to chemically vapor deposited monolayer MoS<sub>2</sub> flakes and optimized the process to establish similarly enhanced performance. Fig. 8.1 shows the image of our furnace which we used for chemical vapor deposition of MoS<sub>2</sub>.



**Fig 8.1. Photograph of the furnace used for the growth of chemical vapor deposition of MoS<sub>2</sub>**

Growth of monolayer MoS<sub>2</sub> needed some optimized conditions for which several experiments were performed. Silicon substrates capped with 2850Å oxide layer are used for MoS<sub>2</sub> growth. These substrates were cut to appropriate sizes and were sonicated in HPLC Acetone (Sigma-Aldrich) and then rinsed with Isopropanol (Sigma-Aldrich). These substrates were introduced into the furnace where they are placed downwards on alumina crucible which contains 20mg of MoO<sub>3</sub> (Sigma-Aldrich) placed at the center of the furnace.

Close to the gas inlet of the furnace is placed another crucible with 100mg of Sulfur powder (Sigma-Aldrich). Growth is performed at atmospheric pressure while flowing a mixture of 95% Argon and 5% Hydrogen. Growth conditions are as follows:

- Heat the furnace to 550 °C at ramp rate of 20 °C/min. and hold for 5 minutes.
- Increase furnace temperature to 750 °C at ramp rate of 5 °C/min.
- Hold for 15 minutes at 750 °C for growth of MoS<sub>2</sub>.
- Cool down slowly to room temperature at 1 °C/min.

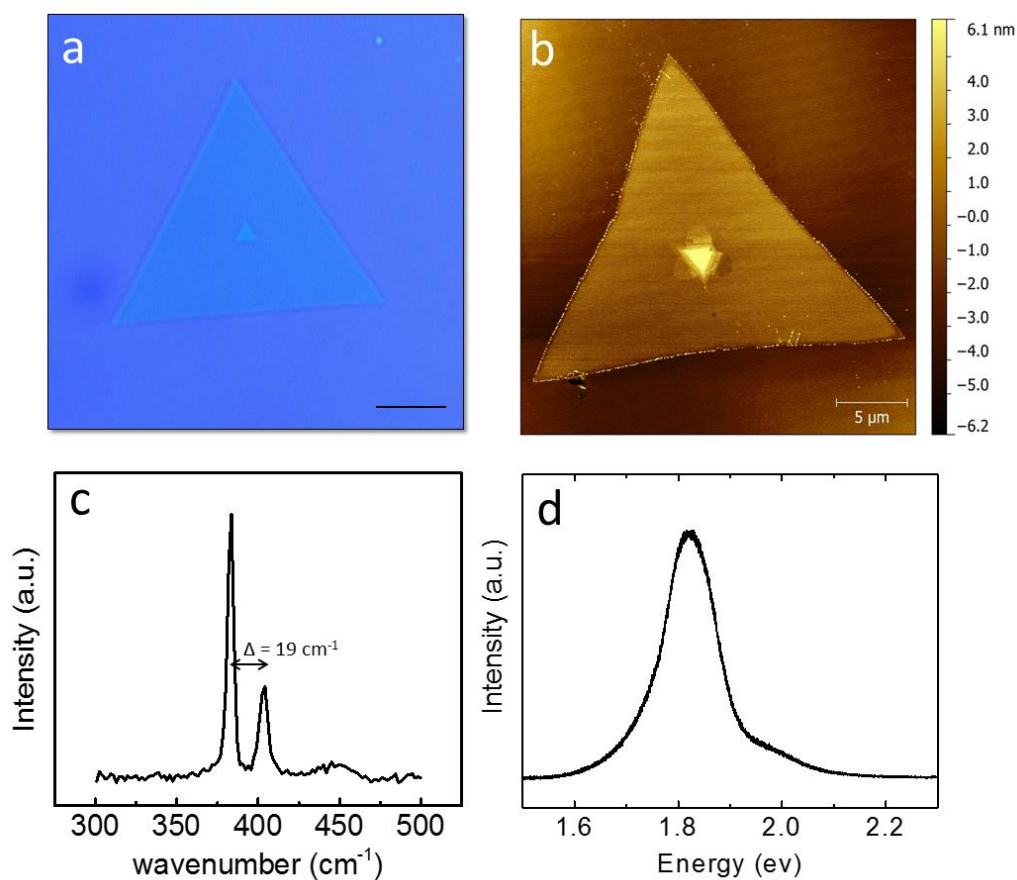


**Fig 8.2.** a) Optical microscope image of CVD monolayer MoS<sub>2</sub>. Scale bar = 5 μm b) AFM image of a monolayer CVD MoS<sub>2</sub> flake. c) Raman spectra of monolayer CVD MoS<sub>2</sub> having less than 20 cm<sup>-1</sup> difference in peak position, a sign of monolayer MoS<sub>2</sub>. d) Photoluminescence spectra of monolayer MoS<sub>2</sub> showing strong PL peak at 1.85 eV direct bandgap.

Figure 8.2 has some optical characterization data of the high quality monolayer flakes grown by this process. Devices are made on these high quality CVD monolayer MoS<sub>2</sub> flakes using Au-Ti contacts. Au or Au-Ti contacts did not differ significantly in case of CVD MoS<sub>2</sub> flakes. Fig. 8.3 show the device schematic, device photo, output and transfer characteristics of Au-Ti contacted devices.

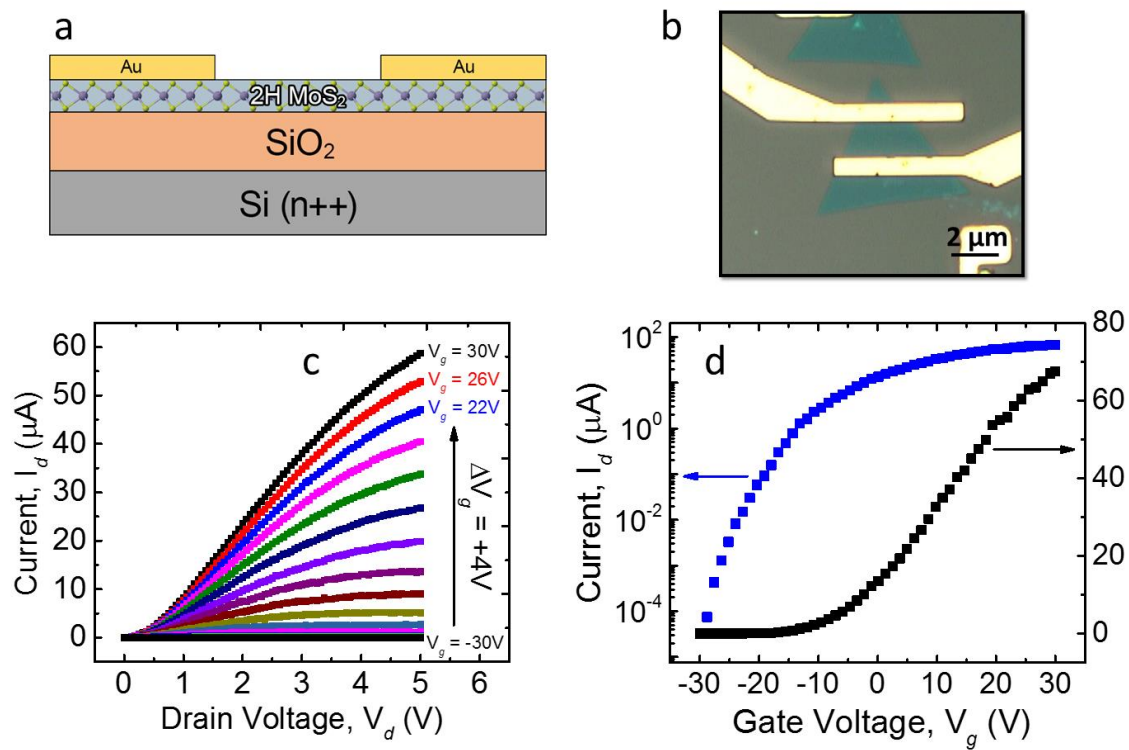


**Fig 8.3.** a) Device schematic of a generic CVD MoS<sub>2</sub> field effect transistor b) Optical microscope image of the device c) Output characteristics and d) Transfer characteristics of bottom gated MoS<sub>2</sub> field effect transistors.

Similar to mechanically exfoliated MoS<sub>2</sub> flake devices, CVD MoS<sub>2</sub> devices too exhibited schottky contacts with reasonably good saturation behavior as seen in output characteristics of fig 8.3c. The transfer characteristics too exhibited good field modulation with an ON/OFF ratio of 10<sup>7</sup>. The average mobility of 10 devices came to be around 24 cm<sup>2</sup>/Vs which is very good for CVD MoS<sub>2</sub> flakes.

Then I went on to make devices with 1T MoS<sub>2</sub> at the contacts. However the conditions of phase transformation were remarkably different for CVD MoS<sub>2</sub> compared to mechanically exfoliated MoS<sub>2</sub>. For complete PL quenching and emergence of 1T MoS<sub>2</sub> spectral peaks in Raman spectroscopy as shown in fig. 8.4 it took almost 48 hours of suspension of the samples in butyl-lithium. These conditions were optimized after several experiments of lithiation exposure in a systemized method.

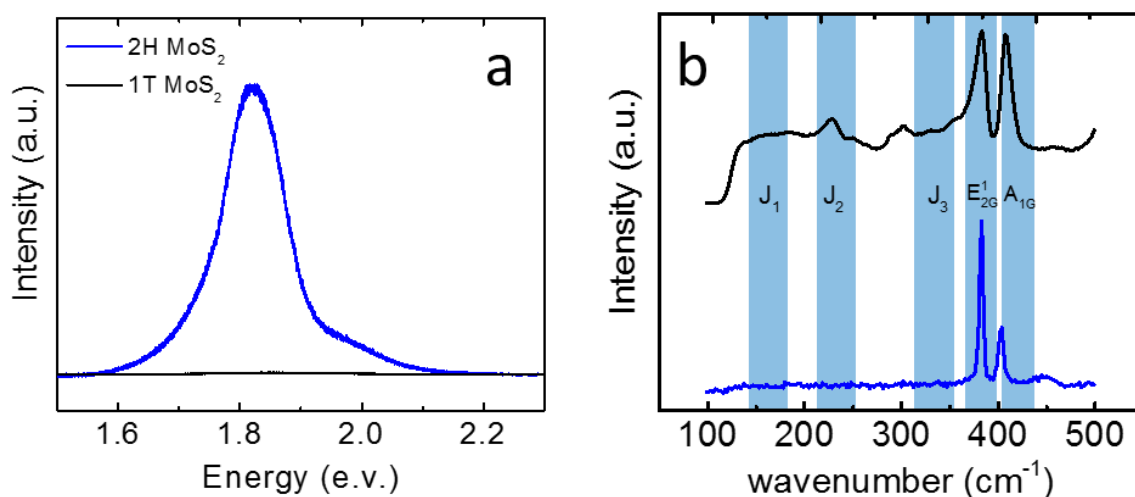


**Fig 8.4. a) Photoluminescence spectra of 1T and 2H MoS<sub>2</sub> showing complete quenching of PL in 1T MoS<sub>2</sub>. b) Raman spectra of 1T and 2H MoS<sub>2</sub> showing additional features in 1T MoS<sub>2</sub> spectra**

Device properties were significantly enhanced when 1T MoS<sub>2</sub> was used as the contacts for MoS<sub>2</sub> devices. Au-Ti was deposited on 1T MoS<sub>2</sub> converted regions, rest of the device fabrication process is similar to earlier. These devices showed much better performances than the generic devices (fig. 8.5). It can be observed that the devices show linear output characteristics representing ohmic contacts as compared to the skewed characteristics of the non 1T contacted devices representing schottky contacts. The saturation behavior is also comparatively better in these devices. The devices also exhibited faster turn on and stronger field modulation compared to the Au-2H contacted devices.

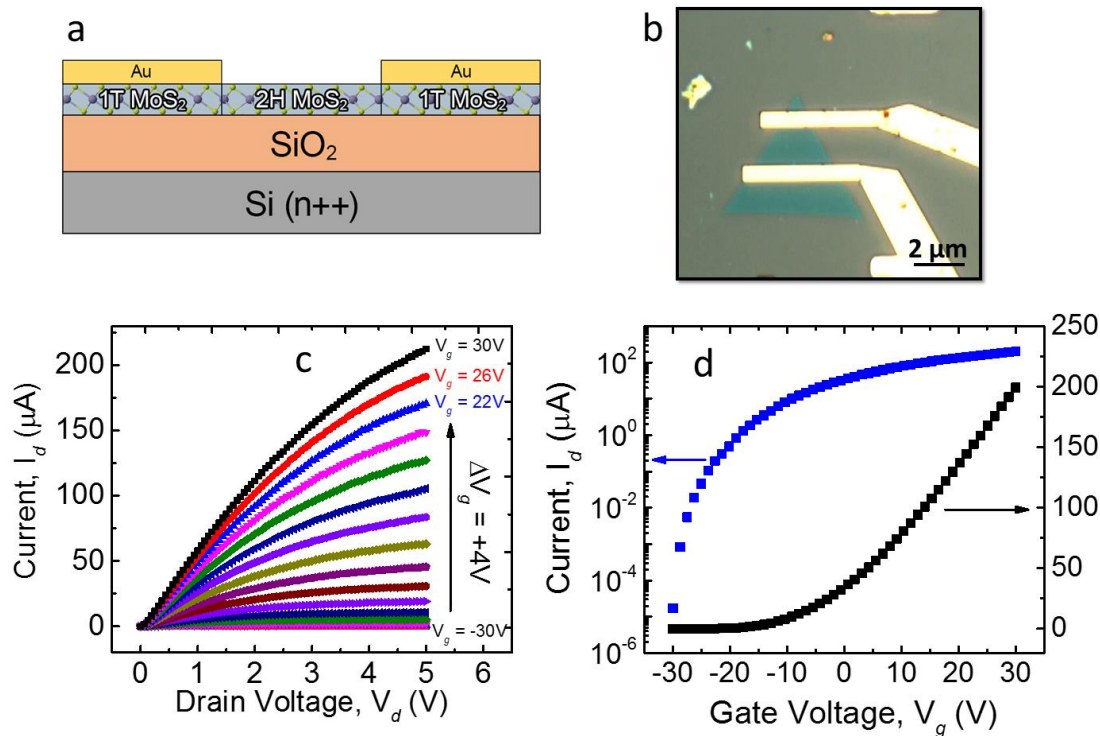


**Fig 8.5. a) Device schematic of a CVD MoS<sub>2</sub> field effect transistor with Au-1T contacts b) Optical microscope image of the device. c) Output characteristics and d) Transfer characteristics of bottom gated MoS<sub>2</sub> field effect transistors.**

Table 8.1 shows a comparison of device properties with both these types of contacts where we can see that the current levels and mobilities have increased by almost 3 times. Another important thing to note is the improvement in the sub-threshold swing. This could be because of the leakage of the 1T phase into the channel region causing a reduction in the density of states between the oxide and semiconductor and hence improving the device turn on feature.

**Table 8.1: Comparison of CVD MoS<sub>2</sub> field effect transistor**

<b>Table   Comparison of CVD MoS<sub>2</sub> bottom-gated devices</b>			
<b>Property</b>	<b>2H phase contacts</b>	<b>1T phase contacts</b>	<b>Ratio</b>
<b>ON currents (<math>\mu\text{A}/\mu\text{m}</math>)</b>	42	110	2.6
<b>Transconductance (<math>\mu\text{S}/\mu\text{m}</math>)</b>	2.2	4.8	2.2
<b>Mobility (<math>\text{cm}^2/\text{Vs}</math>)</b>	24	56	2.3
<b>Subthreshold Swing (V/dec)</b>	1.59	0.72	0.5

## 8.2 Devices with other Transition Metal Dichalcogenides

In order to prove the universality of this approach to other layered materials, I have chosen some prime transition metal dichalcogenides which exhibit hole conduction as well and performed the lithium intercalation based phase transformation on them. Tungsten disulfide (WS<sub>2</sub>), Molybdenum diselenide (MoSe<sub>2</sub>) and Tungsten diselenide (WSe<sub>2</sub>) have been chosen. These crystals were purchased in the form of powder from Alfa Aesar, and were exfoliated in similar process as for MoS<sub>2</sub> crystal. The following section describes the process of phase transformation and device results in detail for each TMD.

### 8.2.1 Tungsten disulfide (WS<sub>2</sub>)

Tungsten sulfide (Prod. No. 11829) was purchased from Alfa Aesar and mechanical exfoliation was performed to obtain flakes as shown in fig. 8.6. Flakes were characterized by Raman and phase transformation was performed over a period of 12 hours to obtain 1T phase WS<sub>2</sub> which was identified with the presence of additional peaks in the Raman spectra and photoluminescence which showed high quenching. These results are shown in fig 8.7. Single layer WS<sub>2</sub> has a band gap of  $\sim 2.0 \text{ eV}^{185}$ , represented by a strong peak in the photoluminescence spectra of fig. 8.7b which was substantially quenched after conversion to its 1T phase.

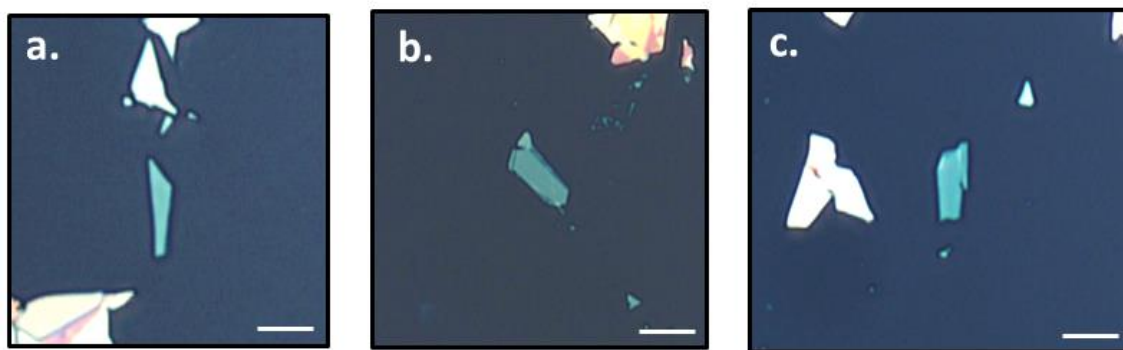


Fig 8.6. Mechanically exfoliated tungsten disulfide flakes with sizes over 5  $\mu\text{m}$ . Scale bar = 5  $\mu\text{m}$

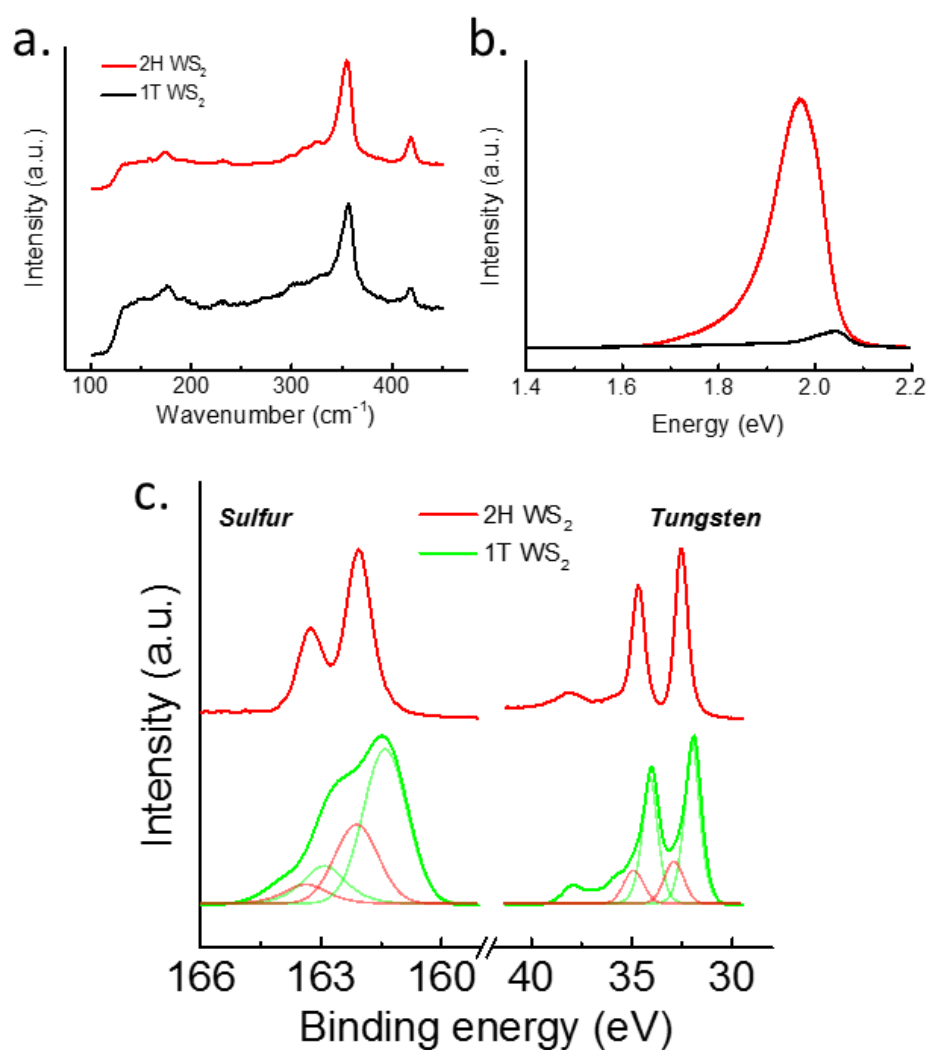
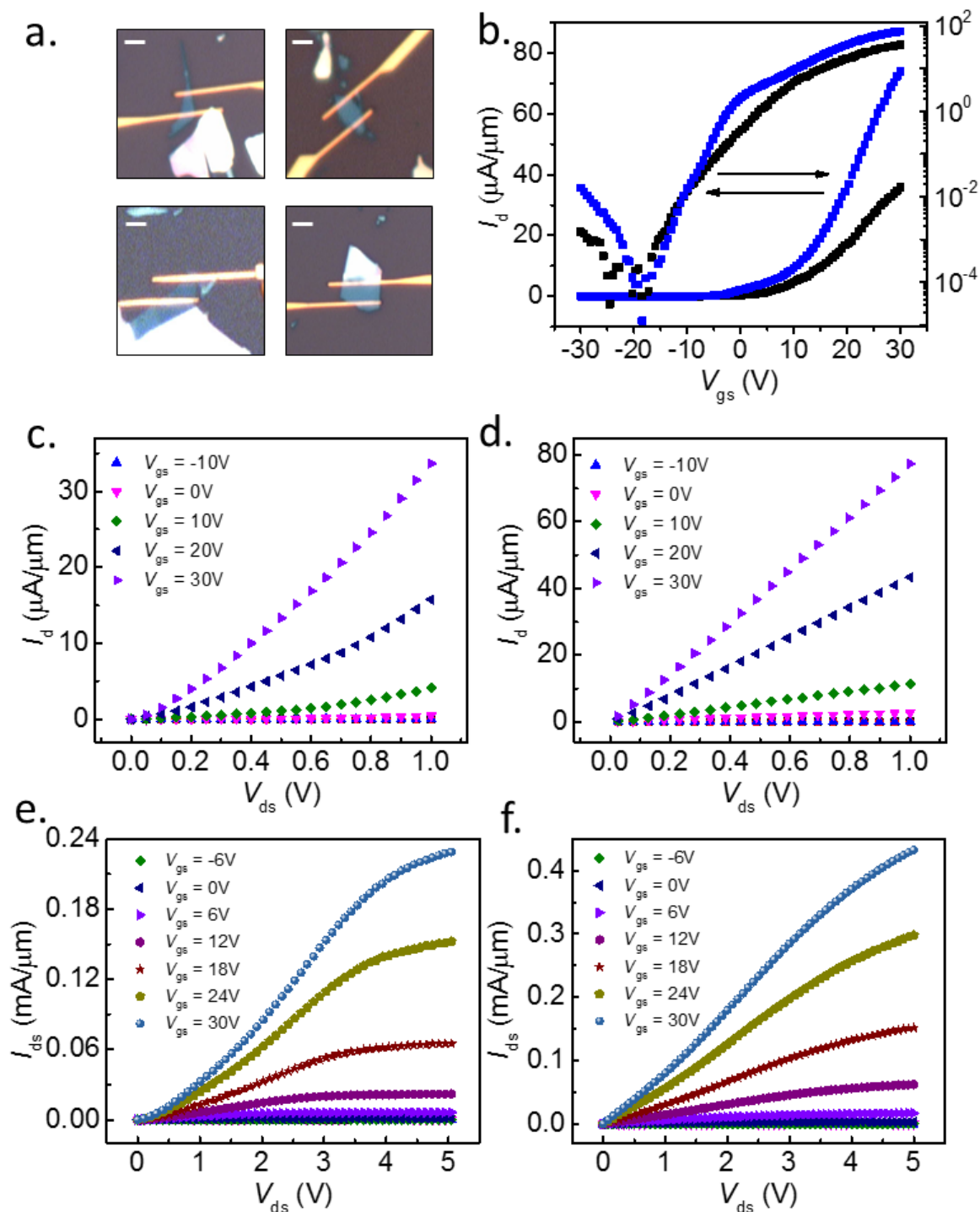


Fig 8.7. Raman (a) Photoluminescence (b) and XPS (c) spectra of 1T and 2H  $\text{WS}_2$

The XPS spectra in fig 8.7c shows the Tungsten and sulfur scans in 1T and 2H WS<sub>2</sub>. Similar to MoS<sub>2</sub>, 1T WS<sub>2</sub> has a higher concentration of charge carriers which causes a change in the Fermi level. This Fermi level can be detected by XPS and W from 1T WS<sub>2</sub> is detected at a lower binding energy. By deconvolution of the peaks in 1T WS<sub>2</sub> peaks, it was found that there is 60% 1T phase in highly lithiated WS<sub>2</sub>.

After optimization of the phase transformation process, I proceeded to the next step of making field effect transistors. I've used titanium of 5nm and gold of 50nm as the contacts and obtained working devices with ON currents in the range of 30  $\mu\text{A}/\mu\text{m}$  at  $V_d = 1\text{V}$  and a gate voltage of 30V on 100nm SiO<sub>2</sub> substrates. Similar to MoS<sub>2</sub>, the output curves were skewed representing a high schottky barrier between gold and WS<sub>2</sub>. An average mobility of 27  $\text{cm}^2/\text{Vs}$  was obtained after measuring around 5 devices. Unlike MoS<sub>2</sub>, there was also some hole current that was measured at negative gate voltages.

After phase transformation of the contacts, the devices showed tremendous improvement in their performances. The output characteristics were linear representing the suppression in the schottky barrier between gold and WS<sub>2</sub>. Currents increased by more than three-fold and averaged at 74  $\mu\text{A}/\mu\text{m}$  at  $V_d = 1\text{V}$  and a gate voltage of 30V. The average mobility was also higher at 64  $\text{cm}^2/\text{Vs}$ . An interesting thing to note was the improvement in hole current as well which was rather unexpected, this showed that 1T contacts allowed the tuning of Fermi level towards the valence band which allowed the injection of holes into the channel. Figure 8.8 shows the device photos, output characteristics showing skewed and linear characteristics, output curves showing saturation and transfer characteristics showing faster switching and higher current levels in 1T contacted devices.



**Fig 8.8.** Device properties of WS<sub>2</sub> field effect transistors. a) Some typical device images, scale bar = 5 μm b) Transfer characteristics of WS<sub>2</sub> field effect transistors with (blue) and without 1T contacts (black) c) Output characteristics showing schottky contacts for Au-2H WS<sub>2</sub> devices d) Output characteristics showing ohmic contacts for Au-1T WS<sub>2</sub> devices e, f) Output characteristics showing good saturation for both types of devices

### 8.2.2 Molybdenum diselenide (MoSe<sub>2</sub>)

Molybdenum diselenide (Prod. No. 13112) was purchased from Alfa Aesar and mechanical exfoliation was performed to obtain flakes as shown in fig. 8.9. Flakes were characterized by Raman and phase transformation was performed for 24 hours to obtain 1T phase WS<sub>2</sub> which was identified with the presence of additional peaks in the Raman spectra and photoluminescence which showed high quenching. These results are shown in fig 8.10. Single layer MoSe<sub>2</sub> has a band gap of  $\sim 1.6$  eV<sup>186,187</sup>, represented by a strong peak in the photoluminescence spectra of fig. 8.10b which was completely quenched after conversion to its 1T phase.

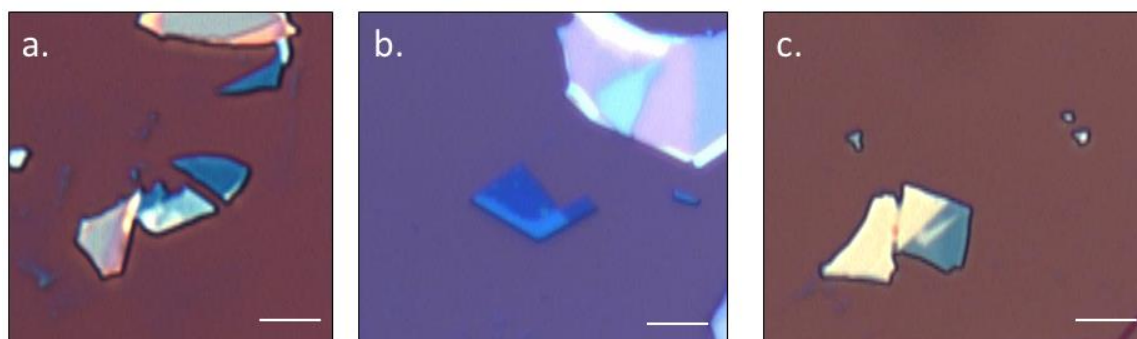


**Fig 8.9. Mechanically exfoliated MoSe<sub>2</sub> flakes with sizes over 5  $\mu$ m. Scale bar = 5  $\mu$ m**

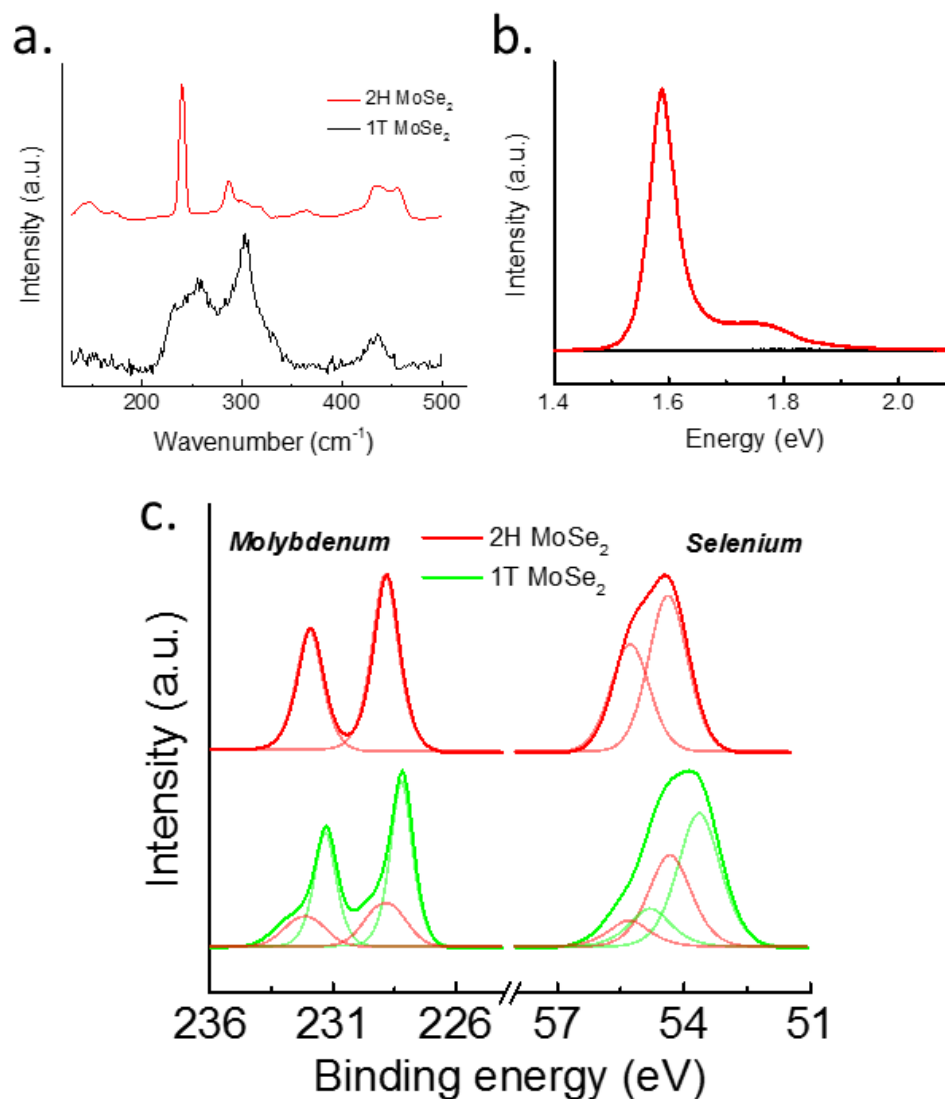


**Fig 8.10. Raman (a) Photoluminescence (b) and XPS (c) spectra of 1T and 2H MoSe<sub>2</sub>**

The XPS spectra in fig 63c shows the Molybdenum and selenium scans in 1T and 2H MoSe<sub>2</sub>. 1T MoSe<sub>2</sub> has a higher concentration of charge carriers which causes a change in the Fermi level. This change can be detected by XPS and Mo from 1T MoS<sub>2</sub> is detected at a lower binding energy. By deconvolution of the peaks in 1T WS<sub>2</sub> peaks, it was found that there is 70% 1T phase in highly lithiated MoS<sub>2</sub>.

After optimization of the phase transformation process in MoSe<sub>2</sub>, I proceeded to the next step of making field effect transistors. I've used titanium of 5nm and gold of 50nm as the contacts and obtained working devices with ON currents in the range of 48  $\mu\text{A}/\mu\text{m}$  at  $V_d = 1\text{V}$  and a gate voltage of 30V on 100nm SiO<sub>2</sub> substrates. The output curves were not as skewed representing a decently low barrier between gold and MoSe<sub>2</sub>. An average mobility of 42  $\text{cm}^2/\text{Vs}$  was obtained after measuring around 5 devices. Similar to WS<sub>2</sub>, there was some hole current that was measured at negative gate voltages.

After phase transformation of the contacts, the devices showed improved performances. The output characteristics were linear representing the suppression in the schottky barrier between gold and MoSe<sub>2</sub>. Currents increased by almost two times and averaged at 95  $\mu\text{A}/\mu\text{m}$  at  $V_d = 1\text{V}$  and a gate voltage of 30V. The average mobility was also higher at 85  $\text{cm}^2/\text{Vs}$ . MoSe<sub>2</sub> devices exhibited a very good saturation behavior unlike WS<sub>2</sub> and the overall current levels and mobilities were higher compared to all the other TMD materials studied in this work. Though the improvement in electron current and mobility were not substantial, there was a good amount of improvement in the hole conduction. This could mean that though gold was a decent electron injection material into the semiconducting MoSe<sub>2</sub>, it wasn't as good in injecting holes which resulted in a low hole current. However upon conversion of the contacts to 1T phase, hole injection was rather easier and hence we see a good increase in the hole current. Figure 8.11 shows the device photos, output characteristics showing skewed and linear characteristics, output curves showing saturation and transfer characteristics showing faster switching and higher current levels in 1T contacted devices.

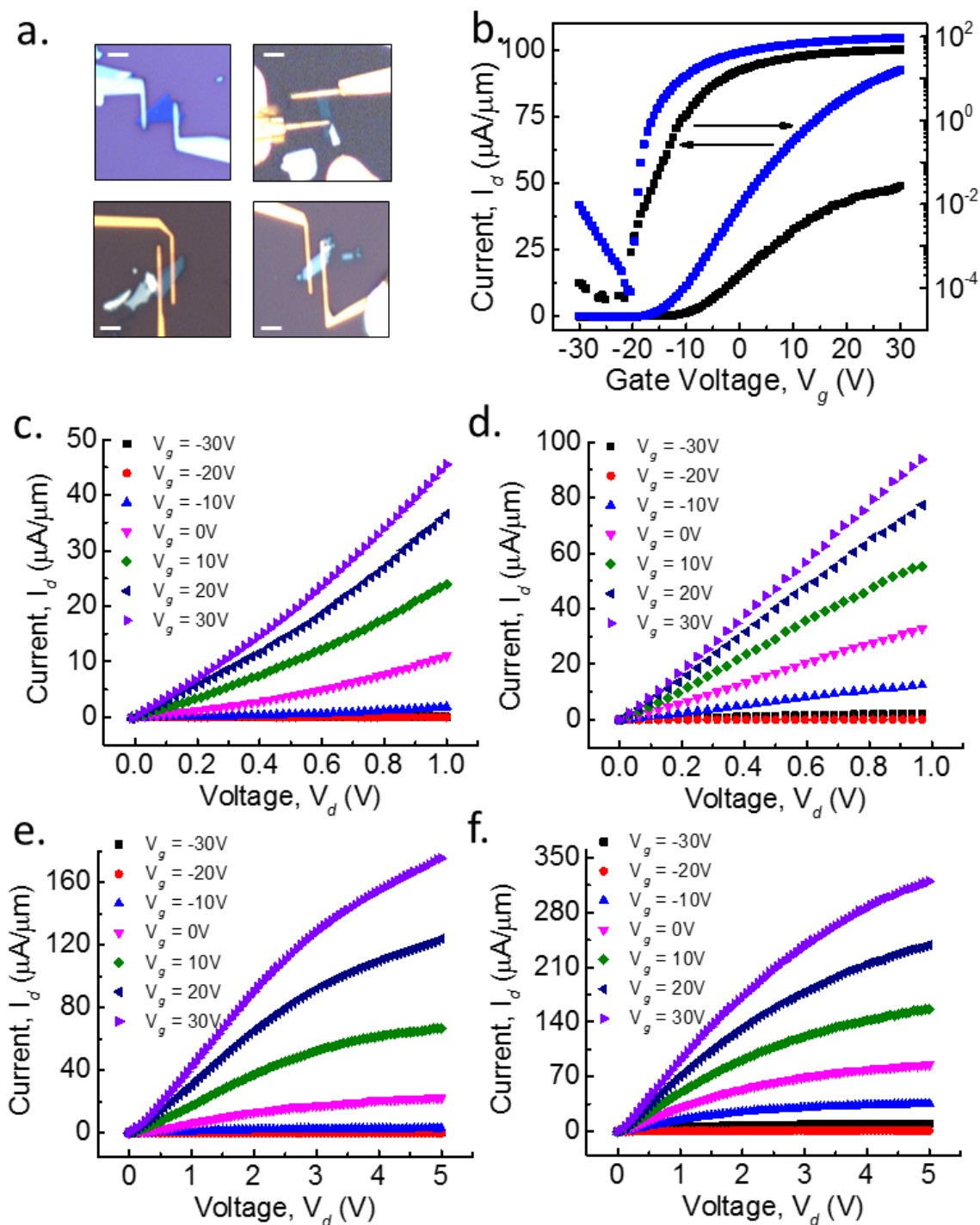


**Fig 8.11.** Device properties of MoSe<sub>2</sub> field effect transistors. a) Some typical device images, scale bar = 5 μm b) Transfer characteristics of MoSe<sub>2</sub> field effect transistors with (blue) and without 1T contacts (black) c) Output characteristics showing schottky contacts for Au-2H MoSe<sub>2</sub> devices d) Output characteristics showing ohmic contacts for Au-1T MoSe<sub>2</sub> devices e, f) Output characteristics showing good saturation for both types of devices

### 8.2.3 Tungsten diselenide (WSe<sub>2</sub>)

Tungsten diselenide (Prod. No. 13084) was purchased from Alfa Aesar and mechanical exfoliation was performed to obtain flakes as shown in fig. 8.12. Flakes were characterized by Raman and phase transformation was performed for 48 hours to obtain 1T phase WS<sub>2</sub> which was identified with the presence of additional peaks in the Raman spectra and photoluminescence which showed high quenching. These results are shown in fig 8.13. Single layer WSe<sub>2</sub> has a band gap of  $\sim 1.7$  eV<sup>188,189</sup>, represented by a strong peak in the photoluminescence spectra of fig. 8.13b which was highly quenched after conversion to its 1T phase.

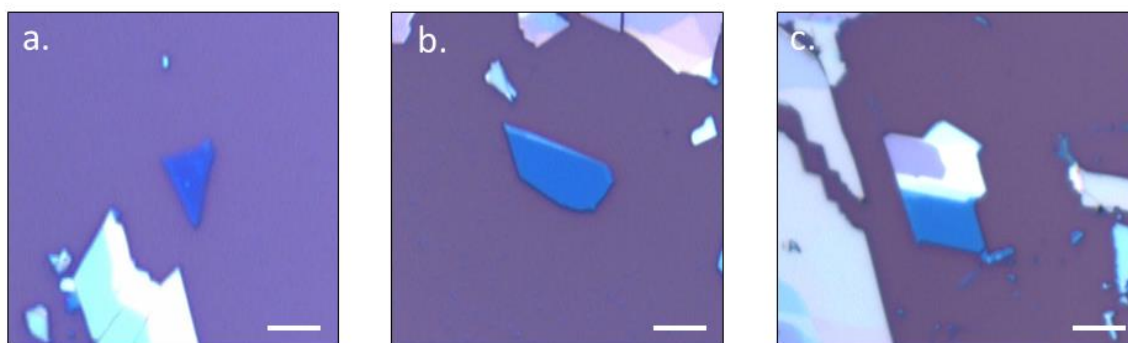


**Fig 8.12. Mechanically exfoliated WSe<sub>2</sub> flakes with sizes over 5  $\mu$ m. Scale bar = 5  $\mu$ m**

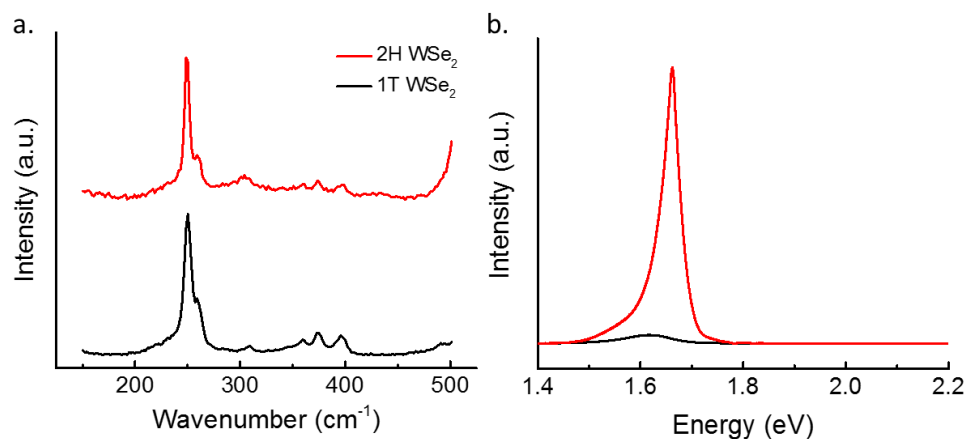


**Fig 8.13. Raman and Photoluminescence spectra of 1T and 2H WSe<sub>2</sub> flakes**

After optimization of the phase transformation process in WSe<sub>2</sub>, I proceeded to the next step of making field effect transistors. I've used titanium of 5nm and gold of 50nm as the contacts and obtained working devices with ON currents in the range of 30  $\mu\text{A}/\mu\text{m}$  at  $V_d = 1\text{V}$  and a gate voltage of 30V on 100nm SiO<sub>2</sub> substrates. The output curves were skewed representing a high barrier between gold and WSe<sub>2</sub>. An average mobility of 45  $\text{cm}^2/\text{Vs}$  was obtained after measuring around 5 devices. Similar to WS<sub>2</sub>, there was some hole current that was measured at negative gate voltages.

After phase transformation of the contacts, the devices showed improved performances. The output characteristics were linear representing the suppression in the schottky barrier between gold and WSe<sub>2</sub>. Currents increased by almost two times and averaged at 59  $\mu\text{A}/\mu\text{m}$  at  $V_d = 1\text{V}$  and a gate voltage of 30V. The average mobility was also higher at 78  $\text{cm}^2/\text{Vs}$ . WSe<sub>2</sub> devices exhibited a good saturation behavior like MoSe<sub>2</sub>. There was a good amount hole current measurable in WSe<sub>2</sub> device prior to phase conversion of the contacts unlike the other TMD semiconductors. However upon phase conversion this current increased much more and showed faster switching in hole current as well. Figure 8.14 shows the device photos, output characteristics showing skewed and linear characteristics, output curves showing saturation and transfer characteristics showing faster switching and higher current levels in 1T contacted devices

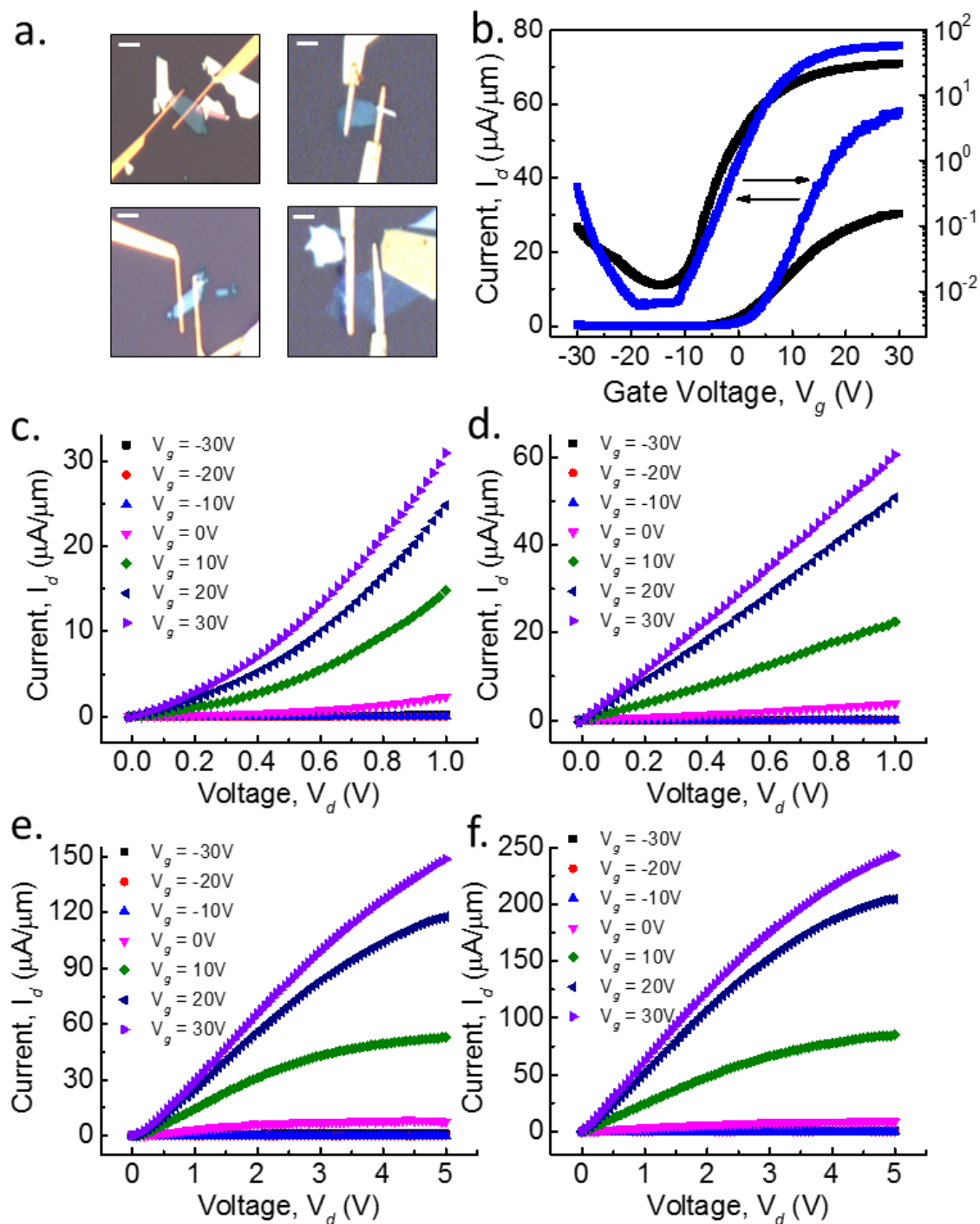


**Fig 8.14.** Device properties of  $\text{WSe}_2$  field effect transistors. a) Some typical device images, scale bar =  $5 \mu\text{m}$  b) Transfer characteristics of  $\text{WSe}_2$  field effect transistors with (blue) and without 1T contacts (black) c) Output characteristics showing schottky contacts for Au-2H  $\text{WSe}_2$  devices d) Output characteristics showing ohmic contacts for Au-1T  $\text{WSe}_2$  devices e, f) Output characteristics showing good saturation for both types of devices

The improvement in electron currents and mobilities in all the above mentioned TMDs proves that 1T phase contacts provide efficient injection of electrons into the channel. A summary of the ON currents and mobility values is given in table 8.2. We have done some Kelvin probe measurements on 1T MoS<sub>2</sub> and found the work function to be very close to the electron affinity value of 2H MoS<sub>2</sub>, this provides a validity for the enhanced performance of the devices. It has also been mentioned in literature about the presence of high mid gap states close to the conduction band in MoS<sub>2</sub> which cause strong Fermi level pinning<sup>155,190</sup>. Due to this it is very difficult to inject holes into MoS<sub>2</sub>. However the Fermi level pinning is not so strong in other TMDs which was proven by device results that some finite amount of hole current can be achieved with regular Au-Ti contacted devices. This hole current was further enhanced when 1T contacts were utilized which meant further elimination of the Fermi level pinning effect.

**Table 8.2: Comparison of FET performances of Au-2H and Au-1T contacts of all TMDs**

Property	Contacts	MoS <sub>2</sub>	WS <sub>2</sub>	MoSe <sub>2</sub>	WSe <sub>2</sub>
<b>ON current (<math>\mu\text{A}/\mu\text{m}</math>)</b> $V_{ds} = 1\text{V}, V_{gs} = 30\text{V}$	2H	28	32	48	30
	1T	85	74	95	59
<b>Mobility (<math>\text{cm}^2/\text{Vs}</math>)</b>	2H	25	27	42	45
	1T	56	64	85	78

### 8.3 Photocurrent measurement in monolayer CVD MoS<sub>2</sub>

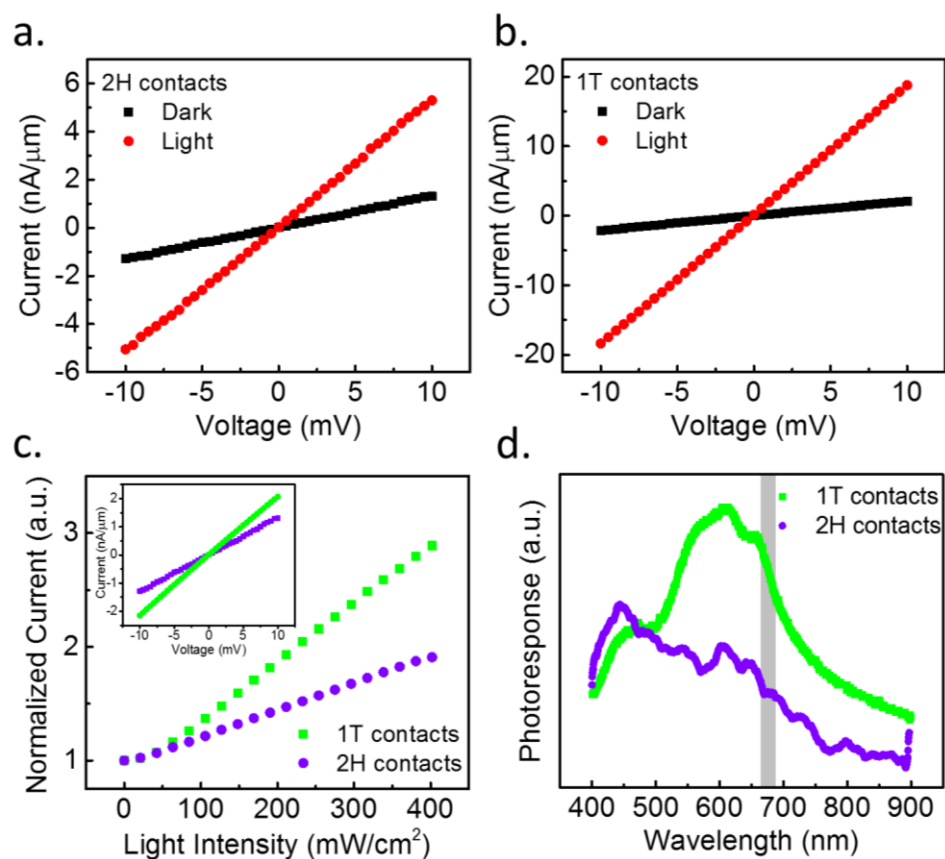
Besides electronic properties, the contact condition also affects the optoelectronic properties significantly. To demonstrate the differences between Au-2H contacts and Au-1T contacts, MoS<sub>2</sub>-based photo-detectors with both these types of contacts were fabricated and studied and the results are shown in Figure 8.15.

Figure 8.15a and b shows the dark current and photo-response IV curves coming from an Au contacted and 1T-contacted MoS<sub>2</sub> photo-detector respectively, with a 532 nm 150 mW/cm<sup>2</sup> illumination source. It is clear that the device with 1T contacts has a much stronger photo-response. With a 10 mV bias voltage, the photocurrent in the 1T-contacted devices is about 20 nA, whereas the one in the 2H-contacted device is about 5 nA. i.e. the photo-response is 4-fold stronger in device with 1T contact. This is because the 1T phased MoS<sub>2</sub> is metallic and, with electrodes, it can easily form Ohmic contact which can significantly reduce the contact resistance and avoid the contact barrier that limits the free transportation of charge carriers so that the recombination rate between electrons and holes can significantly decrease and yield a stronger photocurrent. The photo-responsivity of the 1T device with 10 mV bias is 2.53 A/W and the one of the 2H device is 0.70 A/W.

On the other hand, 2H MoS<sub>2</sub> tends to form Schottky contact with metal electrodes. The Schottky contact can always barrier one kind of charge carriers, either electron or hole, so that recombination happens at the contact area, which limits the over-all external quantum efficiency. Figure 8.15c shows the photo-current as a function of illumination intensity. It can be found that in both cases, the photo-currents nearly obey a linear response. However, the slope of the 1T device is larger, which also proves that the 1T device can utilize the photo-generated charge carriers more effectively due to the Ohmic contact. But the benefit of Schottky contact is that it can minimize the dark current effectively, since charge carriers cannot pass the barrier freely unless they are excited with an energy that is high enough. So in the dark, the current cannot be generated in MoS<sub>2</sub> with Schottky barriers on both sides. On the other hand, Ohmic contact allows charge carriers move freely, and even in the dark, it is still possible to inject electrons and holes from metal

electrodes into MoS<sub>2</sub> which results in a larger dark current. The inset of Figure 8.15c shows the dark currents from the 1T device and the 2H device, and it can be found that the dark current in 1T device is about 2 times larger.

Figure 8.15d shows the photo-response spectrum from both devices. Again, the one with 1T contacts yields a stronger response in the range from 500 nm to 700 nm, which corresponding to the inter-band transition in MoS<sub>2</sub>. i.e. the photo-generated charge carriers more fully used in 1T device.



**Fig 8.15. Optoelectronic characterization of 1T contacted CVD MoS<sub>2</sub> devices. a, b) Photo response of Au and 1T phase contacted CVD MoS<sub>2</sub> flake respectively showing higher photocurrent in the latter case. c) Photocurrent variation with light intensity for Au contacted and 1T contacted CVD MoS<sub>2</sub> flake showing higher response in 1T contact device, inset shows the dark current for both the devices. d) Photo-response spectrum for 1T contacted and Au contacted CVD MoS<sub>2</sub> devices.**

## 8.4 Chapter summary

This chapter discussed the application of the 1T contacts technique to materials other than mechanically exfoliated MoS<sub>2</sub>. For this purpose, chemically vapor deposited MoS<sub>2</sub> was chosen. Synthesis process of CVD MoS<sub>2</sub> was described and its characterization results were shown. Similar enhanced performances were shown for 1T contacted CVD monolayer MoS<sub>2</sub> devices and all the relevant results were presented. Other members of the TMD family such as WS<sub>2</sub>, MoSe<sub>2</sub> and WSe<sub>2</sub> were then introduced and mechanical exfoliation to obtain few layer flakes of these materials were discussed. Phase transformation and PL quenching results were shown. Device characteristics of these materials were presented and enhanced performances with 1T contacts for all these semiconductors were shown. Additionally, optoelectronic measurements were discussed for monolayer MoS<sub>2</sub> devices which showed enhanced photo-conduction and photo-responses for 1T contacts.

## Chapter 9

### Future work and Conclusions

#### 9.1 Future Work

1T phase contacts are definitely the best contacts that have been realized for TMD semiconductors. There is scope for further improvement to obtain 100% transmission, that is, no scattering of charge carriers at the contacts can be established. Such kinds of devices will help in realizing interesting devices and understanding physics concepts at a deep level. Below are some examples:

**9.1.1 Spintronics:** In addition to carrying a charge, electron also carries a specific spin direction and a magnetic moment. In spintronics or spin electronics, these properties are exploited in devices which have ferromagnetic contacts; depending on the orientation of the magnetic fields, the resistance in the device could either be maximum or minimum<sup>191-195</sup>. Monolayer MoS<sub>2</sub> has inversion symmetry breaking and a large spin-orbit coupling which results in a high spin-orbit splitting. This results in suppression of spin relaxation and increase in spin lifetimes<sup>151,196,197</sup>. These properties show promise for MoS<sub>2</sub> to be used in spintronic devices. However, in order to realize spin behavior in MoS<sub>2</sub> or any other TMD, the quality of contacts play a major role since they primarily control the spin injection and spin transport. Therefore, ferromagnetic materials deposited on optimized 1T phase can help in realization of efficient spintronic devices in MoS<sub>2</sub>.

**9.1.2 Probing mid-gap states:** It has been proposed in literature that the reason for strong Fermi-level pinning in MoS<sub>2</sub> is due to the presence of a high number of mid-gap states in MoS<sub>2</sub><sup>198</sup>. These mid gap states can be probed through carefully done photocurrent measurements as shown earlier in fig 8.15d. The presence of mid-gap states would be

evident through a rise in the photocurrent at a particular energy level. A temperature dependent measurement of the photocurrent spectra and a control on the quality of contacts would shed some light onto the nature of these mid-gap states.

**9.1.3 Mono-Multi layer interface:** Through mechanical exfoliation or sometimes chemical vapor deposition, it is possible to obtain a structure which has a monolayer at one end and a multilayer at the other as shown in fig 9.1. Studying devices with the channel having this interface would reveal some interesting physics. Monolayer  $\text{MoS}_2$  is a direct bandgap semiconductor whereas multilayer  $\text{MoS}_2$  is an indirect bandgap semiconductor. Some preliminary results have shown higher current levels for these devices compared to those of monolayer or bilayer devices. Some more involved measurements such as low temperature electrical measurements and some photocurrent mapping spectra would provide some more info on how carriers are transported at these junctions and how they can be utilized for applications involving electronics and optoelectronic devices.

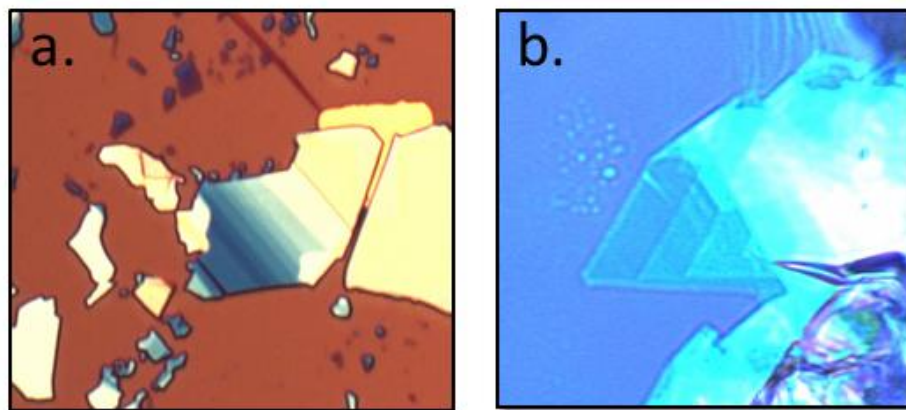


**Fig 9.1. Interfaces of mono-multilayers of  $\text{MoS}_2$  on a) mechanically exfoliated and b) Chemically vapor deposited  $\text{MoS}_2$**

**9.1.4 All 2D Heterojunction solar cells:** Layered TMD materials have saturated atoms and no dangling bonds on their surfaces. Due to this, van der Waals heterostructures of a

plethora of combinations of these TMDs can be realized<sup>199-203</sup>. Moreover due to their bandgaps been different, combining them in the right order to align their HOMO and LUMO levels and choosing the right metals would allow in extracting holes and electrons efficiently upon generation of the electron hole pair at the junctions<sup>204-208</sup>. Some examples of such heterojunction solar cells are given in fig. 9.2.

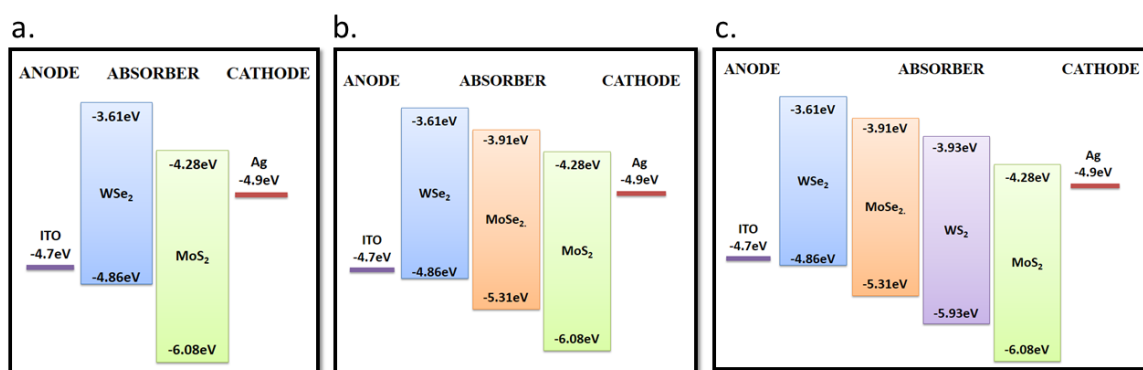


**Fig. 9.2. All 2D heterojunction solar cells with TMD semiconductors**

Along with the above mentioned projects, some additional projects can be planned to make the most of these optimized 1T contacts by suspending MoS<sub>2</sub> in high quality hexagonal boron nitride flakes similar to graphene<sup>209,210</sup> and study interesting concepts such as quantum oscillations and quantum hall effect for which the contacts should be nearly free of scattering. Also possible to realize is the efficiency of these layered materials as hydrogen evolution catalysts by probing them in a number of different ways. Devices can be made where only the edge or the center of these monolayer flakes can be exposed and their catalytic activity can be studied. A comparison of a variety of layered materials can be made and they can be structurally characterized as to where the highest activity comes from. Photocurrent mapping is another strong measurement technique which gives important information of the contact conditions. By measuring the region of a device where

the maximum photocurrent is generated, an estimation of the contact quality as well as the schottky barrier height can be made. A schottky junction would have maximum photocurrent generated at the contacts whereas an ohmic contact would have photocurrent generation uniformly over the device with a maximum at the center of the channel.

These above ideas can be planned in an organized manner to carve the path for the research of another doctoral student or a post-doctoral researcher.

## **9.2 Conclusions**

A relatively new material, molybdenum disulfide,  $\text{MoS}_2$ , has been introduced as a promising candidate for future electronics owing to its excellent properties like high ON currents, mobilities and excellent switching rate evident from the low sub-threshold swings. A major issue of the inability to realize efficient contacts has been discussed and an innovative solution has been proposed. Phase engineering has been an active area of research in materials science field and has been studied since a long time on a variety of materials. Different phases of  $\text{MoS}_2$  have been studied through phase transformation and a metallic 1T phase of the naturally occurring semiconducting 2H phase has been obtained. 1T phase  $\text{MoS}_2$  was characterized through Raman spectroscopy where additional spectral peaks have been observed and was quantized through X-ray photoelectron spectroscopy where the 1T phase was identified due to the change in Fermi level of Molybdenum atom. Electrical properties of 1T  $\text{MoS}_2$  have been explored and was observed that the charge carrier concentration was very high due to which field modulation was not possible. Fine patterning of 1T phase on sheets of 2H  $\text{MoS}_2$  flakes was demonstrated using PMMA mask which was patterned through e-beam lithography. Images from fluorescence microscopy, scanning electron microscope and high resolution transmission electron microscope were

shown to prove the existence of these two phases coherently on the flake with atomically thin interface. Bottom gated MoS<sub>2</sub> field effect transistors were fabricated with these 1T phase contacts and enhanced performances were obtained compared to the performance of devices without the 1T phase contacts. It was shown that these contacts are very effective with record low contact resistance values of ~200 Ωμm at zero gate bias. These low contact resistances have led to very high drive currents (85 μAμm<sup>-1</sup>), high mobility values (55 cm<sup>2</sup>/Vs), low subthreshold swing values (95 mV/dec.) and high on/off ratios exceeding 10<sup>7</sup>. We have also shown that these 1T phase contacts are independent of the type of metal deposited on them by demonstrating working transistors with contacts made of a high work function metal, Palladium, and a low work function metal, Calcium, both of which are not good to fabricate working MoS<sub>2</sub> transistors. We have also fabricated top gated transistors by using a variety of dielectrics and concluded that PECVD silicon nitride (Si<sub>3</sub>N<sub>4</sub>) works best for MoS<sub>2</sub> due to its oxygen-free composition and low temperature deposition compared to the other dielectrics. Silicon nitride works very well for Au-2H contacted as well as Au-1T contacted devices. We have established this method for CVD monolayer MoS<sub>2</sub> and other TMD materials such as MoSe<sub>2</sub>, WS<sub>2</sub> and WSe<sub>2</sub> and have hence proved the universality of this method for its employment to all layered transition metal dichalcogenides semiconductors. Finally we have proven that 1T contacted devices not only enhance the electrical properties of devices but also opto-electrical properties where we have fabricated photo-detectors with CVD MoS<sub>2</sub> and showed enhanced photo-conduction and photo-responses.

## References

- <sup>1</sup> Dennard, R. H., Gaensslen, F. H., Rideout, V. L., Bassous, E. and LeBlanc, A. R., IEEE J. Solid-State Circuits 9, 256 (1974)
- <sup>2</sup> Mistry, K., Allen, C. ; Auth, C. ; Beattie, B. ; Bergstrom, D. ; Bost, M. ; Brazier, M. ; Buehler, M. ; Cappellani, A. ; Chau, R. ; Choi, C.-H. ; Ding, G. ; Fischer, K. ; Ghani, T. ; Grover, R. ; Han, W. ; Hanken, D. ; Hattendorf, M. ; He, J. ; Hicks, J. ; Huessner, R. ; Ingerly, D. ; Jain, P. ; James, R. ; Jong, L. ; Joshi, S. ; Kenyon, C. ; Kuhn, K. ; Lee, K. ; Liu, H. ; Maiz, J. ; McIntyre, B. ; Moon, P. ; Neiryneck, J. ; Pae, S. ; Parker, C. ; Parsons, D. ; Prasad, C. ; Pipes, L. ; Prince, M. ; Ranade, P. ; Reynolds, T. ; Sandford, J. ; Shifren, L. ; Sebastian, J. ; Seiple, J. ; Simon, D. ; Sivakumar, S. ; Smith, P. ; Thomas, C. ; Troeger, T. ; Vandervoorn, P. ; Williams, S. and Zawadzki, IEEE Int. Electron Dev. Meeting 247 (2007)
- <sup>3</sup> Cartwright, J. Intel enters the third dimension. Nature News <http://dx.doi.org/10.1038/news.2011.274> (6 May 2011)
- <sup>4</sup> Moore, G. E., Electron. Mag. 38, 114 (1965)
- <sup>5</sup> International Technology Roadmap for Semiconductors (ITRS, 2012); <http://www.itrs.net>
- <sup>6</sup> C.-H. Jan, U. Bhattacharya, R. Brain, S. - J. Choi, G. Curello, G. Gupta, W. Hafez, M. Jang, M. Kang, K. Komeyli, T. Leo, N. Nidhi, L. Pan, J. Park, K. Phoa, A. Rahman, C. Staus, H. Tashiro, C. Tsai, P. Vandervoorn, L. Yang, J.-Y. Yeh and P. Bai, Int. Electron Dev. Meeting Tech. Digest 44 (2012).
- <sup>7</sup> Yu, B. et al. Proc. Int. Semiconductor Dev. Res. Symp. 623–626 (Engineering Academic Outreach, 1997).
- <sup>8</sup> Novoselov, K. S., Jiang, D., Schedin, F., Booth, T. J., Khotkevich, V. V., Morozov, S. V., and Geim A.K., Proc. Natl Acad. Sci. USA, 102, 10451 (2005)
- <sup>9</sup> Mattheis, L. F., Phys. Rev. B, 8, 3719 (1973)
- <sup>10</sup> Wilson, J. A., Yoffe, A. D., Adv. Phys.18, 193 (1969)
- <sup>11</sup> Wang, Q. H., Kalantar-Zadeh, K., Kis, A., Coleman, J. N., Strano, M. S., Nature Nanotech. 7, 699 (2012)

- <sup>12</sup> Eda, G., Yamaguchi, H., Voiry, D., Fujita, T., Chen, M., and Chhowalla, M., *Nano. Lett.*, 11 (12), 5111 (2011)
- <sup>13</sup> Eda, G., Fujita, T., Yamaguchi, H., Voiry, D., Chen, M. W. & Chhowalla, M., *ACS Nano* 6, 7311 (2012)
- <sup>14</sup> Chhowalla, M., Shin, H. S., Eda, G., Li, L.-J., Loh, K. P., and Zhang, H., *Nat. Chem.* 5, 263 (2013)
- <sup>15</sup> Voiry, D., Yamaguchi, H., Li, J., Silva, R., Alves, D.C.B., Fujita, T., Chen, M., Asefa, T., Shenoy, V. B., Eda, G. & Chhowalla, M.: *Nat. Mat.* 12, 850 (2013)
- <sup>16</sup> Osada, M., Sasaki, T., *Adv. Mater.* 24, 210 (2012)
- <sup>17</sup> Zhang, H., Liu, C.-X., Qi, X.-L., Dai, X., Fang, Z., Zhang, S.-C., *Nature Phys.* 5, 438 (2009)
- <sup>18</sup> Aufray, B., Kara, A., Vizzini, S., Oughaddou, H., Léandri, C., Ealet, B., Le Lay, G., *Appl. Phys. Lett.* 96, 183102 (2010)
- <sup>19</sup> Lalmi, B., Oughaddou, H., Enriquez, H., Kara, A., Vizzini, S., Ealet, B., Aufray, B., *Appl. Phys. Lett.* 97, 223109 (2010)
- <sup>20</sup> Takeda, K., Shiraiishi, K., *Phys. Rev. B* 50, 14916 (1994)
- <sup>21</sup> Liu, H., Neal, A.T., Zhu, Z., Tomanek, D., Ye, P. D., arXiv:1401.4133 [cond-mat.mes-hall] (2014)
- <sup>22</sup> Watanabe, K., Taniguchi, T., Kanda, H., *Nature Mater.* 3, 404 (2004)
- <sup>23</sup> R. F. Frindt and A. D. Yoffe, *Proc. R. Soc. Lond. A*, 273, 69 (1963)
- <sup>24</sup> J. A. Wilson and A. D. Yoffe, *Adv. in Phys.*, 18, 193 (1969)
- <sup>25</sup> Yoffe, A. D., *Annu. Rev. Mater. Sci.* 3, 147 (1993)
- <sup>26</sup> Yoffe, A. D., *Adv. Phys.* 42, 173 (1993)
- <sup>27</sup> Cao, T., Wang G., Han, W., Ye H., Zhu, C., Shi, J., Niu, Q., Tan P., Wang E., Liu, B. & Feng J, *Nature Comm.* 3, 887 (2012)
- <sup>28</sup> D. Xiao, G.-B. Liu, W. Feng, X. Xu, and W. Yao, *Phys. Rev. Lett.*, 108, 196802 (2012)
- <sup>29</sup> Zeng, H., Dai, J., Yao, W., Xiao, D. & Cui, X., *Nature Nanotech.* 7, 490 (2012)
- <sup>30</sup> Eda, G., Fujita, T., Yamaguchi, H., Voiry, D., Chen, M. W. & Chhowalla, M., *ACS Nano* 6, 7311 (2012)
- <sup>31</sup> Yin, Z., Li, H., Li, H., Jiang, L., Shi, Y., Sun, Y., Lu, G., Zhang, Q., Chen, X., and Zhang, H., *ACS Nano* 6, 74 (2012)

- <sup>32</sup> Ataca, C., and Ciraci, S., *J. Phys. Chem. C*, 2011, 115(27), 13303 (2011)
- <sup>33</sup> Raybaud, P., Hafner, J., Kresse, G., Kasztelan, S., Toulhoat, H., *J. Catal.* 189, 129 (2000)
- <sup>34</sup> Bromley, R.A., *Phys. Lett. A* 33, 242 (1970)
- <sup>35</sup> Castellanos-Gomez, A., Agrait, N., Rubio-Bollinger, G., *Appl. Phys. Lett.* 96(21), 213116 (2010)
- <sup>36</sup> Lee, W. Y., Besmann, T. M., and Stott, M. W., *Journal of Materials Research*, 9 (6), 1474 (1994)
- <sup>37</sup> T. F. Jaramillo, K. P. Jorgensen, J. Bonde, J. H. Nielsen, S. Horch, and I. Chorkendorff, *Science*, 317, 100 (2007)
- <sup>38</sup> Nicolosi, V., Chhowalla, M., Kanatzidis, M. G., Strano, M. S., Coleman, J. N., *Science* 340, 6139 (2013)
- <sup>39</sup> H. I. Karunadasa, E. Montalvo, Y. Sun, M. Majda, J. R. Long, and C. J. Chang, *Science*, 335, 698 (2012)
- <sup>40</sup> Schwierz, F., *Nature Nanotech.* 5, 487 (2010)
- <sup>41</sup> Jariwala D., Sangwan V. K., Lauhon L. J., Marks T. J. and Hersam M.C., *ACS Nano*, 8, 1102 (2014)
- <sup>42</sup> Koppens F. H., Mueller T., Avouris P., Ferrari A. C., Vitiello M. S. and Polini M., *Nat. Nanotec.*, 9, 780 (2014)
- <sup>43</sup> Fiori G., Bonaccorso F., Iannaccone G., Palacios T., Neumaier D., Seabaugh A., Banerjee S. K. and Colombo L., *Nat. Nanotech.*, 9, 768 (2014)
- <sup>44</sup> Neto, A.H.C., Guinea, F., Peres, N.M.R., Novoselov, K.S., Geim, A.K., *Rev. Mod. Phys.* 81, 109 (2009)
- <sup>45</sup> A. H. Castro Neto, F. Guinea, N. M. R. Peres, K. S. Novoselov, and A. K. Geim, *Rev. Mod. Phys.* 81, 109 (2009)
- <sup>46</sup> Y.-M. Lin, K. A. Jenkins, A. Valdes-Garcia, J. P. Small, D. B. Farmer, and P. Avouris, *Nano Letters*, 9, 422 (2009)
- <sup>47</sup> Y.-M. Lin, C. Dimitrakopoulos, K. A. Jenkins, D. B. Farmer, H.-Y. Chiu, A. Grill, and P. Avouris, *Science*, 327, 5966 (2010)
- <sup>48</sup> T. Palacios, A. Hsu, and Han Wang, *IEEE Comm. Mag.*, 48, 122 (2010)
- <sup>49</sup> H. Wang, A. Hsu, J. Wu, J. Kong, and T. Palacios, *IEEE Elec. Dev. Letters*, 31, 906 (2010)

- <sup>50</sup> I. Meric, N. Baklitskaya, P. Kim, and K. L. Shepard, Electron Devices Meeting, IEDM2008. IEEE International, 1 (2008)
- <sup>51</sup> Novoselov, K. S., Geim, A. K., Morozov, S. V., Jiang, D., Zhang, Y., Dubonos, S. V., Grigorieva, I. V., Firsov, A. A., Science 306, 666 (2004)
- <sup>52</sup> K. S. Novoselov, A. K. Geim, S. V. Morozov, D. Jiang, M. I. Katsnelson, I. V. Grigorieva, S. V. Dubonos and A. A. Firsov, Nature 438, 197 (2005)
- <sup>53</sup> Bae, S., Kim, H., Lee, Y., Xu, X., Park, J.-S., Zheng, Y., Balakrishnan, J., Lei, T., Kim, H. R., Song, Y. I., Kim, Y.-J., Kim, K. S., Özyilmaz, B., Ahn, J.-H., Hong, B. H., Iijima, S., Nat. Nanotechnol., 5, 574. (2010)
- <sup>54</sup> Reina, A., Jia, X., Ho, J., Nezich, D., Son, H., Bulovic, V., Dresselhaus, M. S., Kong, J., Nano. Lett., 9 (1), 30 (2009)
- <sup>55</sup> J.-H. Chen, C. Jang, S. Xiao, M. Ishigami, and M. S. Fuhrer, Nat Nano, 3, 206 (2008)
- <sup>56</sup> Lee, C., Wei, X. D., Kysar, J. W. & Hone, J., Science 321, 385 (2008)
- <sup>57</sup> Blake, P., Brimicombe, P. D., Nair, R.R., Booth, T. J., Jiang, D., Schedin, F., Ponomarenko, L. A., Morozov, S. V., Gleeson, H. F., Hill, E. W., Geim, A. K., Novoselov, K. S., Nano Lett., 8, 1704 (2008)
- <sup>58</sup> Bonaccorso, F., Sun, Z., Hasan, T., and Ferrari, A. C., Nat. Photon. 4, 611 (2010)
- <sup>59</sup> Baby, T. T., Aravind, S. S. J., Arockiadoss, T., Rakhi, R. B., Ramaprabhu, S., Sci. Direct. 145(1), 71 (2010)
- <sup>60</sup> Geim, A. K., Novoselov, K. S. Nat. Mater. 6, 183 (2007)
- <sup>61</sup> Özyilmaz, B., Jarillo-Herrero, P., Efetov, D., Abanin, D. A., Levitov, L. S., Kim, P. Phys. Re V . Lett. 99, 166804 (2007)
- <sup>62</sup> Morozov, S. V., Novoselov, K. S., Katsnelson, M. I., Schedin, F., Elias, D. C., Jaszczak, J. A., Geim, A. K. Phys. Rev . Lett. 100, 016602 (2008)
- <sup>63</sup> M. C. Lemme, T. J. Echtermeyer, M. Baus, and H. Kurz, 28, 282 (2007)
- <sup>64</sup> Kedzierski, J., Hsu, P.-L., Healey, P., Wyatt, P. W., Keast, C.L., Sprinkle, M., Berger, C., de Heer, W. A., IEEE Trans. Electron. Dev. 55, 2078 (2008)
- <sup>65</sup> Kedzierski, J., Hsu, P.-L., Reina, A., Kong, J., Healey, P., Wyatt, P. W., Keast, C., IEEE Electron Dev. Lett. 30, 745 (2009)
- <sup>66</sup> Li, X., Wang, X., Zhang, L., Lee, S. & Dai, H.: Science 319, 1229 (2008).
- <sup>67</sup> Enyashin, A., Gemming, S., Seifert, G., Eur. Phys. J. 149, 103 (2007)

- <sup>68</sup> Xu, M., Liang, T., Shi, M., Chen, H., Chem. Rev. , 113, 3766 (2013)
- <sup>69</sup> Ataca, C., Sahin, H., Ciraci, S., J. Phys. Chem. C 116, 8983 (2012)
- <sup>70</sup> Huang, X., Zeng, Z., Zhang, H., Chem. Soc. Rev. 42, 1934 (2013)
- <sup>71</sup> Song, X., Hu, J., Zeng, H., J. Mater. Chem. C 1, 2952 (2013)
- <sup>72</sup> G. Gao, W. Gao, E. Cannuccia, J. Taha-Tijerina, L. Balicas, A. Mathkar, T. N. Narayanan, Z. Liu, B. K. Gupta, J. Peng, Y. Yin, A. Rubio, and P. M. Ajayan, Nano Lett., 12.3518 (2012)
- <sup>73</sup> Lopez-Sanchez, O., Lembke, D., Kayci, M., Radenovic A., and Kis A., Nat. Nanotechnol., 8, 497 (2013)
- <sup>74</sup> V. Podzorov, M. E. Gershenson, C. Kloc, R. Zeis, and E. Bucher, Applied Physics Letters, 84, 3301 (2004)
- <sup>75</sup> Kuc, A., Zibouche, N. & Heine, T., Phys. Rev. B 83, 245213 (2011)
- <sup>76</sup> Mann, J., Ma, Q., Odenthal, P. M., Isarraraz, M., Le, D., Preciado, E., Barroso, D., Yamaguchi, K., von Son Palacio, G., Nguyen, A., Tran, T., Wurch, M., Nguyen, A., Klee, V., Bobek, S., Sun, D., Heinz, Tony. F., Rahman, T. S., Kawakami, R., and Bartels, L., Adv. Mater., 26, 1399 (2014)
- <sup>77</sup> Ataca, C., and Ciraci, S., J. Phys. Chem. C: 115, 13303 (2011)
- <sup>78</sup> Schwierz, F., Nat. Nanotechnol. 6 135 (2011)
- <sup>79</sup> Zeng, H., Dai, J., Yao, W., Xiao, D., and Cui, X. Nat. Nanotechnol., 7, 490 (2012)
- <sup>80</sup> Zhang, W., Chuu, C. P., Huang, J. K., Chen C. H., Tsai, M.L, Chang Y. H., Liang C.T., Chen Y.Z., Chueh Y.L., He J. H., Chou, M. Y. and Li L. J., Sci. Rep.,4, 3826 (2014)
- <sup>81</sup> Schweiger, H., Raybaud, P., Kresse, G., Toulhoat, H., J. Catal. 207, 76 (2002)
- <sup>82</sup> Sun, M., Adjaye, J., Nelson, A.E., Appl. Catal. A 263, 131 (2004)
- <sup>83</sup> Fontana, M., Deppe, T., Boyd, A. K., Rinzan, M., Liu, A. Y., Paranjape, M., and Barbara, P., Sci. Reports 3, 1634 (2013)
- <sup>84</sup> Arco, L. G. D., Zhang, Y., Schlenker, C. W., Ryu, K., Thompson, M. E., Zhou, C., ACS Nano 4, 2865 (2010)
- <sup>85</sup> Zhou, W., Yin, Z., Du, Y., Huang, X., Zeng, Z., Fan, Z., Liu, H., Wang, J., and Zhang, H., Small: 9, 140 (2013)
- <sup>86</sup> Yang, L. C., Wang, S. N., Mao, J. J., Deng, J. W., Gao, Q. S., Tang, Y., and Schmidt, O. G., Adv. Mater. 25, 1180 (2013)

- <sup>87</sup> Cho, M. H., Ju, j., Kim, S. J., and Jang, h., 260, 855 (2006)
- <sup>88</sup> Kam, K. K. and Parkinson, B. A. J. Phys. Chem. 86, 463 (1982)
- <sup>89</sup> Ho, W. K., Yu, J. C., Lin, J., Yu, J. G. and Li, P. S. Langmuir 20, 5865 (2004)
- <sup>90</sup> Gourmelon, E., Lignier, O., Hadouda, H., Couturier, G., Bernede, J. C., Tedd, J., Pouzet, J. and Salardenne, J. Sol. Energy Mater. Sol. Cells 46, 115 (1997)
- <sup>91</sup> Mak, K. F., Shan, J. and Heinz, T. F. Phys. Rev. Lett. 104, 176404 (2010)
- <sup>92</sup> Splendiani, A., Sun, L., Zhang, Y., Li, T., Kim, J., Chim, C.-Y., Galli, G., Wang, F., Nano Lett. 10, 1271(2010)
- <sup>93</sup> Mak, K.F., Lee, C., Hone, J., Shan, J., Heinz, T.F., Phys. Rev. Lett. 105, 136805 (2010)
- <sup>94</sup> Harper P. G., Edmondson, D. R., Phys. Stat. Sol. (b) 44, 59 (1971)
- <sup>95</sup> Radisavljevic, B., Radenovic, A., Brivio, J., Giacometti, V., and Kis, A., Nat. Nanotechnol. 6, 147 (2011)
- <sup>96</sup> Cheng, R.; Jiang, S.; Chen, Y.; Liu, Y.; Weiss, N.; Cheng, H.-C.; Wu, H.; Huang, Y.; Duan, X., Nature Commun. 5, 5143 (2014)
- <sup>97</sup> Krasnozhan, D.; Lembke, D.; Nyffeler, C.; Leblebici, Y.; Kis, A. Nano Lett. 14, 5905 (2014)
- <sup>98</sup> L. Liu, S. B. Kumar, Y. Ouyang, and J. Guo, IEEE Trans. on Elec. Dev., 58, 3042 (2011)
- <sup>99</sup> Perkins, F. K., Friedman, A. L., Cobas, E., Campbell, P. M., Jernigan G. G. and Jonker, B. T., Nano Lett., 13, 668 (2013)
- <sup>100</sup> H. Li, Z. Yin, Q. He, H. Li, X. Huang, G. Lu, D. W. H. Fam, A. I. Y. Tok, Q. Zhang, and H. Zhang, Small, 8, 63 (2012)
- <sup>101</sup> Wang, H., Yu, L., Lee, Y.-H., Shi, Y., Hsu, A., Chin, M., Li, L.-J., Dubey, M., Kong, J., and Palacios, T., Nano Lett. 12, 4674 (2012)
- <sup>102</sup> Radisavljevic, B., Whitwick, M. B., and Kis, A., ACS Nano 5, 9934 (2011)
- <sup>103</sup> Singh, N., Jabbour, G., and Schwingenschlögl, U., Eur. Phys. J. B, 85, 392(2012)
- <sup>104</sup> Z. Yin, H. Li, H. Li, L. Jiang, Y. Shi, Y. Sun, G. Lu, Q. Zhang, X. Chen and H. Zhang, ACS Nano, 6, 74 (2011).
- <sup>105</sup> W. Zhang, J.-K. Huang, C.-H. Chen, Y.-H. Chang, Y.-J. Cheng and L.-J. Li, Adv. Mater., 25, 3456 (2013)
- <sup>106</sup> Mak, K.F., He, K., Shan, J., Heinz, T. F., Nat. Nanotechnol. 7, 494 (2012)

- <sup>107</sup> Gordon, R. A., Yang, D., Crozier, E. D., Jiang, D. T. & Frindt, R. F., *Phys. Rev. B* 65, 125407 (2002)
- <sup>108</sup> Sandoval, S. J., D. Yang, D., R. F. Frindt R. F., and J. C. Irwin, J. C., *Phys. Rev. B* 44, 3955 (1991)
- <sup>109</sup> SPI Supplies Brand Moly Disulfide (MoS<sub>2</sub>),  
“<http://www.2spi.com/catalog/molybdenum.shtml>”
- <sup>110</sup> Li, H., Lu, G., Yin, Z.-Y., He, Q.-Y., Li, H., Zhang, Q., Zhang, H., *Small* 8, 682 (2012)
- <sup>111</sup> Castellanos-Gomez, A., Barkelid, M., Goossens, A. M., Calado, V. E., van der Zant, H. S. J., and Steele, G. A., *Nano Lett.* 12, 3178 (2012)
- <sup>112</sup> Lu, X., Utama, M. I. B., Zhang, J., Zhao, Y., Xiong, Q., *Nanoscale* 5, 8904 (2013)
- <sup>113</sup> Late, D. J., Huang, Y. K., Liu, B., Acharya, J., Shirodkar, S. N., Luo, J., Yan, A., Charles, D., Waghmare, U. V., Dravid, V. P., Rao, C. N.: *ACS Nano*, 7, 4879 (2013)
- <sup>114</sup> Castellanos-Gomez, A., Agrait, N., Rubio-Bollinger, G., *Appl. Phys. Lett.* 96, 213116 (2010)
- <sup>115</sup> Benameur, M., Radisavljevic, B., Héron, J. S., Sahoo, S., Berger, H., and Kis, A., *Nanotechnology* 22, 125706 (2011)
- <sup>116</sup> Li, H., Wu, J., Huang, X., Lu, G., Yang, J., Lu, X., Xiong, Q., Zhang, H.: *ACS Nano*. 7, 10344 (2013)
- <sup>117</sup> Smith, R. J., King, P. J., Lotya, M., Wirtz, C., Khan, U., De, S., O’Neill, A., Duesberg, G. S., Grunlan, J. C., Moriarty, G., Chen, J., Wang, J. Z., Minett, A. I., Nicolosi, V., Coleman, J. N. *Adv. Mater.* 23, 3944 (2011)
- <sup>118</sup> Coleman, J. N., Lotya, M., O’Neill, A., Bergin, S. D., King, P. J., Khan, U., Young, K., Gaucher, A., De, S., Smith, R. J., Shvets, I. V., Arora, S. K., Stanton, G., Kim, H. Y., Lee, K., Kim, G. T., Duesberg, G. S., Hallam, T., Boland, J. J., Wang, J. J., Donegan, J. F., Grunlan, J. C., Moriarty, G., Shmeliov, A., Nicholls, R. J., Perkins, J. M., Grievson, E. M., Theuwissen, K., McComb, D. W., Nellist, P. D., Nicolosi, V. *Science* 331, 568 (2011)
- <sup>119</sup> Zhou, K. G., Mao, N. N., Wang, H. X., Peng, Y., Zhang, H. L. *Angew. Chem., Int. Ed.* 50, 10839 (2011)
- <sup>120</sup> Cunningham, G., Lotya, M., Cucinotta, C. S., Sanvito, S., Bergin, S. D., Menzel, R., Shaffer, M. S. P., Coleman, J. N. *ACS Nano* 6, 3468 (2012)
- <sup>121</sup> Dines, M. B.: *Materials Research Bulletin*, 10, 287 (1975)

- <sup>122</sup> B.G. Silbernagel, B. G.: Solid State Communication, 17, 361 (1975)
- <sup>123</sup> M.Stanley Whittingham, M. S., Fred R. Gamble F. R.: Materials Research Bulletin, 10, 363 (1975)
- <sup>124</sup> Py, M. A., Haering, R. R.: Canadian Journal of Physics. 61, 76 (1983)
- <sup>125</sup> Mulhern, P. J.: Canadian Journal of Physics. 67, 1049 (1989)
- <sup>126</sup> Joensen, P.; Frindt, R. F.; Morrison, S. R.: Mater. Res. Bull., 21, 457 (1986)
- <sup>127</sup> X. Li, W. Cai, J. An, S. Kim, J. Nah, D. Yang, R. Piner, A. Velamakanni, I. Jung, E. Tutuc, S. K. Banerjee, L. Colombo, R., and S. Ruoff, Science 324, 1312 (2009)
- <sup>128</sup> Su, C.-Y., Lu, A.-Y., Wu, C.-Y., Li, Y.-T., Liu, K.-K., Zhang, W., Lin, S.-Y., Juang, Z.-Y., Zhong, Y.-L., Chen, F.-R., and Li, L.-J., Nano Lett. 11, 3612 (2011)
- <sup>129</sup> Sun, Z., Yan, Z., Yao, J., Beitler, E., Zhu, Y., and Tour, J. M., Nature 468, 549 (2010)
- <sup>130</sup> K. S. Kim, Y. Zhao, H. Jang, S. Y. Lee, J. M. Kim, K. S. Kim, J.-H. Ahn, P. Kim, J.-Y. Choi, and B. H. Hong, Nature, 457, 7230 (2009)
- <sup>131</sup> S. Bae, H. Kim, Y. Lee, X. Xu, J.-S. Park, Y. Zheng, J. Balakrishnan, T. Lei, H. Ri Kim, Y. I. Song, Y.-J. Kim, K. S. Kim, B. Ozyilmaz, J.-H. Ahn, B. H. Hong, and S. Iijima, Nat Nano, 5, 574 (2010)
- <sup>132</sup> Kim, H., Ahn, C., Arabale, G., Lee, C., and Kim, T., ECS Trans. 58, 470 (2013)
- <sup>133</sup> Jeon, J., Jang, S. K., Jeon, S. M., Yoo, G., Jang, Y. H., Park, J.-H. and Lee, S., Nanoscale, DOI: 10.1039/C4NR04532G (2015)
- <sup>134</sup> Shi, Y., Li, H. and Li, L.-H., Chem. Soc. Rev., DOI: 10.1039/C4CS00256C (2014)
- <sup>135</sup> Liu, K.-K., Zhang, W., Lee, Y.-H., Lin, Y.-C., Chang, M.-T., Su, C.-Y., Chang, C.-S., Li, H., Shi, Y., Zhang, H., Lai, C.-S., and Li, L.-J., Nano Lett., 12, 1538 (2102)
- <sup>136</sup> Zhan, Y., Liu, Z., Najmaei, S., Ajayan, P. M., and Lou, J., Small 8, 966 (2012)
- <sup>137</sup> Lee, Y.-H., Zhang, X.-Q., Zhang, W., Chang, M.-T., Lin, C.-T., Chang, K.-D., Yu, Y.-C., Wang, J. T.-W., Chang, C.-S., Li, L.-J., and Lin, T.-W., arXiv 1202, 5458 (2012)
- <sup>138</sup> Lee, Y.-H., Zhang, X.-Q., Zhang, W., Chang, M.-T., Lin, C.-T., Chang, K.-D., Yu, Y.-C., Wang, J. T.-W., Chang, C.-S., Li, L.-J., and Lin, T.-W., Adv. Mater. 24, 2320 (2012)
- <sup>139</sup> Najmaei, S., Liu, Z., Zhou, W., Zou, X., Shi, G., Lei, S., Yakobson, B. I., Idrobo, J.-C., Ajayan, P. M., and Lou, J., Nat. Mater. 12, 754 (2013)

- <sup>141</sup> Van der Zande, A. M., Huang, P. Y., Chenet, D. A., Berkelbach, T. C., You, Y. M., Lee, G.-H., Heinz, T. F., Reichman, D. R., Muller, D. A., and Hone, J. C., *Nat. Mater.* 12, 554 (2013)
- <sup>142</sup> Lee, C., Yan, H., Brus, L. E., Heinz, T. F., Hone, J., Ryu, S. *ACS Nano* 4, 2695 (2010)
- <sup>143</sup> Zhou, K., Zhu, Y., Yang, X., Zhou, J., Li, C.: *Chem. Phys. Chem.* 13, 699 (2012)
- <sup>144</sup> International Technology Roadmap for Semiconductor,  
“<http://www.itrs.net/Links/2011ITRS/Home2011.htm>”
- <sup>145</sup> Gordon E. Moore, “Cramming More Components onto Integrated Circuits”, *Proceedings of the IEEE*, 86, 1 (1998)
- <sup>146</sup> A. Khakifirooz and D. A. Antoniadis, *Electron Devices Meeting, 2006. IEDM '06. International*, 1 (2006)
- <sup>147</sup> D. A. Antoniadis, I. Aberg, C. Ni Chleirigh, O. M. Nayfeh, A. Khakifirooz, and J. L. Hoyt, *IBM Journal of Research and Development*, 50, 363 (2006)
- <sup>148</sup> Lin, Y.-M., Farmer, D. B., Jenkins, K. A., Tedesco, J. L., Myers-Ward, R. L., Eddy Jr., C. R., Gaskill, D. K., Wu, Y., Dimitrakopoulos, C., and Avouris, P., *Electron Device Letters*, *IEEE* 32, 13435 (2011)
- <sup>149</sup> Frank, D. J., Wong, H.-S. P., *IEEE Electron Device letters*, 19, 10, (1998)
- <sup>150</sup> Chen, J-H., Jang, C., Xiao, S., Ishigami, M. & Fuhrer, M. S., *Nature Nanotech.* 3, 206 (2008)
- <sup>151</sup> Geim, A., *Bull. Am. Phys. Soc.* 55, abstr. J21.0004,  
<http://meetings.aps.org/link/BAPS.2010.MAR.J21.4> (2010)
- <sup>152</sup> Ayari, A., Cobas, E., Ogundadegbe, O. & Fuhrer, M. S., *J. Appl. Phys.* 101, 014507 (2007)
- <sup>153</sup> Yoon, Y., Ganapathi, K., and Salahuddin, S., *Nanoletters*, 11, 3768 (2011)
- <sup>154</sup> Liu, H., Neal, A. T., and Ye, P. D., *ACS Nano*, 6, 8563 (2012)
- <sup>155</sup> Das, S., Chen, H.-Y., Penumatcha, A. V., and Appenzeller, J., *Nano Lett.*, 13 (1), 100 (2013)
- <sup>156</sup> Das, S., and Appenzeller, J., *Nano Lett.*, 13, 3396 (2013)
- <sup>157</sup> Fang, H., Tosun, M., Seol, G., Chang, T. C., Takei, K., Guo, J., and Javey, A., *Nano Lett.*, 13, 1991 (2013)

- <sup>158</sup> Kim, S., Konar, A., Hwang, W.-S., Lee, J. H., Lee, J., Yang, J., Jung, C., Kim, H., Yoo, J.-B., Cho, J.-Y., Jin, Y. W., Lee, S. Y., Jena, D., Choi, W., & Kim, K., *Nat. Commun.* 3, 1011 (2012)
- <sup>159</sup> C. D. English, G. Shine, V. E. Dorgan, K. C. Saraswat and E. Pop, 72<sup>nd</sup> DRC, 193 (2014)
- <sup>160</sup> A. T. Neal, H. Liu, J. J. Gu and P. D. Ye, 72<sup>nd</sup> DRC, 65 (2014)
- <sup>161</sup> H. Qiu, L. Pan, Z. Yao, J. Li and Y. Shi, *Appl. Phys. Lett.* 100, 123104 (2012)
- <sup>162</sup> N. Kaushik, A. Niapne, F. Basheer, S. Dubey, S. Grover, M. M. Deshmukh and S. Lodha, *Appl. Phys. Lett.* 105, 113505 (2014)
- <sup>163</sup> Popov I., Seifert G., Tománek D., *Phys Rev Lett.* 108, 156802 (2012)
- <sup>164</sup> Baugher, B. W., Churchill, H. O., Yang, Y., Jarillo-Herrero, P., *Nano Lett.* 13, 4212 (2013)
- <sup>165</sup> Schmidt, H., Wang, S., Chu, L., Toh, M., Kumar, R., Zhao, W., Neto, A. H. C., Martin, J., Adam, S., Özyilmaz, B., and Eda, G., *Nano Lett.* 14, 1909 (2014)
- <sup>166</sup> Kim, S. Y., Park, S. and Choi, W., *Appl. Phys. A*, 117, 761 (2014)
- <sup>167</sup> Dankert, A., Langouche, L., Kamalakar, M. V., and Dash S. P., *ACS Nano.* 8, 476 (2014)
- <sup>168</sup> Chen, J. R., Odenthal, P. M., Swartz, A. G., Floyd, G. C., Wen, H., Luo, K. Y., and Kawakami, R. K., *Nano Lett.* 13, 3106 (2013)
- <sup>169</sup> Leong, W. S., Luo, X., Li, Y., Khoo, K. H., Quek, S. Y. and Thong, J. T. L., arXiv:1410.1328 [cond-mat.mes-hall] (2014)
- <sup>170</sup> Wang, L.; Xu, Z.; Wang, W.; Bai, X., *J. Am. Chem. Soc.*, 136, 6693 (2014)
- <sup>171</sup> Lin, Y.-C.; Dumcenco, D. O.; Huang, Y.-S.; Suenaga, K., *Nat. Nanotechnol.*, 9, 391 (2014)
- <sup>172</sup> Cheng Y., Nie A., Zhang Q., Gan L. Y., Shahbazian-Yassar R., Schwingenschlogl U., *ACS Nano*, DOI: 10.1021/nn505668c (2014)
- <sup>173</sup> J. Chastain, P.-E. C. P. E. Division, and J. F. Moulder, *Handbook of x-ray photoelectron spectroscopy a reference book of standard spectra for identification and interpretation of XPS data*. Eden Prairie, Minn: Perkin-Elmer Corporation, Physical Electronics Division, 1992

- <sup>174</sup> Jariwala, D., Sangwan, V. K., Late, D. J., Johns, J. E., Dravid, V. P., Marks, T. J., Lauhon, L. J. and Hersam, M. C., *Appl. Phys. Lett.* 102, 173107 (2013)
- <sup>175</sup> S. Ghatak, A. N. Pal, and A. Ghosh, *ACS Nano* 5, 7707 (2011)
- <sup>176</sup> H. Liu, A. T. Neal, and P. D. Ye, *ACS Nano* 6, 8563 (2012)
- <sup>177</sup> R. Koppera, D. Voiry, S. E. Yalcin, B. Branch, G. Gupta, A. D. Mohite and M. Chhowalla, *Nat. Mater.* doi:10.1038/nmat4080 (2014)
- <sup>178</sup> S. M. Sze and K. K. Ng, *Physics of semiconductor devices*. Wiley-interscience, 2006.
- <sup>179</sup> McDonnell S., Brennan B., Azcatl A., Lu N., Dong H., Buie C., Kim J., Hinkle C. L., Kim M. J., Wallace R. M., *ACS Nano*, 7, 10354 (2013)
- <sup>180</sup> Valsaraj, A., Chang, J., Register, L. F. and Banerjee, S. K., *72nd DRC*, 87 (2014)
- <sup>181</sup> Kang. J., Liu, W. and Banerjee, K., *Appl. Phys. Lett.* 104, 093106 (2014)
- <sup>182</sup> J. Kang, D. Sarkar, W. Liu, D. Jena and K. Banerjee, *2012 IEEE International*, 17.4. 1 (2012)
- <sup>183</sup> Das, S. and Appenzeller, J., *Phys. Status Solidi RRL*, 7, 268 (2013)
- <sup>184</sup> R. Koppera, D. Voiry, S. E. Yalcin, W. Jen, M. Acerce, S. Torrel, B. Branch, S. Lei, W. Chen, S. Najmaei, J. Lou, P. M. Ajayan, G. Gupta, A. D. Mohite and M. Chhowalla, *APL Mat.* 2, 092516 (2014)
- <sup>185</sup> H. R. Gutierrez, N. Perea-Lopez, A. L. Elias, A. Berkdemir, B. Wang, R. Lv, F. Lopez-Urias, V. H. Crespi, H. Terrones, and M. Terrones, *Nano Lett.*, 13, 3447 (2013)
- <sup>186</sup> Chang Y. H., Zhang W., Zhu Y., Han Y., Pu J., Chang J. K., Hsu W. T., Huang J. K., Hsu C. L., Chiu M. H., Takenobu T., Li H., Wu C. I., Chang W. H., Wee A. T., Li L. J., *ACS Nano*, 8, 8582 (2014)
- <sup>187</sup> Wang X., Gong Y., Shi G., Chow W. L., Keyshar K., Ye G., Vajtai R., Lou J., Liu Z., Ringe E., Tay B. K., Ajayan P. M., *ACS Nano*, 8, 5125 (2014)
- <sup>188</sup> Huang J. K., Pu J., Hsu C. L., Chiu M. H., Juang Z. Y., Chang Y. H., Chang W. H., Iwasa Y., Takenobu T. and Li L.J., *ACS Nano*, 8, 923 (2014)
- <sup>189</sup> Xu K., Wang Z., Du X., Safdar M., Jiang C. and He J., *Nanotechnology*, 24, 465705 (2013)
- <sup>190</sup> McDonnell, S., Addou, R., Buie, C., Wallace, R. M. and Hinkle C. L., *ACS Nano*, 8, 2880 (2014)
- <sup>191</sup> S. D. Sarma, J. Fabian, X. Hu and I. Zutic, *Sol. St. Comm.*, 119, 207 (2001)

- <sup>192</sup> M. Johnson, *IEEE Spectrum*, 31, 47 (1994)
- <sup>193</sup> Wolf, S. A., and D. Treger. 2000. *IEEE Trans. on Magnetics*, 36, 2748 (2000)
- <sup>194</sup> Zutic, I., Fabian, J. and Sarma, S. D., *Rev. Mod. Phys.* 76, 323 (2004)
- <sup>195</sup> S. A. Wolf, D. D. Awschalom, R. A. Buhrman, J. M. Daughton, M. L. Roukes, A. Y. Chtchelkanova, D. M. Treger, *Science*, 294, 1488 (2001)
- <sup>196</sup> Xiao, D., Liu G. B., Feng W., Xu X. and Yao W., *Phys Rev Lett.* 108, 196802 (2012)
- <sup>197</sup> Zhu, Z. Y.; Cheng, Y. C.; Schwingenschlögl, U. *Phys. Rev. B* 84, 153402 (2011)
- <sup>198</sup> Lu, C-P., Li, G., Mao, J., Wang, L-M. and Andrei, E. Y., *Nanolett.* 14, 4628 (2014)
- <sup>199</sup> Geim, A. K., Grigorieva, *Nature*, 499, 419 (2013)
- <sup>200</sup> H. Fang, C. Battaglia, C. Carraro, S. Nemsak, B. Ozdol, J. S. Kang, H. A. Bechtel, S. B. Desai, F. Kronast, A. A. Unal, G. Conti, C. Conlon, G. K. Palsson, M. C. Martin, A. M. Minor, C. S. Fadley, E. Yablonovitch, R. Maboudian and Ali Javey, *Proc. Nat. Acad. Sci.* 111, 6198 (2014)
- <sup>201</sup> Shim G. W., Yoo K., Seo S. B., Shin J., Jung D. Y., Kang I. S., Ahn C. W., Cho B. J. and Choi S. Y., *ACS Nano* 22, 6655 (2014)
- <sup>202</sup> C.-H. Lee, G.-H. Lee, A. M. van der Zande, W. Chen, Y. Li, M. Han, X. Cui, G. Arefe, C. Nuckolls, T. F. Heinz, J. Guo, J. Hone and P. Kim, *Nat. Nanotech.*, 9, 676 (2014)
- <sup>203</sup> G.-H. Lee, C.-H. Lee, A. M. van der Zande, M. Han, X. Cui, G. Arefe, C. Nuckolls, T. F. Heinz, J. Hone and P. Kim, *APL Mat.*, 2, 092511 (2014)
- <sup>204</sup> Tsai M. L., Su S. H., Chang J. K., Tsai D. S., Chen C. H., Wu C. I., Li L. J., Chen L. J. and He J. H., *ACS Nano*, 8, 8317 (2014)
- <sup>205</sup> W. Liu, X. Yang, Y. Zhang, M. Xu and H. Chen, *RSC Advances* 4, 32744 (2014)
- <sup>206</sup> Britnell L., Ribeiro R. M., Eckmann A., Jalil R., Belle B. D., Mishchenko A., Kim Y. J., Gorbachev R. V., Georgiou T., Morozov S. V., Grigorenko A. N., Geim A. K., Casiraghi C., Castro Neto A. H., Novoselov K. S., *Science*, 340, 1311 (2014)
- <sup>207</sup> A. Pospischil, M. M. Furchi and T. Mueller, *Nat. Nanotech.* 9, 257 (2014)
- <sup>208</sup> Hong X., Kim J., Shi S. F., Zhang Y., Jin C., Sun Y., Tongay S., Wu J., Zhang Y. and Wang F., *Nat. Nanotech.*, 9, 682 (2014)
- <sup>209</sup> J. Xue, J. Sanchez-Yamagishi, D. Bulmash, P. Jacquod, A. Deshpande, K. Watanabe, T. Taniguchi, P. Jarillo-Herrero, and B. J. LeRoy, *Nat Mater*, 10, 282 (2011)

<sup>210</sup>H. Wang, T. Taychatanapat, A. Hsu, K. Watanabe, T. Taniguchi, P. Jarillo-Herrero, and T. Palacios, *IEEE Electron Device Letters*, 32, 1209 (2011)

## ACKNOWLEDGEMENT OF PREVIOUS PUBLICATIONS

This thesis dissertation is comprised of results from articles which are previously published and some which are presently under preparation. Results from Chapter 4, 5, 6 and 7 are published in *Kappera et al, Nature Materials*, doi:10.1038/nmat4080, (2014) and results from Chapter 4 and 8 are published in *Kappera et al, APL Materials*, 02, 092516 (2014). Results in Chapter 7 and 8 are under preparation for publication.